

# VORTEX FORMATION AND DYNAMICS IN SUPERFLUID $^3\text{He}$ AND ANALOGIES IN QUANTUM FIELD THEORY

V.B. Eltsov

*Low Temperature Laboratory, Helsinki University of Technology, Box 2200, FIN-02015 HUT, Finland  
and P.L. Kapitza Institute for Physical Problems, 119334 Moscow, Russia*

M. Krusius

*Low Temperature Laboratory, Helsinki University of Technology, Box 2200, FIN-02015 HUT, Finland*

G.E. Volovik

*Low Temperature Laboratory, Helsinki University of Technology, Box 2200, FIN-02015 HUT, Finland  
and L.D. Landau Institute for Theoretical Physics, 119334 Moscow, Russia*

The formation and dynamics of topological defects of different structure has been of central interest in the study of the  $^3\text{He}$  superfluids. Compared to superfluid  $^4\text{He-II}$ , the variability of the important parameters with temperature and pressure is wider and many features are more ideal. This has made experimentally new approaches possible. An example is the formation of quantized vortices and other topological defects in a rapid time-dependent phase transition from the normal state to  $^3\text{He-B}$ . This vortex formation process is known as the Kibble-Zurek mechanism and is one the central topics of this review. It demonstrates the use  $^3\text{He-B}$  as a model system for quantum fields, with detailed control from the laboratory.

*PACS:* 67.57.Fg, 47.32, 05.70.Fh, 98.80.Cq.

*Keywords:* superfluid, quantized vortex, cosmic string, vortex formation, vortex dynamics, mutual friction, non-equilibrium phase transition, superfluid turbulence, critical velocity.

# CONTENTS

|   |    |   |    |
|---|----|---|----|
| 1. Superfluid $^3\text{He}$ and quantum field theory                          | 3  | 3.2.2. Gravitational Aharonov-Bohm effect   | 49 |
| 2. Defect formation in quench-cooled superfluid transition                    | 3  | 3.2.3. Asymmetric cross section of scattering from a vortex   | 50 |
| 2.1. Non-equilibrium phase transitions  | 3  | 3.2.4. Iordanskii force: quantized vortex and spinning string   | 50 |
| 2.2. Cosmic large-scale structure   | 4  | 3.3. Spectral flow force and chiral anomaly   | 51 |
| 2.3. Kibble-Zurek mechanism   | 4  | 3.3.1. Chiral anomaly   | 51 |
| 2.4. Experimental verification of KZ mechanism                                | 5  | 3.3.2. Anomalous force acting on a continuous vortex and baryogenesis from textures                     | 53 |
| 2.5. Principle of superfluid $^3\text{He}$ experiments                        | 7  | 3.3.3. Anomalous force acting on a singular vortex and baryogenesis with strings                        | 54 |
| 2.5.1. Outline of experimental method   | 7  | 3.4. Analog of magnetogenesis: vortex textures generated in normal-superfluid counterflow               | 56 |
| 2.5.2. Interpretation of $^3\text{He}$ experiments                            | 8  | 3.5. Vortex mass: chiral fermions in strong magnetic field  | 58 |
| 2.6. Measurement of vortex lines in $^3\text{He-B}$                           | 9  | 3.5.1. “Relativistic” mass of the vortex  | 58 |
| 2.6.1. Critical velocity of vortex formation                                  | 9  | 3.5.2. Contribution from bound states to the mass of a singular vortex                                  | 59 |
| 2.6.2. Rotating states of the superfluid                                      | 10 | 3.5.3. Kopnin vortex mass in the continuous-core model: connection to chiral fermions in magnetic field | 59 |
| 2.6.3. Experimental setup   | 10 | 3.5.4. Associated hydrodynamic mass   | 60 |
| 2.6.4. NMR measurement  | 11 | 3.5.5. Topology of the energy spectrum: gap nodes and their ramifications                               | 61 |
| 2.7. Vortex formation in neutron irradiation                                  | 12 | 4. Final remarks  | 62 |
| 2.8. Volume or surface mechanism?   | 15 | Acknowledgements  | 62 |
| 2.9. Threshold velocity for vortex loop escape                                | 17 | References  | 63 |
| 2.9.1. Properties of threshold velocity                                       | 17 |   |    |
| 2.9.2. Influence of $^3\text{He-A}$ on the threshold velocity $v_{\text{cn}}$ | 17 |   |    |
| 2.10. Other defect structures formed in neutron irradiation                   | 19 |   |    |
| 2.10.1. Radiation-induced supercooled $A \rightarrow B$ transition            | 19 |   |    |
| 2.10.2. Vortex formation, AB interfaces, and KZ mechanism                     | 20 |   |    |
| 2.10.3. Spin-mass vortex  | 20 |   |    |
| 2.11. Vortex formation in gamma radiation                                     | 23 |   |    |
| 2.12. Bias dependence of loop extraction                                      | 24 |   |    |
| 2.12.1. Experimental velocity dependence                                      | 24 |   |    |
| 2.12.2. Analytic model of vortex loop escape                                  | 25 |   |    |
| 2.13. Neutron-induced vortex formation at low temperatures                    | 27 |   |    |
| 2.13.1. Experimental techniques   | 28 |   |    |
| 2.13.2. Measurement of vortex formation rate                                  | 29 |   |    |
| 2.13.3. Superfluid turbulence in neutron irradiation                          | 30 |   |    |
| 2.13.4. Calorimetry of vortex network   | 32 |   |    |
| 2.14. Simulation of loop extraction   | 34 |   |    |
| 2.14.1. Initial loop distribution   | 35 |   |    |
| 2.14.2. Network evolution under scaling assumptions                           | 36 |   |    |
| 2.14.3. Direct simulation of network evolution                                | 38 |   |    |
| 2.15. Superfluid transition as a moving phase front                           | 40 |   |    |
| 2.15.1. Neutron absorption and heating  | 40 |   |    |
| 2.15.2. Thermal gradient and velocity of phase front                          | 41 |   |    |
| 2.16. Quench of infinite vortex tangle  | 43 |   |    |
| 2.16.1. Vorticity on microscopic and macroscopic scales                       | 43 |   |    |
| 2.16.2. Scaling in equilibrium phase transitions                              | 44 |   |    |
| 2.16.3. Non-equilibrium phase transitions                                     | 45 |   |    |
| 2.17. Implications of the quench-cooled experiments                           | 45 |   |    |
| 2.17.1. Topological-defect formation  | 45 |   |    |
| 2.17.2. Phase transitions   | 46 |   |    |
| 3. Vortex dynamics and quantum field theory analogues                         | 47 |   |    |
| 3.1. Three topological forces acting on a vortex and their analogues          | 47 |   |    |
| 3.2. Iordanskii force   | 48 |   |    |
| 3.2.1. Superfluid vortex vs spinning cosmic string                            | 48 |   |    |

## 1. SUPERFLUID $^3\text{He}$ AND QUANTUM FIELD THEORY

In recent times condensed matter and elementary particle physics have been experiencing remarkable convergence in their developments, as many-body aspects have become increasingly more important in particle physics: The Early Universe is the ultimate application field for the theories on interacting particle systems which can be worked out for different energy regimes, or epochs of the expansion after the Big Bang. Compact astrophysical objects provide other “laboratories” with a narrower range of conditions in which to test theories. Actual collider experiments are set up to study interacting particle systems, such as the quark-gluon plasma in heavy ion collisions or the pion condensate.

Collective phenomena in interacting many-body systems is what condensed matter physics is about, but elementary particle systems are adding to the picture extreme quantum behavior plus relativistic motion. So far systems, where all of these features would be of importance, are not available for direct observation. During the nineties it turned out that valuable analogues can nevertheless be constructed from comparisons with non-relativistic many-body quantum systems of condensed matter, such as superconductors and helium superfluids. More recently optically cooled alkali atom clouds have been added to this list. Here we limit our discussion to the fermionic  $^3\text{He}$  superfluids.

The liquid  $^3\text{He}$  phases provide attractive advantages as model systems for the study of various general concepts in quantum field theory: The liquid is composed of neutral particles in an inherently isotropic environment — no complications arise from electrical charges or a symmetry constrained by a crystalline lattice. This allows one to concentrate on the consequences from a most complex symmetry breaking, which gives rise to a multi-dimensional order parameter space, but is well described by a detailed microscopic theory. Experimentally superfluid  $^3\text{He}$  is devoid of extrinsic imperfections. In fact, with respect to impurities and dirt it is one of the purest of all condensed matter systems, excepting optically cooled atom clouds. The superfluid coherence length is large such that even surface roughness can be reduced sufficiently to transform the container walls to almost ideally behaving boundaries. There are topologically stable defects of different dimensionality and type, which often can be detected with NMR methods with single-defect sensitivity. The study of the different intrinsic mechanisms, by which these defects are formed, provide one of the important parallels to other systems. Phase transitions of both first and second order exist, which can be utilized in the investigation of defect formation. Another example is the use of the zero-temperature  $^3\text{He}$  systems to model the complicated physical vacuum of quantum field theory — the modern ether:

The bosonic and fermionic excitations in  $^3\text{He}$  (in the dilute limit) are in many respects similar to the excitations of the physical vacuum — the elementary particles. This approach has been quite successful in constructing a physical picture of the interactions of elementary particles with strings and domain walls, as described in a recent monograph by one of the present authors (Volovik 2003).

This review describes some examples from superfluid  $^3\text{He}$  research where strong connections exist to quantum field theory. In fact, some of these studies were only taken up because they can be used as laboratory models, to answer the question whether a proposed principle is physically correct or not. Our discussion has been split in two parts: The first part Chap. 2 deals with a detailed description of defect formation and evolution in a rapid non-equilibrium phase transition of second order, caused by the localized heating from an absorption event in ionizing radiation. This phenomenon originally became interesting because it can be thought to model phase transitions in the early Universe. Defect formation in these transitions has been suggested as the origin for the inhomogeneous mass distribution in the present Universe. The second part Chap. 3 discusses concepts from vortex dynamics which have been used in Chap. 2 to analyze vortex formation in rapid phase transitions. This discussion proceeds in more general terms and continues to highlight connections to quantum field theory.

## 2. DEFECT FORMATION IN QUENCH-COOLED SUPERFLUID TRANSITION

### 2.1. Non-equilibrium phase transitions

A rapid phase transition is generally associated with a large degree of inhomogeneity. After all, this is the process by which materials like steel or amorphous solids are prepared. This disorder we attribute to heterogeneous extrinsic influence which is usually present in any system which we study: impurities, grain boundaries, and other defects depending on the particular system. To avoid disorder and domain formation, we generally examine phase transitions in the adiabatic limit, as close to equilibrium as possible.

But suppose we would have an ideally homogeneous infinite system with no boundaries. It is rapidly cooling from a symmetric high temperature state to a low temperature phase of lower symmetry, which we call the broken-symmetry phase, for example by uniform expansion. What would happen in such a transition? Are defects also formed in this case? Such a measurement of a homogeneous transition as a function of the transition speed, is difficult. As we shall see, ultimately it also raises the question whether the source of the precipitated inhomogeneity has been reliably identified.

## 2.2. Cosmic large-scale structure

According to the standard theory of cosmology the Universe started off in the “Big Bang” in a homogeneous state. It then rapidly cooled through a sequence of phase transitions, in which the four fundamental forces of nature separated out. Today the Universe exists in a state with inhomogeneous large-scale structure. The clumped distribution of visible mass has become most evident from galaxy surveys — maps which show that galaxies form clusters and these in turn super clusters, such as the “Great Wall”, which are the largest structures discovered to date (Geller and Huchra 1989). The clustering takes the form of long chains or filaments, which are separated by large voids, regions empty of visible mass. Recent extended galaxy surveys indicate that the length scale of large-scale structure is of order 100 Mpc<sup>1</sup> (Peacock et al. 2001).

Another image of large-scale structure has been preserved in the cosmic microwave background radiation, from the time when the Universe had cooled to a few eV, when nuclei and electrons combined to form atoms and the Universe became transparent to photons. Since then the background radiation has cooled in the expanding Universe. It now matches to within 3 parts in 10<sup>5</sup> the spectrum of a black body at 2.728 K, as measured eg. with the spectrometers on board of the satellite Cosmic Background Explorer (COBE) in 1990. Later balloon-borne measurements examined the spatial distribution of the residual anisotropy with high angular resolution and amplitude sensitivity. The recent satellite Wilkinson Microwave Anisotropy Probe (WMAP) has extended this work, mapping all-sky surveys with an angular resolution better than 1° on different frequency bands, to separate out the interfering signal from our galaxy (Bennett et al. 2003; Spergel et al. 2003). Combined with other information, this anisotropy of the cosmic microwave background radiation, 30 μK in amplitude, which represents the density fluctuations in the structure of the Universe when it was only 300 000 years old, is expected to explain the mechanisms which originally seeded and led to the formation of the large-scale structure, as we observe it today.

## 2.3. Kibble-Zurek mechanism

One of the early explanations for the origin of large-scale structure was offered by Tom Kibble (1976). He suggested that the inhomogeneity was created in rapid phase transitions of the early expanding Universe. Even

in a perfectly homogeneous transition of second order defects can be expected to form, if the transition proceeds faster than the order parameter of the broken-symmetry phase is able to relax. In such a non-equilibrium transition the new low-temperature phase starts to form, due to fluctuations of the order parameter, simultaneously and independently in many parts of the system. Subsequently during further cooling, these regions grow together to form the new broken-symmetry phase. At the boundaries, where different causally disconnected regions meet, the order parameter does not necessarily match and a domain structure is formed.

If the broken symmetry is the U(1) gauge symmetry, then domains with different value of the order parameter phase are formed. Such a random domain structure reduces to a network of linear defects, which are vortex lines in superfluids and superconductors or perhaps cosmic strings in the Early Universe. If the symmetry break is more complicated, as is the case in <sup>3</sup>He superfluids, then defects of different dimensionality and structure may be formed.

Subsequent numerical simulations of rapidly cooled second order phase transitions confirmed that defects were indeed forming (Vachaspati and Vilenkin 1984). In 1985 Wojciech Zurek proposed a conceptually powerful phenomenological approach how to understand a phase transition far out of equilibrium, when the outcome from the transition becomes time dependent (Zurek 1985, 1996). He characterizes the transition speed with a quench time

$$\tau_Q = \left( \frac{1}{T_c} \left| \frac{dT}{dt} \right|_{T=T_c} \right)^{-1}, \quad (1)$$

which allows him to approximate temperature and time with a linear dependence during the thermal quench.

The quench time  $\tau_Q$  is compared to the order parameter relaxation time  $\tau$ , which in a Ginzburg-Landau system at a second order phase transition is of the general form

$$\tau(T) = \tau_0 (1 - T/T_c)^{-1}. \quad (2)$$

In superfluid <sup>3</sup>He,  $\tau_0$  is on the order of  $\tau_0 \sim \xi_0/v_F$ , where  $\xi_0$  is the zero temperature limiting value of the temperature ( $T$ ) and pressure ( $P$ ) dependent superfluid coherence length  $\xi(T, P)$ . Close to  $T_c$ , it is of the form  $\xi(T, P) = \xi_0(P)(1 - T/T_c)^{-1/2}$ . The second quantity,  $v_F$ , is the velocity of the thermal quasiparticle excitations which are excited above the superfluid energy gap.

As sketched in Fig. 1, this means that below  $T_c$  the order parameter coherence spreads out with the velocity  $c(T) \sim \xi/\tau = \xi_0 (1 - T/T_c)^{1/2}/\tau_0$ . The freeze-out of defects occurs at  $t = t_{\text{Zurek}}$ , when the causally disconnected regions have grown together and superfluid coherence becomes established in the whole volume. At the

<sup>1</sup>1 Mpc = 10<sup>6</sup> parsec = 3.262·10<sup>6</sup> light years.

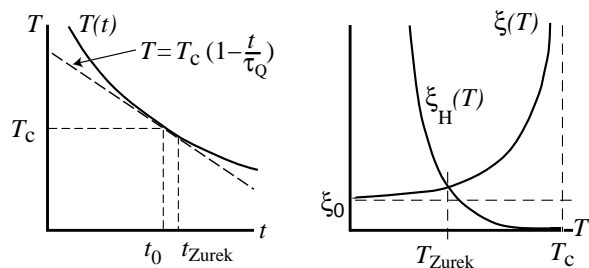


FIG. 1. Principle of KZ mechanism. Rapid thermal quench through  $T_c$ : (Left) Temperature  $T(t)$  and its linear approximation  $T = T_c(1 - t/\tau_Q)$  during the quench, as a function of time  $t$ . (Right) Superfluid coherence length  $\xi(T)$  and order parameter relaxation time  $\tau(T)$  diverge at  $T_c$ . At the freeze-out point  $t_{\text{Zurek}}$ , when phase equilibrium is achieved, the edge of the correlated region, the causal horizon, has moved out to a distance  $\xi_H(t_{\text{Zurek}})$ , which has to equal the coherence length  $\xi(t_{\text{Zurek}})$ .

freeze-out temperature  $T(t_{\text{Zurek}}) < T_c$ , the causal horizon has travelled the distance  $\xi_H(t_{\text{Zurek}}) = \int_0^{t_{\text{Zurek}}} c(T) dt = \xi_0 \tau_Q (1 - T_{\text{Zurek}}/T_c)^{3/2} / \tau_0$  which has to be equal to the coherence length  $\xi(t_{\text{Zurek}})$ . This condition establishes the freeze-out temperature  $T_{\text{Zurek}}/T_c = 1 - \sqrt{\tau_0/\tau_Q}$  at the freeze-out time  $t_{\text{Zurek}} = \sqrt{\tau_0 \tau_Q}$ , when the domain size has reached the value

$$\xi_v = \xi_H(t_{\text{Zurek}}) = \xi_0 (\tau_Q/\tau_0)^{1/4}. \quad (3)$$

In superfluid  $^3\text{He}$  we may have  $\xi_0 \sim 20$  nm,  $\tau_0 \sim 1$  ns, and in the best cases a cool-down time of  $\tau_Q \sim 1$   $\mu\text{s}$  can be reached. From these values we expect the domain structure to display a characteristic length scale of order  $\xi_v \sim 0.1$   $\mu\text{m}$ . Assuming a  $U(1)$ -symmetry-breaking transition, where vortex lines are formed at the domain boundaries, the average inter-vortex distance and radius of curvature in the randomly organized vortex network is on the order of the domain size  $\xi_v$ . In general, we can expect a rapid quench to lead to an initial defect density (defined as vortex length per unit volume)

$$l_v = \frac{1}{a_l \xi_v^2}, \quad (4)$$

where the numerical factor  $a_l \sim 1 - 100$  depends on the details of the model system. Numerical simulation calculations (Ruutu et al. 1998a) give  $a_l \approx 2$  for  $^3\text{He-B}$ . In this system with global symmetry and negligible thermal fluctuations the Kibble-Zurek (KZ) model of defect formation can be expected to work well. Moreover, Ginzburg-Landau theory provides a good description close to  $T_c$  and might lead via microscopic calculations to more rigorous predictions even on a time-dependent phase transition.

## 2.4. Experimental verification of KZ mechanism

The predictions of the KZ model have been tested in numerous numerical experiments under varying conditions (cf. Bettencourt et al. 2000). Laboratory experiments are fewer and their results are less conclusive.

The first experiments were performed on liquid crystals (Chuang et al. 1991; Bowick et al. 1994), where the transition from the isotropic to the nematic phase was examined. This is a weakly first order transition of rod-like molecules from a disordered to an ordered state, where defects of different dimensionalities can be formed. The results were generally found to be consistent with the KZ interpretation. However, a liquid-crystal transition at room temperature is rather different from the ideal KZ case.

The first experiments on coherent quantum systems were started with liquid  $^4\text{He}$  (Hendry et al. 1994), by releasing the pressure on a convoluted phosphor-bronze bellows so that the sample expanded from the normal liquid through the  $\lambda$  transition into the superfluid phase. For a mechanical pressure system the quench time is of order  $\tau_Q \sim 10$  ms. The depressurization is followed by a dead time of similar length, which is required for damping down the vibrations after the mechanical shock. The vortex density after the transition is determined from the attenuation in second sound propagation through bulk liquid. Expansion of  $^4\text{He}$  across the  $T_\lambda(P)$  line (which has negative slope in the  $(P, T)$  phase diagram) requires careful elimination of all residual flow which might result from the expansion itself, foremost the flow out of the filling capillary of the sample cell, but also that around the convolutions of the bellows. Such flow will inevitably exceed the critical velocities, which approach zero at  $T_\lambda$ , and leads to vortex nucleation (Sec. 2.6.1). After the initial attempts, where vortices were detected but a fill line was still present, later much improved measurements failed to yield any evidence of vortex line production, in apparent contradiction with the KZ prediction (Dodd et al. 1998).

The early  $^4\text{He}$  expansion experiments were analyzed by Gill and Kibble (1996) who concluded that the initially detected vortex densities were unreasonably large and must have originated from extrinsic effects, most likely created by the flow out the fill line. The absence of vorticity in the later results was shown not to be evidence against the KZ mechanism (Karra and Rivers 1998; Rivers 2000): Although the pressure drop in expansion cooling is large, 20 – 30 bar, the change in relative temperature  $\epsilon = 1 - T/T_\lambda$  is small,  $|\Delta\epsilon| < 0.1$ . The final temperature  $\epsilon_f < 0.06$  is below  $T_\lambda$  but still above the Ginzburg temperature  $T_G$ , ie. in the regime where thermal fluctuations might be sufficiently effective to wipe out domain formation. Here  $T_G$  is defined as the temperature at which  $k_B T_G$  equals the energy of a vortex

loop of the size  $\xi_v$ , which is expected after the quench according to Eq. (3). Thus the current view about the  $^4\text{He}$  expansion experiments holds that the vortices decay away before the observation switches on (Rivers 2000; Hendry et al. 2000).

Simultaneously with the  $^4\text{He}$  expansion experiments, measurements of quite different nature were carried out in  $^3\text{He-B}$  (Ruutu et al. 1996a; Bäuerle et al. 1996). Here a detailed comparison with the KZ predictions was achieved. These efforts were followed by measurements of thermal quenches through the superconducting transition in different superconducting geometries.

The most conclusive results have been obtained with high- $T_c$  YBCO films (Maniv et al. 2003). The film is heated above its transition temperature of 90 K with a laser pulse. The hot film is then cooled from below back to the ambient temperature of 77 K. This happens laterally uniformly through the contact with an optically transparent substrate of much larger thickness and heat capacity. The maximum cooling rate was measured to be  $10^8$  K/s, by monitoring the electrical resistance of the film. The total net flux, which remains frozen in the pinning sites of the YBCO film after the transition, was measured with a sensing coil below the substrate and connected to a SQUID magnetometer. This flux was found to display very weak dependence on the cooling rate, as predicted by the KZ scaling theory.

As discussed by Kibble and Rajantie (2003), the important information to obtain from such measurements would be the spatial distribution of the flux quanta in the film. Spatial correlations between the fluxoids would support the KZ mechanism, if the vortices were found to display negative correlations, i.e. neighboring vortices would prefer to have opposite signs. A competing mechanism involves thermal fluctuations of the magnetic field which generates vortices during the quench cooling through  $T_c$  where the critical field vanishes:  $H_{c2} \rightarrow 0$ . This second mechanism is predicted to display positive correlations, i.e. vortices of same sign would tend to cluster. An analogous situation arises in the  $^3\text{He-B}$  experiments which will be described below. Here at temperatures below 3 mK thermal fluctuations are not important since any energy barriers will generally automatically be orders of magnitude higher. Nevertheless, even in these conditions a phenomenon can be identified which competes with the KZ mechanism (which is a volume effect). This involves the phase boundary between the normal liquid and  $^3\text{He-B}$  (a surface effect) if a phase boundary exists in the presence of flow. The reason is again that at  $T_c$  the critical velocity for vortex formation vanishes:  $v_c \rightarrow 0$ .

In superconductors a measurement with spatial resolution and single-fluxoid sensitivity has been recently accomplished (Kirtley et al. 2003). Here a scanning SQUID microprobe is used to map the flux quanta trapped in an amorphous  $\text{Mo}_3\text{Si}$  film which had been lithographically

patterned in ring-like elements. Unfortunately, in this measurement the cooling rate was limited to  $\sim 20$  K/s at the  $T_c = 7.8$  K of the film and the detected quantized flux was concluded to originate from a thermally activated process.

These examples illustrate the difficulties in attempting to find experimental proof for the KZ process. The KZ mechanism is intuitively easy to accept, but its experimental verification is complicated and involves careful considerations. In a phase transition defect formation is more usual than its absence. In most experiments both extrinsic and intrinsic sources of vortex formation are present and compete in actual vortex generation. For instance, even slow cooling of liquid  $^4\text{He}$  across the  $\lambda$  transition is known to produce primordial vortices which remain pinned as remanent vorticity on the walls of the container (Awschalom and Schwarz 1984). There are no claims in the literature yet that an experiment would have produced a perfectly vortex-free bulk sample of superfluid  $^4\text{He}$ .

A second point to note is that the KZ model describes a second order transition where the energy barrier, which separates the symmetric high-temperature phase from the broken-symmetry states at low-temperatures, vanishes at  $T_c$ . Thus the transition becomes an instability. A first order transition is different: Here the barrier remains finite and the low temperature phase has to be nucleated, usually by overcoming the barrier via thermal activation. Nucleation may occur in different parts of the system nearly simultaneously, depending on the properties of the system, the fluctuations, the quench time  $\tau_Q$ , and the nucleation mechanism. Such a situation, which often is called bubble nucleation, also leads to domain formation and to a final state which is qualitatively similar to that expected after the second order transition and the KZ mechanism.

In all of the experimental examples listed above, other mechanisms are also possible which might replace or operate in parallel to the KZ process. The differences are subtle, as we shall see in Sec. 2.8 for  $^3\text{He-B}$  or as has been emphasized for superconductors by Rajantie (2001). In practice measurements differ from the original KZ model, i.e. from a homogeneous transition, which occurs simultaneously in the whole system and where there are no gradients in density or temperature. In practical measurements on bulk material a rapid quench through the transition is often forced by strong gradients. On some level gradients will always appear in any laboratory system and their influence has to be investigated.

Superfluid  $^3\text{He}$  measurements have so far established the most quantitative comparison to the KZ scaling theory (Ruutu et al. 1996a; Bäuerle et al. 1996). A happy coincidence of many valuable features has made this possible: A reduced likelihood of defect formation from extrinsic sources, the virtual absence of remanent vorticity,

the possibility to perform thermal quenches in microseconds, the presence of a pure second order phase transition, and the availability of measuring methods to detect different types of defects, often with a resolution of one single defect. A critical discussion of these questions is presented below.

The search for firm proof of the KZ mechanism has grown to an important topic in condensed matter physics. The reason is that it provides (at least superficially) easy interpretation of the fastest non-equilibrium phase transitions. Amusingly this question does not enjoy similar interest any more in cosmology where the problem was born. Measurements of the anisotropy in the cosmic microwave background radiation with the WMAP satellite (with an angular resolution  $\sim 0.25^\circ$  and an amplitude sensitivity  $\sim 1 \mu\text{K}$ ) have concluded that the angular distribution of the anisotropy expanded in its harmonic components gives a multipole expansion with a sharp dominating peak at  $\ell \sim 200$ , which corresponds to an angular scale  $\sim 1^\circ$  (Bennett et al. 2003; Spergel et al. 2003). This distribution can be fit with models which are based on inflationary expansion of the Early Universe, *i.e.* with models with an early period of accelerated expansion. In contrast, topological defects, such as cosmic strings, are expected to generate a clearly different broader peak. These two different scenarios have been the ruling contenders as the explanation for the origin of large-scale structure. Thus at present time the KZ mechanism appears to survive only in condensed matter physics.

## 2.5. Principle of superfluid $^3\text{He}$ experiments

To study reliably defect formation in a quench-cooled transition, two basic requirements are the following: First, the transition can be repeated reproducibly, and second, a measurement is required to detect the defects after their formation, either before they annihilate or by stabilizing their presence with a bias field. Both of these requirements can be satisfied in  $^3\text{He}$  experiments.

### 2.5.1. Outline of experimental method

A schematic illustration of one set of experiments (Ruutu et al. 1996a) is depicted in Fig. 2. The top part displays the events which are controlled by the observer in the laboratory. A cylindrical container filled with superfluid  $^3\text{He-B}$  is rotated at constant velocity  $\Omega$ . The velocity of rotation is maintained below the critical value at which quantized vortex lines are spontaneously formed. In other words, the initial state is one of metastable vortex-free counterflow of the superfluid and normal components in constant conditions.

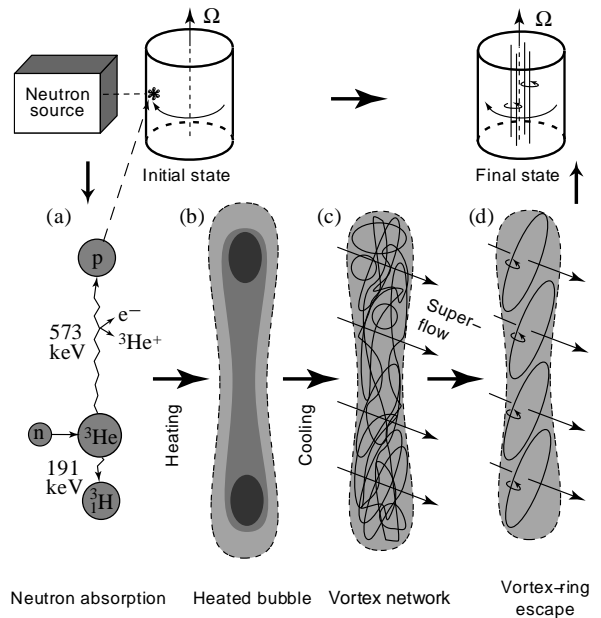


FIG. 2. Principle of the quench-cooled rotating experiment in superfluid  $^3\text{He-B}$ : (Top) A cylindrical sample container with superfluid  $^3\text{He-B}$  is rotated at constant angular velocity  $\Omega$  and temperature  $T$ , while the NMR absorption is monitored continuously. When the sample is irradiated with neutrons, vortex lines are observed to form. (Bottom) Interpretation of the processes following a neutron absorption event in bulk superflow; see the text for details. (From Ruutu et al. 1996a).

Next a weak source of thermal neutrons is placed in the vicinity of the  $^3\text{He}$  sample. If the rotation velocity is sufficiently high, then vortices start to appear at a rate which is proportional to the neutron flux. The neutron source is positioned at a convenient distance  $d$  from the cryostat so that vortex lines are observed to form in well-resolved individual events. The experimental signal for the appearance of a new vortex line is an abrupt jump in NMR absorption. An example, measured at low rotation, is shown by the lower recorder trace in Fig. 3.

The lower part of Fig. 2 shows in more detail what is thought to happen within the superfluid. Liquid  $^3\text{He}$  can be locally heated with the absorption reaction of a thermal neutron:  $n + ^3_2\text{He} \rightarrow p + ^3_1\text{H} + E_0$ , where  $E_0 = 764$  keV. The reaction products, a proton and a triton, are stopped by the liquid and produce two collinear ionization tracks (Meyer and Sloan 1997). The ionized particles, electrons and  $^3\text{He}$  ions, diffuse in the liquid to recombine such that 80% or more of  $E_0$  is spent to heat a small volume with a radius  $R_b \sim 50 \mu\text{m}$  from the superfluid into the normal phase. The rest of the reaction energy escapes in the form of ultraviolet emission (Stockton et al. 1971; Adams et al. 1995) and, possibly, in the form of long-living molecular  $^3\text{He}_2^*$  excitations (Keto et al. 1974; Kafanov et al. 2000), which partially relax at the walls of the container.

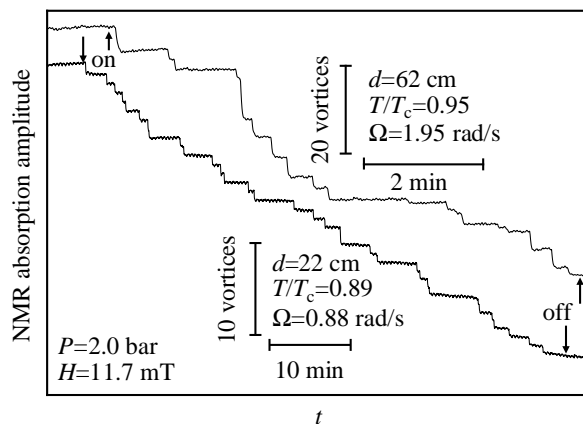


FIG. 3. Peak height of the NMR signal which monitors the velocity of the bias flow from rotation (the so-called counterflow peak in the NMR absorption spectrum of  $^3\text{He-B}$ ), shown as a function of time  $t$  during neutron irradiation. The lower trace is for a low and the upper trace for a high value of rotation velocity  $\Omega$ . The initial state in both cases is metastable vortex-free counterflow. The vertical arrows indicate when the neutron source was turned on/off. Each step corresponds to one neutron absorption event and its height, when compared to the adjacent vertical calibration bar, gives the number of vortex lines formed per event. The distance of the neutron source from the sample is denoted with  $d$ . (From Ruutu et al. 1996b).

For measurements in rotating  $^3\text{He}$ , neutron absorption is an ideal heating process. For slow neutrons from a room temperature source with a Maxwellian distribution (at  $20.4^\circ\text{C}$  or  $0.0253\text{eV}$ ) the velocity at the peak of the distribution is  $2200\text{m/s}$ . The capture cross section of the  $^3\text{He}$  nucleus for these neutrons is huge:  $5327 \pm 10\text{ barn} = 5.3 \cdot 10^{-21}\text{ cm}^2$  (Beckurts and Wirtz 1964). This means a short mean free path of about  $100\ \mu\text{m}$ . Thus most neutrons are absorbed within a close distance from the wall, although still within the bulk liquid, but such that the velocity of the applied counterflow is accurately specified. In other parts of the refrigerator neutron absorption is negligible and thus the temperature of the  $^3\text{He}$  sample can be maintained stable during the irradiation. Finally, the cooling is fast, as the small volume heated by the neutron absorption event is embedded in the cold bulk system.

Subsequently, the normal liquid in the heated neutron bubble cools back through  $T_c$  in microseconds. The measurements in Fig. 3 demonstrate that vortex lines are indeed created in this process. Vortex loops, which form within a cooling neutron bubble in the bulk superfluid, would normally contract and disappear in the absence of rotation. This decay is brought about by the inter-vortex interactions between the vortex filaments in the presence of dissipation from mutual friction between the normal and superfluid components. In rotation the externally

applied counterflow provides a bias which causes sufficiently large loops to expand to rectilinear vortex lines and thus maintains them for later detection. In the rotating experiments in Helsinki these rectilinear vortex lines are counted with NMR methods (Ruutu et al. 1996a, 1998a; Finne et al. 2004a).

In a second series of  $^3\text{He}$  experiments, performed in Grenoble (Bäuerle et al. 1996, 1998a) and Lancaster (Bradley et al. 1998), the vortices formed in a neutron absorption event are detected calorimetrically with very-low-temperature techniques. In the zero temperature limit mutual friction becomes exponentially small and the life time of the vorticity might be very long, even if there is no flow. In this situation the existence of the vorticity can be resolved as a deficit in the energy balance of the neutron absorption reaction.

### 2.5.2. Interpretation of $^3\text{He}$ experiments

Several alternative suggestions can be offered on how to explain these observations. The KZ model is one of them. Whatever the mechanism, the superfluid transition in a localized bubble represents a new process for creating vortex rings. This phenomenon is associated with one of the fastest 2nd order phase transition, which has been probed. It takes place in the bulk superfluid and not in immediate contact with a solid wall, where most other vortex formation processes occur in the presence of applied counterflow.

The KZ interpretation of the later stages of the experiment is contained in the two illustrations marked as (c) and (d) in Fig. 2. First a random vortex network (c) is created while cooling through  $T_c$ . Next the network starts to evolve under the influence of inter-vortex interactions and the applied flow. At high temperatures the process is highly dissipative, owing to the large mutual friction force which connects the superfluid and normal fractions and acts on a moving vortex. The average inter-vortex distance increases, small loops are smoothed out, and the network becomes rarefied or “coarse grained”. Also reconnections, which take place when two lines cross, contribute to the rarefaction. The applied flow favors the growth of loops with the right winding direction and orientation. It causes sufficiently large loops to expand, while others contract or reorient themselves with respect to the flow. The final outcome is that correctly oriented large loops (d), which exceed a critical threshold size, start expanding spontaneously as vortex rings, until they meet the chamber walls. There the superfluous sections of the ring will annihilate and only a rectilinear vortex line will finally be left over. It is pulled to the center of the container, where it remains in stationary state parallel to the rotation axis, stretched between the top and bottom surfaces.



This picture applies at high temperatures in  $^3\text{He-B}$  where Kelvin-wave excitations on vortices are exponentially damped and spontaneous loop formation on existing vortices does therefore not occur. In this situation the number of vortex rings, which are extracted from the neutron bubble (Fig. 2d), remains conserved during the later expansion. Thus the number of rectilinear vortex lines, the end result from the neutron absorption event, characterizes the extraction process as a function of the applied bias velocity. This situation is very different from that in  $^4\text{He-II}$  where mutual friction damping never reaches this high values (except extremely close to  $T_\lambda$ ).

Very different time scales are at work in this process of vortex formation. Except for the retarded molecular excitations, the heating from the initial ionization and subsequent recombination is limited by the diffusion of charges in the liquid and takes place much faster than the thermal recovery. The initial vortex network forms during cooling through  $T_c$ , for which the relevant time scale is microseconds. The later evolution of the network and the loop escape happen again on a much slower time scale, namely from milliseconds up to seconds, since here the vortex motion is governed by the mutual-friction-dependent superfluid hydrodynamics.

## 2.6. Measurement of vortex lines in $^3\text{He-B}$

There are two major phases of superfluid  $^3\text{He}$ , the A and B phases (Fig. 14). The neutron measurements have been performed in the quasi-isotropic  $^3\text{He-B}$ . In the present context we may think of vortices in  $^3\text{He-B}$  as being similar to those in superfluid  $^4\text{He-II}$ , where only the  $U(1)$  symmetry is broken and the order parameter is of the general form  $\Psi = |\Psi(T)| e^{i\Phi(\mathbf{r})}$ : The vortices are topologically stable, have a singular core, inside of which  $|\Psi|$  deviates from its bulk value, while outside the phase  $\Phi$  changes by  $2\pi\nu$  on a closed path which encircles the core. A persistent superfluid current is trapped as a single-quantum circulation ( $\nu = 1$ ) around the core, with the circulation quantum  $\kappa = h/(2m_3) \simeq 0.0661 \text{ mm}^2/\text{s}$  and a superflow velocity  $\mathbf{v}_{\text{s,vortex}} = \kappa/(2\pi) \nabla\Phi = \kappa/(2\pi r) \hat{\phi}$ .

### 2.6.1. Critical velocity of vortex formation

The energy of a single rectilinear vortex line, aligned along the symmetry axis of a rotating cylindrical container of radius  $R$  and height  $Z$ , consists primarily of the hydrodynamic kinetic energy stored in the superfluid circulation trapped around the core,

$$E_v = \frac{1}{2} \int \rho_s v_{\text{s,vortex}}^2 dV = \frac{\rho_s \kappa^2 Z}{4\pi} \ln \frac{R}{\xi} . \quad (5)$$

Here the logarithmic ultraviolet divergence has been cut off with the core radius, which has been approximated with the coherence length  $\xi$ . If the container rotates at an angular velocity  $\Omega$ , the state with the first vortex line becomes energetically preferred when the free energy  $E_v - \Omega L_z$  becomes negative. The hydrodynamic angular momentum from the superflow circulating around the vortex core is given by

$$L_z = \int \rho_s r v_{\text{s,vortex}} dV = \rho_s \kappa R^2 Z . \quad (6)$$

One finds that  $E_v - \Omega L_z < 0$ , when the velocity  $\Omega R$  of the cylinder wall exceeds the Feynman critical velocity,  $v_{c1} = \kappa/(2\pi R) \ln(R/\xi)$ . With a container radius  $R$  of a few mm, the Feynman velocity is only  $\sim 10^{-2} \text{ mm/s}$ . However, if we can exclude remanent vorticity and other extrinsic mechanisms of vortex formation (which is generally the case in  $^3\text{He-B}$  at temperatures  $T > 0.6 T_c$ , but not in  $^4\text{He-II}$ ), then vortex-free superflow will persist as a meta-stable state to much higher velocities because of the existence of a finite nucleation energy barrier.

The height of the nucleation barrier decreases with increasing velocity. In  $^4\text{He-II}$  intrinsic vortex formation is observed in superflow through submicron-size orifices. Here the barrier is ultimately at sufficiently high velocities overcome by thermal activation or at low temperatures by quantum tunnelling (Packard 1998; Varoquaux et al. 1998). The other possibility is that the thermodynamic stability limit of the superfluid is reached (Andreev and Melnikovsky 2003). In  $^3\text{He-B}$  the barrier is unpenetrably high in practically any situation and the flow velocity has to be increased to the point where the barrier approaches zero. Vortex formation then occurs in the form of an instability which takes place locally at some sharp asperity on the cylindrical wall of the rotating sample where the stability limit of superflow is first reached (Parts et al. 1995; Ruutu et al. 1997a). The average velocity at the cylindrical container wall we call the spontaneous critical velocity  $v_c(T, P)$  (Fig. 13), which now depends on surface roughness and is therefore container specific. When the instability occurs and a vortex is formed, the actual local velocity at the critical dominating asperity equals the intrinsic bulk instability velocity  $v_{cb}(T, P)$ .

When the flow reaches the instability value  $v_{cb}$  at the dominating sharpest protrusion, a segment of a vortex ring is formed there. The energy of the smallest possible vortex ring, which has a radius comparable to the coherence length, is of order  $E_v \sim \rho_s \kappa^2 \xi$ . This energy constitutes the nucleation barrier. On dimensional grounds we may estimate that  $E_v/(k_B T) \sim (\xi/a)(T_F/T)$ , where  $T_F = \hbar^2/(2m_3 a^2) \sim 1\text{K}$  is the degeneracy temperature of the quantum fluid and  $a$  the interatomic spacing. In  $^4\text{He-II}$  the coherence length is of order  $\xi \sim a$  and the temperature  $T \sim T_F$ , which means that  $E_v/(k_B T) \sim 1$  and thermally activated nucleation becomes possible.

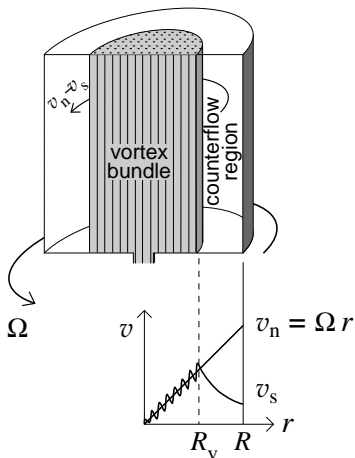


FIG. 4. (Top) Metastable state with a central vortex cluster in the rotating cylinder. This axially symmetric arrangement consists of rectilinear vortex lines surrounded by vortex-free counterflow. (Bottom) Radial distribution of the velocities of the superfluid component,  $v_s$ , and the normal component,  $v_n$ . Because of its large viscosity, the normal fraction corotates with the container. (From Krusius et al. 1994).

In contrast in  $^3\text{He-B}$  the coherence length is more than 10 nm and we find  $E_v/(k_B T) \sim 10^5$  at temperatures of a few mK or less. The consequence from such an enormous barrier is that both thermal activation and quantum tunnelling are out of question as nucleation mechanisms. The only remaining intrinsic mechanism is a hydrodynamic instability, which develops at rather high velocity. This fact has made possible the measurement of neutron-induced vortex formation as a function of the applied flow velocity  $v < v_c$ .

### 2.6.2. Rotating states of the superfluid

When a container with superfluid is set into rotation and the formation of vortex lines is inhibited by a high energy barrier, then the superfluid component remains at rest in the laboratory frame. Its velocity is zero in the whole container:  $v_s = 0$ . The normal component, in contrast, corotates with the container and  $v_n = \Omega r$ . This state of vortex-free counterflow is called the Landau state. It corresponds to the Meissner state in superconductors, with complete flux expulsion.

In  $^4\text{He-II}$  vortex-free flow with sufficiently high velocity is out of reach in most situations, because even at very low velocities remanent vorticity leads to efficient vortex formation. In  $^3\text{He-B}$  the superfluid coherence length is several orders of magnitude larger and remanent vorticity can be avoided if the container walls are sufficiently smooth. Coupled with a high nucleation barrier, metastable rotating states then become possible. These can include an arbitrary number  $N$  of rectilinear vortex

lines, where  $N \leq N_{\text{max}}$ . In most experimental situations the maximum possible vortex number,  $N_{\text{max}}$ , equals that in the equilibrium vortex state,  $N_{\text{eq}} \approx 2\pi\Omega R^2/\kappa$ . The equilibrium vortex state is obtained by cooling the container slowly at constant  $\Omega$  through  $T_c$ .

If the number of lines is smaller than that in the equilibrium state, then the existing vortex lines are confined within a central vortex cluster, as shown in Fig. 4. The confinement comes about through the Magnus force from the normal-superfluid counterflow,  $v = v_n - v_s$ , which circulates around the central cluster in the vortex-free region. Within the cluster mutual repulsion keeps the lines apart such that they form a triangular array at the equilibrium density,  $n_v = 2\Omega/\kappa$ , which is constant over the transverse cross section of the cluster. At this line density the cluster corotates with the container at constant  $\Omega$ , like a solid body. The total number of lines is given by  $N = \pi n_v R_v^2$ , where  $R_v$  is the radius of the cluster.

With  $N$  vortex lines in the cluster, the superflow velocity outside has the value  $v_s = \kappa N/(2\pi r)$ , which is equivalent to that around a giant vortex with  $N$  circulation quanta  $\kappa$  (Fig. 4). The counterflow velocity  $v$  vanishes inside the cluster (measured on length scales which exceed the inter-vortex distance), while outside it increases from zero at  $r = R_v$  to its maximum value at the cylinder wall,  $r = R$ :

$$v(R) = \Omega R - \frac{\kappa N}{2\pi R}. \quad (7)$$

In the absence of the neutron source, new vortex lines are only formed if  $v(R)$  is increased to its container-dependent spontaneous critical value  $v_c(T, P)$ .

### 2.6.3. Experimental setup

Fig. 5 shows a measuring setup for rotating NMR measurements in  $^3\text{He-B}$ . The cylindrical sample is connected via an orifice to a long liquid  $^3\text{He}$  column which is needed to fill the sample volume, to provide the thermal contact with the nuclear refrigeration stage, and to isolate the sample in a metal-free environment for NMR measurement. The major resistances in the thermal path between the sample and the nuclear cooling stage are the orifice, the liquid column, and the Kapitza surface resistance of the porous sintered heat exchanger in a large liquid volume below the column. The most important characteristic of the sample container itself is its spontaneous critical velocity  $v_c(T, P)$ , which may depend in complicated ways on temperature and pressure, since different sources contribute to vortex formation. These arise from (i) the surface roughness of the cylindrical walls in the volume above the orifice, (ii) sites in which remanent vortices can be trapped, and (iii) the leakage of vortices through the orifice (since the volume in contact with the

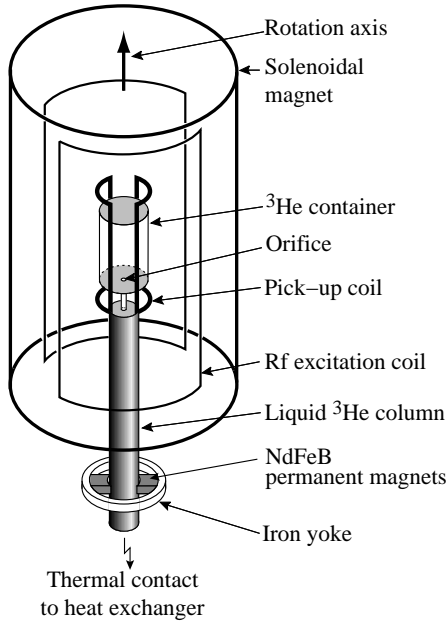


FIG. 5. Liquid  $^3\text{He}$  sample container with coils for NMR measurement. The cylindrical sample on the top is connected via a narrow aperture with a long liquid  $^3\text{He}$  column which serves as a thermal path to the sintered heat exchanger on the nuclear refrigeration stage. The nuclear stage is located below this structure while the mixing chamber of the pre-cooling dilution refrigerator is above. The excitation coil and the outer magnet have not been drawn to scale. (From Ruutu et al. 1997a).

rough heat exchanger surfaces will be filled with the equilibrium number of vortices already at low  $\Omega$ ). In practice for a clean quartz cylinder the most important source is some isolated surface protrusion, a localized defect or a piece of dirt, which increases the flow velocity at a sharp asperity by up to an order of magnitude (Parts et al. 1995; Ruutu et al. 1997a). To achieve a high critical velocity, the geometry and surface quality of the sample container are of utmost importance.

The sample container structure in Fig. 5 is prepared from fused quartz. The sample cylinder itself has a radius  $R = 2.5\text{ mm}$ , length  $Z = 7\text{ mm}$ , and wall thickness  $0.5\text{ mm}$ . An orifice of  $0.5\text{ mm}$  diameter links it with the  $60\text{ mm}$  long connecting column. The long length is needed to place the sample in the middle of the NMR polarization magnet. The container is fused together from tubular and flat plate parts in an oxygen-acetylene flame. After assembly the structure is annealed in an oven, etched, and cleaned with solvents. All indications point to an average surface roughness well below  $1\ \mu\text{m}$ , such that it is dirt particles and perhaps isolated localized defects on the glass surface which ultimately control the critical velocity. For the quartz glass cylinder in Fig. 5 the spontaneous critical velocity  $v_c$  was found to be a

factor of three or more larger than the lowest velocity  $v_{\text{cn}}(T, P)$  at which vortices start to appear in neutron irradiation (cf. Fig. 13).

The non-invasive continuous-wave NMR measurement is conducted from the outside with a system of three orthogonal superconducting coils. The innermost is a saddle-shaped detector coil, wound from  $25\ \mu\text{m}$  solid Nb wire on a thin epoxy shell and mounted directly on the sample cylinder. It is thermally anchored to a Cu strip to the nuclear cooling stage. The outermost coil is a magnet which produces the axially oriented homogeneous polarization field. This end-compensated solenoid on a bronze body is fixed mechanically and thermally to the mixing chamber. The coil in the middle is used for rf excitation. It consists of two turns in each half and is fixed inside the polarization magnet. All parts shown here are located inside a superconducting Nb shield, to avoid interference from the demagnetization field which is required for cooling and temperature stabilization. The Nb jacket is part of the heat shield which is fixed to the mixing chamber.

The neutron source is a weak  $^{241}\text{Am}/\text{Be}$  specimen which is sandwiched between two paraffin moderator tiles so that a cubic box results with sides of  $25\text{ cm}$  length. For irradiation the box is carried to the cryostat and placed at room temperature at a desired distance from the  $^3\text{He}$  sample. By varying this distance the neutron flux can be adjusted to the required low value, as determined from the vortex formation rate  $\dot{N}$  in Fig. 8. Between measurements the source is moved a fair distance away from the cryostat ( $\sim 25\text{ m}$ ).

#### 2.6.4. NMR measurement

The unusual NMR properties of the  $^3\text{He}$  superfluids are a direct consequence from the Cooper pairing in states with spin  $S = 1$  and orbital momentum  $L = 1$ . In  $^3\text{He-B}$  the NMR absorption spectrum, recorded at low rf excitation with traditional transverse cw methods, is related to the spatial distribution of the order parameter orientation in the rotating cylinder. Spin-orbit coupling, although weak, is responsible for the large frequency shifts which give rise to absorption peaks shifted from the Larmor frequency (Vollhardt and Wölfle 1990). The height of the so-called *counterflow* (CF) peak, which depends on the CF velocity around the vortex cluster, can be used to determine the number of rectilinear vortex lines in the cluster.

In the left panel of Fig. 6 NMR absorption spectra are shown, which have been recorded at the same  $\Omega$ , but with a different number  $N$  of vortex lines in the vortex cluster. In the vortex-free state the large CF peak on the right increases rapidly with  $\Omega$  when the orienting effect from the CF grows. The absorption intensity for this

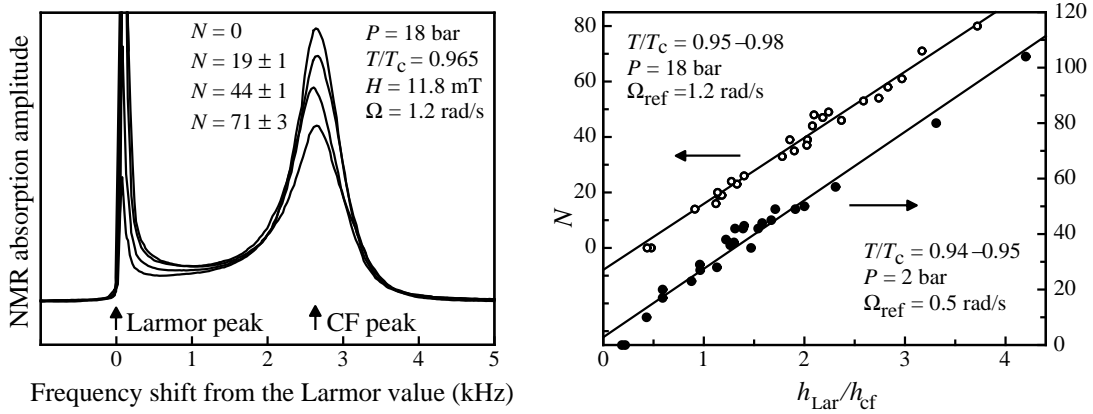


FIG. 6. NMR measurement of vortex lines in superfluid  ${}^3\text{He-B}$ , when rotated in a long cylinder with the magnetic field oriented axially: (*Left*) NMR spectra recorded at a reference velocity  $\Omega_{\text{ref}} = 1.2$  rad/s with different number of vortex lines  $N$ . The Larmor frequency is at the left and the counterflow peak at the right vertical arrow. (*Right*) Two calibration measurements of the number of vortex lines  $N$  as a function of the ratio of the Larmor and counterflow peak heights,  $h_{\text{Lar}}/h_{\text{cf}}$ , measured at two different rotation velocities  $\Omega_{\text{ref}}$ . (From Xu et al. 1996).

growth in peak height is shifted from the asymmetric peak on the left close to the *Larmor* frequency. This second peak reflects the order parameter orientation in the center of the container in the region of the vortex cluster. At fixed  $\Omega$ , if more vortex lines are added, the central vortex cluster expands, the CF velocity outside the cluster is reduced, and the absorption intensity from the CF peak is shifted back to the Larmor peak (Kopu et al. 2000).

The frequency shift of the CF peak increases monotonically with decreasing temperature and is used to measure the temperature. The total integrated absorption in the NMR spectrum is proportional to the B phase susceptibility  $\chi_{\text{B}}(T, P)$  and decreases rapidly with temperature. However, by maintaining the CF peak at fixed frequency shift, the temperature is kept stable, and the relative amount of absorption in the Larmor and CF peaks can then be used to determine the number of vortex lines. By monitoring the peak height of either of the two absorption maxima, one can detect a change in  $N$ , as was illustrated in Fig. 3.

In the right panel of Fig. 6 the ratio of the two peak heights has been calibrated to give the vortex number at two different angular velocities  $\Omega_{\text{ref}}$ . In both cases only a relatively small number of vortex lines  $N \ll N_{\text{eq}}$  is present and the CF peak is large (Xu et al. 1996). These calibration plots were measured by starting with an initially vortex-free sample rotating at  $\Omega_{\text{ref}}$ , into which a given number of vortex lines  $N$  was introduced with neutron absorption reactions, as in Fig. 3. After that the irradiation was stopped and the entire NMR spectrum was recorded (by sweeping the magnetic polarization field  $H$ ). From the spectrum the ratio of the peak heights of the two absorption maxima is worked out and plotted versus  $N$ . This gives the linear relationships in Fig. 6.

The reduction in the CF peak height from the addition of one single vortex line can be discerned with good resolution in favorable conditions (Fig. 3). The optimization of this measurement has been analyzed by Kopu et al. (2000). With a small-size superconducting magnet and its modest field homogeneity ( $\Delta H/H \sim 10^{-4}$ ), the best conditions are usually achieved at low magnetic field ( $H \sim 10 - 20$  mT) close to  $T_c$  ( $T \geq 0.8T_c$ ) and at relatively high CF velocity ( $\Omega > 0.6$  rad/s), where the CF peak is well developed (Korhonen et al. 1990). The single-vortex signal, i.e. the change in peak height per vortex line, decreases with increasing  $\Omega$  and CF peak height, as shown in Fig. 7. In neutron irradiation measurements, the rate of vortex line creation  $\dot{N}$  is determined directly from records like the two traces in Fig. 3. The plot in Fig. 7 provides a yard stick for the single-vortex signal, to estimate the number of new lines if multiple lines are created in one neutron absorption event.

## 2.7. Vortex formation in neutron irradiation

A measurement of vortex-line formation in neutron irradiated normal-superfluid counterflow is performed at constant ambient conditions. The externally controlled variables include the rotation velocity  $\Omega$ , temperature  $T$ , pressure  $P$ , magnetic field  $H$ , and neutron flux  $\phi_{\text{n}}$ . The initial state is one of vortex-free counterflow ( $N = 0$ ). When stable conditions have been reached, a weak neutron source is placed at a distance  $d$  from the  ${}^3\text{He-B}$  sample and the output from the NMR spectrometer is monitored, as shown in Fig. 3. From this NMR absorption record as a function of time, the vortex lines can be counted which are formed during a given irradiation period.

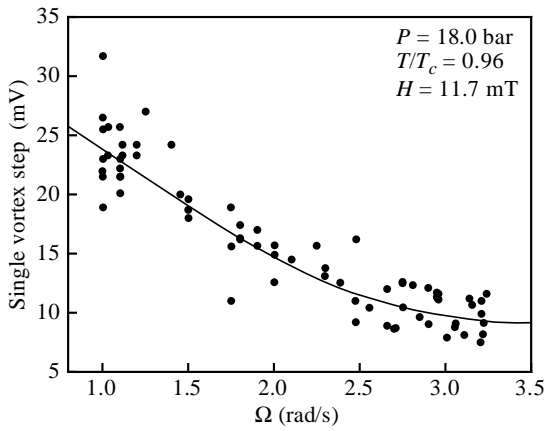


FIG. 7. Absolute magnitude of the single-vortex signal (as in Fig. 3), measured in the vortex-free counterflow state at different  $\Omega$ . The reduction in the height of the counterflow peak is given here in millivolts at the output of the cooled preamplifier which has a gain of  $\approx 10$  and is located inside the vacuum jacket of the cryostat. The scatter in the data arises from residual differences in the measuring temperature, perhaps from small differences in the order-parameter texture from one cool down to the next, and from an electronic interference signal which is generated by the rotation of the cryostat. More details on the NMR spectrometer are given by Parts et al. (1995) and Ruutu et al. (1997a).

The process evidently exhibits stochastic variation. To measure the vortex-formation rate  $dN/dt = \dot{N}$ , records with a sufficiently large number of detected neutron absorption events are analyzed to obtain a representative result. After that one of the experimental parameters is changed and a new run is performed. In this way the dependence of the vortex formation process on the external variables can be studied. It was found that  $\dot{N}$  varies as a function of all the external parameters, i.e. neutron flux, rotation velocity, temperature, pressure, and magnetic field. In the following we shall first describe these empirically established dependences.

The rate of vortex-line formation is proportional to the neutron flux. The latter is varied by changing the distance of the source from the cryostat. In this way individual absorption events can be studied, which are well separated in time. A calibration plot of the measured rate  $\dot{N}$ , as a function of the distance between sample and source, is shown in Fig. 8. By means of this plot the results can be scaled to correspond to the same incident neutron flux, for example with the source at the minimum distance  $d = 22$  cm, which is given by the outer radius of the liquid He dewar.

A most informative feature is the dependence of  $\dot{N}$  on rotation velocity (Ruutu et al. 1996a,b, 1998a). Rotation produces the applied bias velocity at the neutron absorption site. Since the absorption happens close to the wall of the container, the velocity of this bias flow is approxi-

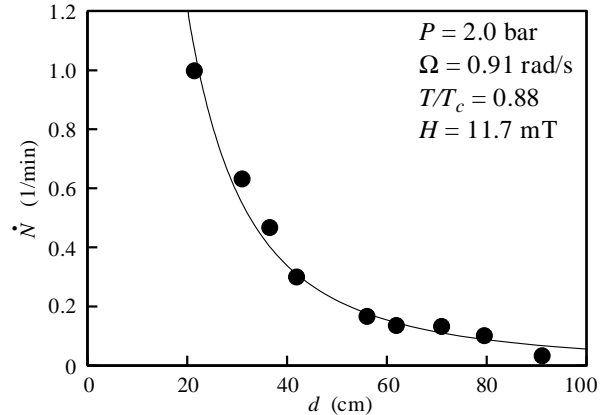


FIG. 8. Rate of vortex-line formation in neutron irradiated counterflow,  $\dot{N}$ , as a function of the distance  $d$  between neutron source and  $^3\text{He-B}$  sample. The initial state for all data points is vortex-free counterflow at a rotation velocity of 0.91 rad/s. The neutron irradiation time is 30 min. The fitted curve is of the form  $\ln[1 + (R_s/d)^2]$ , where  $R_s$  is the radius of the front surface of the paraffin moderator box (perpendicular to  $\mathbf{d}$ ), in which the Am-Be source is embedded.

mately equal to  $v(R)$  (Eq. (7)), the counterflow velocity at the cylinder wall. We shall denote this velocity simply with  $v$ . It depends both on the angular velocity  $\Omega$  and the number of vortex lines  $N(t)$  which are already present in a central cluster. The bias flow provides the force which allows vortex rings to escape from the heated neutron bubble and to expand to rectilinear vortex lines, which are then preserved in the central cluster.

These features can be seen in Fig. 9. It demonstrates that it is the counterflow velocity  $v(N)$ , which is the important variable governing the rate  $\dot{N}$  and not, for instance, that of the normal component,  $v_n(R) = \Omega R$ . Here the total vortex number  $N(t)$  is recorded during neutron irradiation at constant external conditions over a time span of six hours. The irradiation is started from the vortex-free state:  $N(t=0) = 0$ . The rate  $\dot{N}(t)$ , at which vortex lines accumulate in the center of the container, is not constant: Initially both the counterflow velocity and the rate of vortex formation are the highest. When more vortex lines collect in the central cluster, both the velocity  $v$  and the rate  $\dot{N}$  fall off. Finally the vortex number  $N$  approaches a saturation value, beyond which no more lines are formed. This means that there exists a lower limit, a threshold value for the counterflow velocity  $v$ , below which the neutron absorption events produce no vortex lines at all.

The dependence of  $\dot{N}$  on the counterflow velocity  $v$  is obtained from experiments like that in Fig. 9. However, more efficient is a measurement of only the initial slope of the  $N(t)$  record. Typically 15–30 min accumulation periods are then enough. Only a small number of vor-

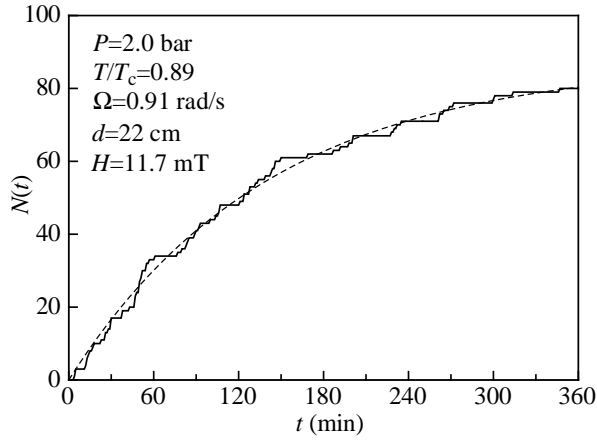


FIG. 9. Cumulative number of vortex lines  $N(t)$  as a function of time  $t$ , after turning on the neutron irradiation at constant flux on an initially vortex-free  $^3\text{He-B}$  sample rotating at constant  $\Omega$ . The dashed curve represents a fit to Eq. (10) with  $\gamma = 1.1 \text{ min}^{-1}$  and  $v_{\text{cn}} = 1.9 \text{ mm/s}$ . The result demonstrates that the rate of vortex-line formation is controlled by the counterflow velocity  $v(N)$  and not by that of the normal component  $v_n(R) = \Omega R$ , which is constant during this entire measurement. (From Ruutu et al. 1996b).

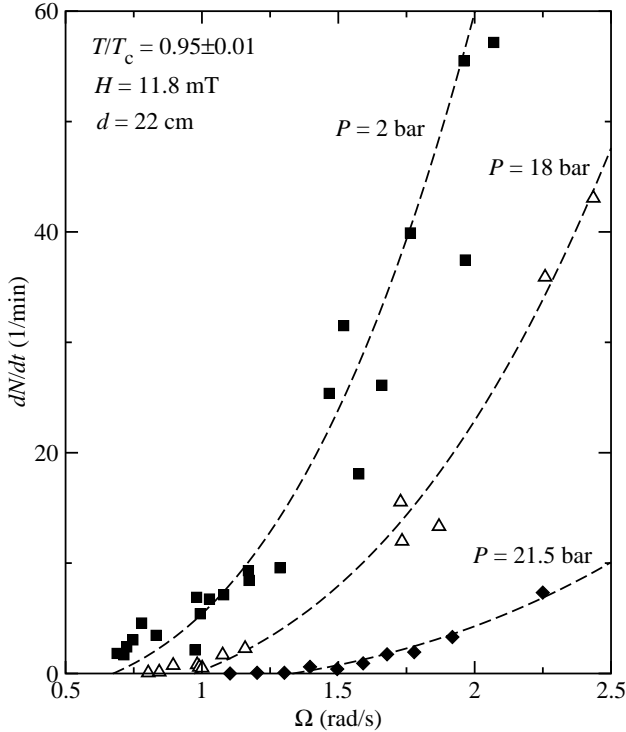


FIG. 10. Initial rate  $\dot{N}$  of vortex line formation at different rotation velocities  $\Omega$ .  $\dot{N}$  has been measured as the average of all vortex lines formed during an accumulation period of 15 – 30 min. The fitted curves are of the form  $\gamma [(\Omega/\Omega_{\text{cn}})^3 - 1]$  (Eq. (8)). Their low velocity end points determine the threshold velocity  $v_{\text{cn}} = \Omega_{\text{cn}} R$ .

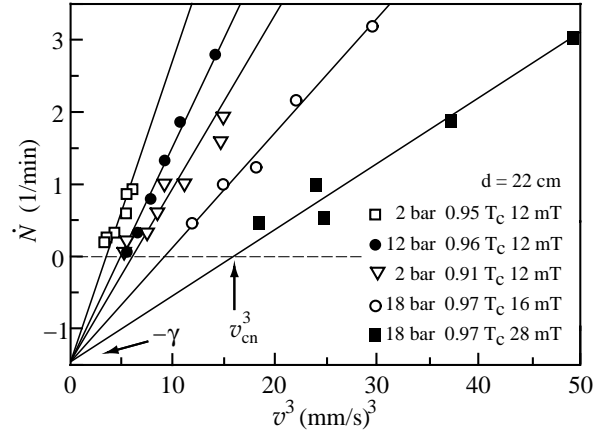


FIG. 11. Vortex-formation rate  $\dot{N}$  plotted versus the cube of the bias velocity  $v$ . This plot is used to determine the threshold velocity  $v_{\text{cn}}$ . A line has been fit to each set of data, measured under different external conditions, to identify the horizontal intercept  $v_{\text{cn}}^3$  and the common vertical intercept  $-\gamma = -1.4 \text{ min}^{-1}$ . (From Ruutu et al. 1996a).

tices form during such a run compared to the number of vortices in the equilibrium state. Thus the total decrease in the counterflow velocity is small and can be accounted for by assigning the average of the velocities before and after irradiation as the appropriate value of the applied bias velocity. An example of the measured rates is shown in Fig. 10.

These measurements reveal a vortex-formation rate  $\dot{N}$  as a function of  $v$  which has an onset at a threshold velocity  $v_{\text{cn}}$ , followed by a rapid non-linear increase. As shown in Fig. 3, close above the threshold a successful neutron absorption event produces one vortex line, but at high flow rates many lines may result. Therefore the nonlinear dependence  $\dot{N}(\Omega)$  arises in the following manner: Initially the fraction of successful absorption events increases, i.e. of those which produce one new vortex line. Eventually this effect is limited by the neutron flux, when essentially all absorbed neutrons produce at least one new vortex. The second part of the increase is brought about by the fact that more and more lines are produced, on an average, in each absorption event.

As demonstrated in Fig. 11 the dependence of the rate  $\dot{N}$  on the counterflow velocity  $v$  can be approximated by the empirical expression

$$\dot{N}(v) = \gamma \left[ \left( \frac{v}{v_{\text{cn}}} \right)^3 - 1 \right] \quad (8)$$

with  $\gamma$  and  $v_{\text{cn}}$  as parameters. This equation also describes the results in Fig. 9: If initially  $v$  in the vortex-free state is only slightly larger than the critical velocity  $v_{\text{cn}}$ , then Eq. (8) can be linearized to  $\dot{N} \approx 3\gamma(v/v_{\text{cn}} - 1)$ . Thus  $N(t)$  is obtained by integration from

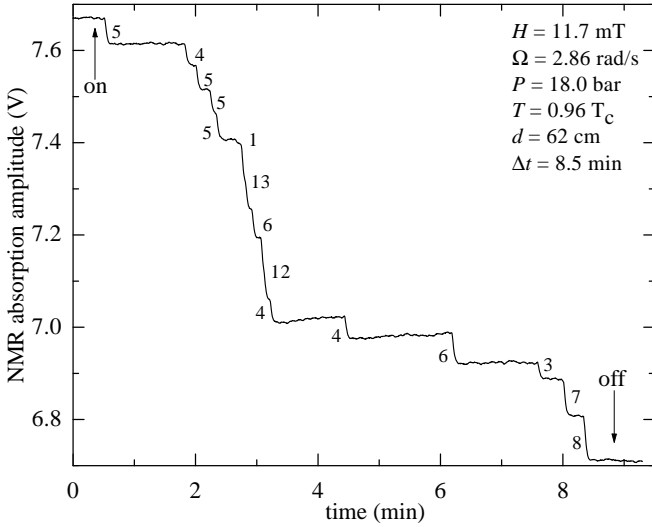


FIG. 12. Neutron irradiation and vortex-line yield at high rotation velocity. The total number of lines, which are created in one irradiation session, can be determined in several ways: 1) In this example the direct count of the steps in signal amplitude yields 88 lines (cf. Fig. 3). The number next to each step denotes its equivalent in rectilinear vortex lines. 2) From Fig. 7 one finds that the drop in signal amplitude per vortex line is 11 mV in the present measuring conditions. The total amplitude drop of 960 mV corresponds thus to 87 vortex lines. 3) A measurement of the annihilation threshold, by successive deceleration to lower and lower  $\Omega$  (Ruutu et al. 1997a), gives the total number of lines in the vortex cluster. Here this measurement yields  $\Omega_v = 0.245$  rad/s. The annihilation threshold, which at  $\Omega_v \gtrsim 0.2$  rad/s coincides with the equilibrium vortex state, corresponds to  $N = \pi R^2 2\Omega_v \kappa^{-1} (1 - 0.18\sqrt{1 \text{ rad s}^{-1}/\Omega_v})$ , as measured by Ruutu et al. (1998b). With  $R = 2.45$  mm, this gives 88 vortex lines. 4) The rate equation (8), with the measured values of  $\gamma$  and  $v_{\text{cn}}$  from Fig. 11, gives 88 lines for an irradiation time of 8.5 min (with  $\Omega_{\text{cn}} = 0.75$  rad/s). Thus all of the reduction in the height of the counterflow peak (cf. Fig. 6) can be reliably accounted for in many different ways.

$$\dot{N}(t) = 3\gamma \left( \frac{v(0) - \kappa N(t)/(2\pi R)}{v_{\text{cn}}} - 1 \right) \quad (9)$$

with the solution

$$N(t) = \frac{2\pi R}{\kappa} [v(0) - v_{\text{cn}}] \left[ 1 - \exp\left(-\frac{3\gamma\kappa t}{2\pi R v_{\text{cn}}}\right) \right]. \quad (10)$$

This equation has been fit to the measurements in Fig. 9, to give the two parameters  $\gamma$  and  $v_{\text{cn}}$ . The resulting values agree with those of the horizontal and vertical zero intercepts in Fig. 11.

At high rotation velocities a large number of vortex lines is produced in each neutron absorption event. The accumulation record for one neutron irradiation session (similar to the upper trace in Fig. 3) then consists of many large steps where, in the worst case, two absorption

events might even be overlapping. Nevertheless, the final total number of lines, which have been collected into the central cluster, can be determined in a few different ways and these give consistent answers. These tests have been described in Fig. 12. One of them includes the use of the rate equation (8) where the multiplier  $\gamma$  has the value from Fig. 11.

In fact, it can be guessed from Fig. 11 that Eq. (8) has wider applicability than is apparent from the present examples: The same equation holds universally under different externally applied conditions with all dependence on external variables contained in  $v_{\text{cn}}(T, P, H)$ , while  $\gamma$  is proportional to the neutron flux but does not depend on temperature, pressure, or magnetic field. Hence  $\dot{N}(v/v_{\text{cn}})$  appears to be a universal function for all measurements which have been performed in the temperature regime  $T > 0.8T_c$ .

To summarize, the experimental result displays two distinguishing features: 1) the cubic dependence on the bias  $v$  and 2) the universality that all dependence of the vortex formation properties on the experimental variables  $T$ ,  $P$ , and  $H$  is contained in the threshold velocity  $v_{\text{cn}}$ .

## 2.8. Volume or surface mechanism?

In the following sections we examine the various experimental properties of the neutron-induced vortex formation. The analysis demonstrates that most features are consistent with the KZ mechanism – none have so far been found contradictory. But does this fact constitute solid proof of the mechanism?

Neutron-induced vortex formation in a rotating superfluid does not exactly fit the ideal KZ model — a rapid second order transition in an infinite homogeneous system. In the heated neutron bubble there is a strong thermal gradient and a strict boundary condition applies at its exterior, imposed by the bulk superfluid state outside. The comparison of experiment and model is further complicated by the fact that the cool down occurs so fast that an extrapolation from the equilibrium state theories becomes uncertain, whether it concerns the hydrodynamics or even the superfluid state itself. (The applicability of the KZ mechanism to inhomogeneous transitions is considered in more detail in Sec. 2.15.) Perhaps, other processes of hydrodynamic origin can be suggested which account for the experimental observations?

The most viable alternative arises from the boundary condition in the presence of the applied bias flow: It is the instability of superflow along the normal-superfluid interface in the outer peripheral regions of the neutron bubble. In the Ginzburg-Landau temperature regime the container-dependent spontaneous critical velocity  $v_c(T, P)$  decreases with increasing temperature and vanishes at  $T_c$  (dashed curves in Fig. 13). It is related (via

surface roughness enhancement) to the intrinsic instability velocity  $v_{\text{cb}}(T, P)$  of the bulk superfluid (Parts et al. 1995; Ruutu et al. 1997a), which has qualitatively a similar temperature and pressure dependence, but is larger in magnitude. In the outermost region of the neutron bubble the fluid remains in the B phase, but is heated above the surrounding bulk temperature  $T_0$ . Consequently, if no other process intervenes, the superflow instability has to occur within a peripheral shell surrounding the hot neutron bubble where  $v_{\text{cb}}(T, P)$  drops below the applied bias  $v$ . This process was discussed by Ruutu et al. (1998a) and compared to rotating measurements, but was found incompatible with the measured results. As explanation it was suggested that the KZ mechanism is inherently the fastest process for creating vortices.

The interplay between the interior volume of the neutron bubble and its boundary was examined by Aranson et al. (1999) in a rapidly cooling model system with a scalar order parameter, using the thermal diffusion equation to account for cooling and the time-dependent Ginzburg-Landau equation for order-parameter relaxation. Rigorous analytic calculations showed that the normal-superfluid interface becomes unstable in the presence of superflow along the interface. Numerical calculations (Aranson et al. 1999, 2001) further confirmed that the instability develops such that vortex rings are formed. The rings encircle the bubble perpendicular to the applied flow and screen the superflow, so that the superfluid velocity (in the rotating frame) is zero inside the bubble. The number of rings depends on the shape and size of the bubble and on the bias velocity. In this process it does not matter what the state of the liquid is inside the bubble: The rings are formed within an external cooler layer, which remains throughout the process in the B phase. After their formation, the rings start to expand and might eventually be pulled away by the Magnus force. Thus these rings could be the source for the vortex lines which are observed in the rotating measurements.

However, the calculations also confirmed that in addition to the superflow instability at the bubble boundary, the KZ mechanism in the bubble interior is also present – thus in this calculation both processes produce vortices. In the simulation the loops, which eventually manage to escape into the bulk bias flow, originate from the boundary while the random vortex network in the interior collapses and decays away. Thus Aranson et al. confirmed the presence of the KZ mechanism, but concluded that the vortices observed in the rotating measurements are produced by the boundary instability. The time-dependent Ginzburg-Landau treatment with one common relaxation time for both the phase and the magnitude of the order parameter is rigorously obeyed only within a narrow temperature interval from  $T_c$  down to  $1 - T/T_c \sim 10^{-3}$ . The bulk liquid temperature in the rotating measurements is at least an order of magnitude be-

low this range (see Fig. 13). Another difference between experiment and calculation lies in the size of the neutron bubble: The numerical calculation is carried out on a grid with unit length smaller than the coherence length  $\xi(T_0)$ . To make this tractable, the reaction energy  $E_0$  is reduced by one or two orders of magnitude. This scales down the neutron bubble radius  $R_b$  via the thermal diffusion equation, which is used to model the neutron bubble (see Sec. 2.9.1). A smaller bubble (see Eq. (14)) means a faster velocity of the phase front ( $\propto 1/R_b$ ). At present time it is not known how reliably the calculation with its differences extrapolates into the range of the measurements.

How do we, in fact, distinguish from measurements whether it is the KZ mechanism or the boundary instability which is responsible for the observed vortex lines? Clearly the critical velocity  $v_{\text{cn}}$  does not discriminate between them. In both cases  $v_{\text{cn}}$  is the velocity of the bias flow at which the largest vortex ring which fits in the bubble is stable, as will be shown in Sec. 2.9. However, the different nature of the two processes has important consequences for the vortex formation rate  $\dot{N}(v)$ . The row of vortex rings, which is produced by the boundary instability to screen the interior of the neutron bubble from the bias flow, resembles a vortex sheet. The sheet is formed in the heated peripheral shell of the neutron bubble, where the outside superfluid moves with velocity  $v$  along the bubble interface and the superfluid inside is stationary. The density of vorticity in the sheet is  $v/\kappa$  and the number of loops produced by one neutron absorption event is  $N \propto vR_b/\kappa$ , where  $R_b$  is the size of the bubble along the flow direction. Thus  $N(v)$  grows linearly with the applied bias flow velocity,  $N(v) \propto v$ , which agrees with the result of Aranson et al. (1999). In contrast, the KZ mechanism is a volume effect, which results in the cubic dependence expressed in Eq. (8) (see also Sec. 2.12.2). The measured result in the figures of the previous section is not linear, but is consistent with the cubic dependence.

Are there other arguments emerging from the measurements which would support the KZ origin of the observed vortices? Several more can be listed in addition to the rate dependence  $\dot{N}(v)$ , which favor a volume effect: (i) The boundary instability is expected to be a deterministic process which in every neutron event produces the same surface density of vortex rings. Variations in the number of rings arise only owing to variations in the shape of the neutron bubble and its orientation with respect to the bias flow. (Unfortunately, the distribution of the number of rings was not studied in detail in the simulations by Aranson et al. 2001.) In contrast, the KZ mechanism produces a random vortex network from which the number of loops extracted by the bias flow varies and follows a stochastic distribution (Fig. 30). (ii) The boundary instability should not be particularly sen-



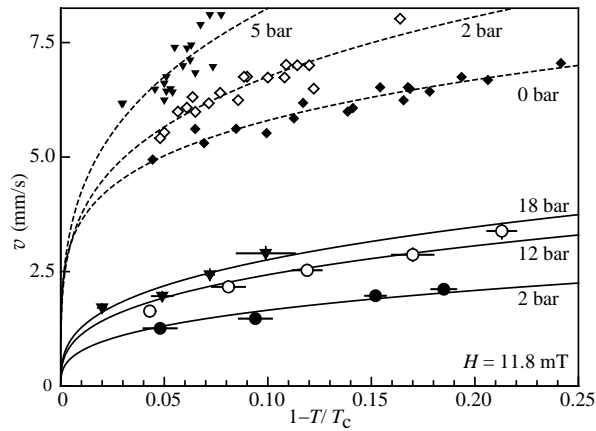


FIG. 13. Critical values of the applied bias velocity  $v$  vs. temperature at different pressures: (Solid lines) Threshold velocity  $v_{\text{cn}} \propto (1 - T/T_c)^{1/3}$  for vortex formation in neutron irradiation (Ruutu et al. 1996a). (Dashed lines) Critical velocity  $v_c \propto (1 - T/T_c)^{1/4}$  of spontaneous vortex formation in the same quartz glass container in the absence of the neutron source. (From Parts et al. 1995; Ruutu et al. 1997a).

sitive to the processes inside the heated neutron bubble and only regular mass-flow vortices are expected to form in such an instability. The KZ mechanism, on the other hand, can be expected to produce all possible defects. Their presence might be either directly observed in the final state or via their influence on the evolution of the vortex network inside the neutron bubble. Such observations are discussed in Sec. 2.10.

## 2.9. Threshold velocity for vortex loop escape

The dependence on the counterflow bias  $v$  can be studied from the threshold  $v_{\text{cn}}$  up to the critical limit  $v_c$  at which a vortex is spontaneously nucleated at the cylindrical wall in the absence of the neutron flux (Parts et al. 1995; Ruutu et al. 1997a). The threshold velocity  $v_{\text{cn}}(T, P, H)$  is one of the features which can be examined to learn more about neutron-induced vortex formation. Measurements of both critical velocities,  $v_{\text{cn}}$  and  $v_c$ , are shown in Fig. 13 as a function of temperature.

### 2.9.1. Properties of threshold velocity

By definition the threshold  $v_{\text{cn}}$  represents the smallest bias velocity at which a vortex ring can escape from the neutron bubble after the absorption event. It can be connected with the bubble size in the following manner. A vortex ring of radius  $r_o$  is in equilibrium in the applied bias flow at  $v$  if it satisfies the equation

$$r_o(v) = \frac{\kappa}{4\pi v} \ln \left( \frac{r_o}{\xi(T, P)} \right). \quad (11)$$

As explained in more detail in Sec. 2.12.2, a ring with a radius larger than  $r_o$  will expand in the flow while a smaller one will contract. Thus the threshold or minimum velocity at which a vortex ring can start to expand towards a rectilinear vortex line corresponds to the maximum possible vortex-ring size. This must be comparable to the diameter of the heated bubble. For a simple estimate we set the vortex ring radius equal to that of a spherical neutron bubble:  $r_o(v_{\text{cn}}) \sim R_b$ . (In fact, the numerical simulations to be described in Sec. 2.14.3 suggest that  $r_o(v_{\text{cn}}) \approx 2R_b$  because of the complex convoluted shape of the largest rings in the random vortex network.)

A simple thermal diffusion model can be used to yield an order of magnitude estimate for the radius  $R_b$  of the bubble which originally was heated above  $T_c$ . In the temperature range close to  $T_c$  the cooling occurs via diffusion of quasiparticle excitations out into the surrounding superfluid with a diffusion constant  $D \approx v_F l$ , where  $v_F$  is their Fermi velocity and  $l$  their mean free path. The difference from the surrounding bulk temperature  $T_0$  as a function of the radial distance  $r$  from the centre of the bubble can be calculated from the diffusion equation

$$\frac{\partial T(r, t)}{\partial t} = D \left( \frac{\partial^2 T}{\partial r^2} + \frac{2}{r} \frac{\partial T}{\partial r} \right). \quad (12)$$

With the assumption that at  $t = 0$  the reaction energy  $E_0$  is deposited at  $r = 0$ , the solution is given by

$$T(r, t) - T_0 \approx \frac{E_0}{C_v} \frac{1}{(4\pi Dt)^{3/2}} \exp\left(\frac{-r^2}{4Dt}\right), \quad (13)$$

where  $C_v$  is the specific heat. For now, we may assume that all the energy of the neutron absorption reaction is deposited as heat. The bubble of normal fluid,  $T(r) > T_c$ , first expands and reaches a maximum radius

$$R_b = \sqrt{\frac{3}{2\pi e}} \left( \frac{E_0}{C_v T_c} \right)^{1/3} (1 - T_0/T_c)^{-1/3}. \quad (14)$$

It then starts cooling and rapidly shrinks with the characteristic time  $\tau_Q \sim R_b^2/D \sim 1\mu\text{s}$ . Since  $v_{\text{cn}}$  is inversely proportional to  $r_o \sim R_b$ , it has the temperature dependence  $v_{\text{cn}} \propto (1 - T_0/T_c)^{1/3}$ . This is in agreement with the solid curves in Fig. 13 which have been fitted to measurements on  $v_{\text{cn}}$ . The prefactor of these curves is in agreement with that from Eqs. (14) and (11) within a factor of  $\sim 2$ , and its increase with increasing pressure is well described by the decrease in bubble size according to Eq. (14), where  $C_v$  and  $T_c$  increase with pressure (Greywall 1986).

### 2.9.2. Influence of $^3\text{He-A}$ on the threshold velocity $v_{\text{cn}}$

Measurements on the threshold velocity  $v_{\text{cn}}$  offer interesting possibilities to study whether the interior of the

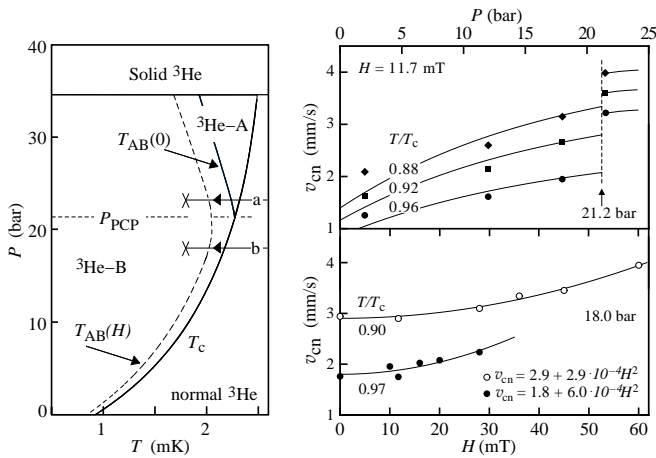


FIG. 14. Threshold velocity  $v_{\text{cn}}$  for the onset of vortex formation during neutron irradiation: (Left) Phase diagram of  $^3\text{He}$  superfluids in the pressure vs. temperature plane, with the A  $\rightarrow$  B transition at  $T_{\text{AB}}(0)$  in zero field (solid line) and at  $T_{\text{AB}}(H)$  in nonzero field (dashed line). Two quench trajectories, distinguishing different types of measurements on the right, are marked with (a) and (b). (Right top) The pressure dependence of  $v_{\text{cn}}$  displays a steep change at the pressure  $P_{\text{PCP}}$  of the polycritical point. (Right bottom) The magnetic field dependence of  $v_{\text{cn}}$  is parabolic, similar to that of the equilibrium state A  $\rightarrow$  B transition  $T_{\text{AB}}(H)$ . (From Ruutu et al. 1998a).

heated bubble participates in vortex formation or not. In the left panel of Fig. 14 the phase diagram of  $^3\text{He}$  is shown at temperatures below 2.5 mK. In the measurements which we discussed so far, the liquid pressure has been below 21.2 bar, so that the heated bubble cools from the normal phase directly into the B phase (along trajectory b). On the top right in Fig. 14 the measured  $v_{\text{cn}}$  is plotted as a function of pressure  $P$  at constant reduced temperature  $T/T_c$ . Here the pressure dependence displays an abrupt increase at about 21.2 bar, the pressure  $P_{\text{PCP}}$  of the polycritical point: It thus makes an unexpectedly large difference whether the quench trajectory follows a path denoted with a or with b! The two cooling trajectories differ in that above  $P_{\text{PCP}}$  a new phase,  $^3\text{He-A}$ , is a stable intermediate phase between the normal and B phases. Consequently, although the bulk liquid is well in the B phase in all of the measurements of Fig. 14, vortex formation is less than expected on the basis of extrapolations from lower pressures, when the quench trajectory crosses the stable A-phase regime.

The fitted curves in Fig. 14 represent  $v_{\text{cn}}(P)$  at pressures below  $P_{\text{PCP}}$

$$v_{\text{cn}} = \mathcal{A}\kappa/(4\pi R_b) \ln(R_b/\xi), \quad (15)$$

where  $R_b$  is obtained from Eq. (14). If we assume that all of the reaction energy is transformed to heat ( $E_0 = 764$  keV), then the common scaling factor  $\mathcal{A}$  of the three

curves has the value  $\mathcal{A} = 2.1$ . This is the only fitting parameter in Figs. 13 and 14 where the same fit is compared to measurements as a function of both temperature and pressure. The agreement is reasonable and suggests that the spherical thermal diffusion model is not too far off. However, as seen in Fig. 14,  $v_{\text{cn}}$  is clearly above the fit at  $P > P_{\text{PCP}}$ . Also this offset is largest at the highest temperature, which in Fig. 14 is  $0.96 T_c$ . Both features suggest that vortex formation is reduced when the relative range of A-phase stability increases over the quench trajectory below  $T_c$ .

The lower right panel of Fig. 14 shows the dependence of  $v_{\text{cn}}$  on the applied magnetic field  $H$ . Below  $P_{\text{PCP}}$  the magnetic field acts to stabilize  $^3\text{He-A}$  in a narrow interval from  $T_c$  down to the first order A  $\rightarrow$  B transition at  $T_{\text{AB}}(P, H)$ . This result confirms our previous conclusion:  $v_{\text{cn}}$  again increases when the range of A-phase stability increases. The parabolic magnetic field dependence of  $v_{\text{cn}}(H)$  in the lower right panel is reminiscent of that of the equilibrium  $T_{\text{AB}}(H)$  transition temperature.<sup>2</sup> It should be noted that the measurements in the upper right panel of Fig. 14 have not been carried out in zero magnetic field but in 11.7 mT. However, as shown in the lower panel, the field dependence in the range 0–12 mT is not visible within the experimental precision.

Thus by increasing the pressure above  $P_{\text{PCP}}$  or by increasing the magnetic field we reduce the A-phase energy minimum relative to that of the B phase and both operations act to increase  $v_{\text{cn}}$ . If we go back to Figs. 10 and 11, we note that both operations seem to leave the rate equation (8) and its rate constant  $\gamma$  unchanged. To be more careful, we conclude that in first order the changes from increased A-phase stability appear to affect only  $v_{\text{cn}}$ . This conclusion is compatible with the KZ model, as will be discussed in the next sections. What about the competing model, the superflow instability at the boundary of the heated neutron bubble, can it also account for the observations in Fig. 14? At first glance this does not appear to be the case.

The superflow instability occurs in B phase in the outer periphery of the heated bubble in a shell where the temperature is close to  $T_c$ . In principle this phenomenon should not be influenced by the appearance of A phase in the interior of the bubble during its cool down to the bath temperature  $T_0$ . However, it can be affected by the presence of an A phase shell around the hot bubble, bounded by an inner surface  $T = T_c$  and an outer  $T = T_{\text{AB}}$ , *i.e.* a region where the temperature exceeds the AB transition temperature  $T_{\text{AB}}(P, H)$ . The B-phase bulk critical velocities

<sup>2</sup>According to Tang et al. (1991), below  $P_{\text{PCP}}$  the equilibrium A  $\leftrightarrow$  B transition temperature is in first order of the form  $T_{\text{AB}}(P, H) = T_c(P)(1 - bH^2)$ , where  $b(P) \sim (0.5 - 10) \cdot 10^{-6} (\text{mT})^{-2}$ .

ity is approximately equal to the pair-breaking velocity and in the Ginzburg-Landau temperature regime it is of the form (Vollhardt et al. 1980; Kleinert 1980)

$$v_{\text{cb}}(T, P) \approx v_{\text{c0}}(P) \sqrt{1 - T/T_c},$$

where  $v_{\text{c0}}(P) = 1.61 (1 + F_1^s/3) k_B T_c / p_F$ . This velocity is a smooth function of pressure and cannot account for the steep rise of  $v_{\text{cn}}$  at  $P_{\text{PCP}}$  in Fig. 14 (upper right panel). The B-phase boundary instability occurs within an outer shell where the inner surface is defined by  $T = T_c$  and the outer by the condition  $v_{\text{cb}}(T, P) = v$ . For the data in Fig. 14 the latter condition puts the outer surface of this shell at  $1 - T/T_c \sim 10^{-3} - 10^{-5}$ , which falls inside the shell within which A-phase is stable. Thus here it is the A-phase shell within which the boundary instability has to occur. Such a situation is complicated (see Blaauwgeers et al. 2002; Parts et al. 1993) and possibly one where the escape of vorticity from the A-phase shell into B-phase is reduced. In first order these considerations suggest that  $v_{\text{cn}}$  increases with increasing pressure and magnetic field, when the range of the stable A-phase regime increases over the length of the quench trajectory as a function of temperature. However, it is unclear whether in a 3-phase problem — where an outer region of warm superfluid surrounds a hot interior with normal liquid, while both are embedded in a cold bath of B-phase — coherence is established such that we can apply shell structure considerations. Therefore, in the absence of more quantitative estimates, we must conclude that the measurements in Fig. 14 do not yet allow a preference between the KZ model or the superflow instability at the neutron bubble boundary. Clearly more extensive measurements are needed to study rapid thermal quenches in the 3-phase situation, as will be emphasized in Sec. 2.13.2.

## 2.10. Other defect structures formed in neutron irradiation

### 2.10.1. Radiation-induced supercooled A $\rightarrow$ B transition

The first order transition of supercooled  $^3\text{He-A}$  to  $^3\text{He-B}$  is another experimentally confirmed phenomenon which is catalyzed by the interior of the neutron bubble. Usual arguments about homogeneous first-order phase transitions show that the A $\rightarrow$ B transition is forbidden (Leggett 1984). The normal phase symmetry  $SO(3) \times SO(3) \times U(1)$  of liquid  $^3\text{He}$  can be broken to the  $U(1) \times U(1)$  symmetry of the A phase or to the  $SO(3)$  symmetry of the B-phase, with only a small energy difference between these two states, but separated by an extremely high energy barrier ( $\sim 10^6 k_B T_c$ ). Nevertheless, so far it has not been reported that the transition would not have taken place ultimately, if only one cools to sufficiently low temperature.

The A $\rightarrow$ B transition has not been found to be affected by rotation (Hakonen et al. 1985) and in the absence of ionizing radiation it is generally believed to be caused by extrinsic sources, perhaps at solid surfaces. A dramatic increase in the transition probability has been shown to take place in the bulk liquid in the presence of  $\gamma$  radiation or thermal neutrons (Schiffer et al. 1992; Schiffer and Osheroff 1995). A generally accepted understanding of this feature is still missing, because two quite different models, the “baked Alaska” (Leggett 1992; Schiffer et al. 1995; Leggett 2002) and the KZ mechanism (Volovik 1996; Bunkov and Timofeevskaya 1998a,b), are discussed in this context. Since only the latter is appropriate in radiation-induced vortex formation, we briefly describe it in the context of the supercooled A $\rightarrow$ B transition.

When  $^3\text{He-A}$  is supercooled to low temperatures, below the thermodynamic A $\leftrightarrow$ B transition, the sample stays in the A phase for long times, perhaps even indefinitely, depending on temperature and other largely unknown requirements. The deeper the supercooling, the faster the transition into the B phase follows. With increasing magnetic field the transition probability decreases, since a magnetic field acts to stabilize the A phase. However, when neutron irradiation is turned on, the transition probability increases sharply. In such measurements the initial state is supercooled  $^3\text{He-A}$  at varying temperatures and magnetic fields. Consequently here the A-phase state is enforced by the boundary condition around the hot neutron bubble: The boundary condition is not the source for the A $\rightarrow$ B transition! Rather the new B-phase state has to emerge from the interior of the bubble.

According to the KZ model, in different parts of the rapidly cooling neutron bubble the order parameter may fall initially either in the A or B phase energy minima. Thus a domain structure of size  $\xi_v$  (Eq. 3) is laid down, where A and B-phase blobs form a patch work. When these blobs later grow together, then AB interfaces are formed. The lower the temperature, the lower is the B-phase energy minimum relative to that of the A phase, the larger is the proportion of B-phase blobs in the patch work, and the more likely it is that many of them manage to merge together to form one large bubble, where the AB interface exceeds the critical diameter of about  $1 \mu\text{m}$ , needed for spontaneous A-phase expansion to start. This one seed is then sufficient to initiate the A $\rightarrow$ B transition in the whole sample.

The time dependent Ginzburg-Landau calculations of Bunkov and Timofeevskaya (1998a,b) are consistent with this model. In the calculations there is no spatial dependence, an initial fluctuation is imposed at  $T_c$  into a random direction of the phase space, and the evolution towards the final state is followed. As seen in Fig. 15, the energy difference between the A and B phases is small, but pressure dependent. During rapid cool down through

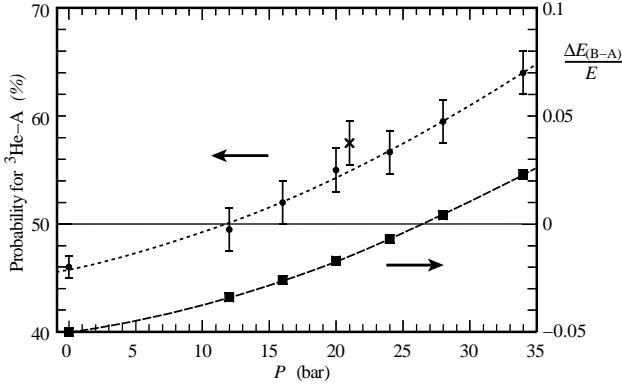


FIG. 15. Normalized energy difference,  $\Delta E_{(B-A)}/E(P)$ , between A and B phases (*right vertical axis*) and probability of A-phase formation in a rapid cool-down (*left vertical axis*), plotted as a function of pressure at temperatures close to  $T_c$  in the Ginzburg-Landau regime. The results have been calculated with the weak coupling  $\beta$  parameters ( $\beta_i = -1, 2, 2, 2, -2$ ), except for the data point marked with a cross ( $\times$ ) on the upper curve, for which strong-coupling parameter values have been used according to the spin fluctuation model. (From Bunkov and Timofeevskaya 1998a,b).

$T_c$  the order parameter may settle into either of these two energy minima with a pressure-dependent probability, which is also shown in Fig. 15.

Thus the KZ mechanism provides a simple explanation of the A $\rightarrow$ B transition probability as a function temperature and magnetic field in supercooled  $^3\text{He-A}$ . This model is independent of the boundary condition, which dictates  $^3\text{He-A}$ . Furthermore, in ambient conditions, where only B phase is stable, A-phase blobs ultimately shrink away and only B phase remains. Before that, however, a network of AB interfaces is created which interact with the formation of other topological defects. This feature can be used to explain the sharp increase in  $v_{\text{cn}}$  at  $P_{\text{PCP}}$  in Fig. 14 (top right panel).

### 2.10.2. Vortex formation, AB interfaces, and KZ mechanism

The KZ model predicts that in different parts of the cooling neutron bubble the order parameter may fall initially either in A or B phase energy minima, and a patchwork of AB interfaces is laid down. The relative number of A and B-phase blobs of size  $\xi_v$  is not only determined by the difference in the A and B-phase energies: It also depends on the trajectory from the normal phase to the new energy minimum in the phase space spanned by the order parameter components. The latter aspect gives more preference to the higher energy A state: Although the A-phase is energetically not favorable in a wide pressure range, the probability of its formation has

a value close to 50 % even at lower pressures, as shown in Fig. 15. The AB interfaces interfere with the simultaneous formation of a random vortex network, which is laid down separately in both the A and B phases. It is known from experiments on both a moving AB interface (Krusius et al. 1994) and a stationary AB interface (Blaauwgeers et al. 2002) that the penetration of vortex lines through the AB phase boundary is suppressed. We thus expect that the presence of A-phase blobs reduces the combined volume which remains available for B phase blobs and their vortex network inside a neutron bubble. Consequently, when B-phase blobs merge to larger units, the overall volume, into which the B-phase vortex network is confined, is smaller, and B-phase vortex formation becomes impeded. This process increases the value of  $v_{\text{cn}}$ .

To conclude, the KZ mechanism provides a unified view on the problems of pressure and magnetic field dependences of  $v_{\text{cn}}$  (Fig. 14) and also the A $\rightarrow$ B transition in supercooled  $^3\text{He-A}$ . In both cases AB interfaces appear as a new type of defect in the rapidly cooling neutron bubble. Normally, to create a sizeable bubble of B phase within bulk A liquid requires that an AB interface of large size is formed. This is a slow and energy consuming process. In quench cooling through  $T_c$  the freeze-out of disconnected blobs with A and B-phase like fluctuations happens first and these are initially separated by supercooled normal liquid. The AB interfaces appear later as metastable defects when the blobs grow together. Such an interpretation suggests that the KZ mechanism is the fastest process by which defects are created, before other effects manage to switch on.

### 2.10.3. Spin-mass vortex

Unlike vortex lines, which are produced in neutron irradiation and are then partly stabilized by the applied flow, no bias is provided for maintaining AB interfaces in Fig. 14. Thus in these rotating experiments, the evidence for AB interfaces remains indirect. However, there exists another topologically stable defect, which is formed in a neutron absorption event and is preserved by the bias flow for later examination. This is a combined object called the spin-mass vortex (Kondo et al. 1992; Korhonen et al. 1993).

The signature from the spin-mass vortex is explained in Fig. 16, where the counterflow peak height is plotted as a function of time during neutron irradiation (as in Figs. 3 and 12). This accumulation record shows one oversize step in the absorption amplitude, which coincides with a similar discontinuous jump in the out-of-phase dispersion signal. As explained in the context of Fig. 12, the total number of vortex lines extracted from an irradiation session can be determined in several different ways. In the

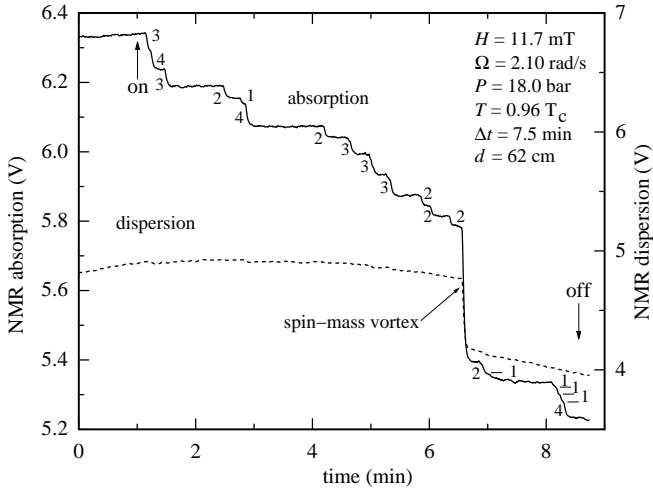


FIG. 16. Signal from spin-mass vortex in neutron irradiation. This irradiation session includes one large jump in signal amplitude. Like in Fig. 12, the various methods for extracting the total number of lines give: 1) A direct count of the steps in signal amplitude yields 45 lines plus the large jump. The combined amplitude drop for these 45 lines amounts to 716 mV which translates to 16 mV/vortex, in agreement with Fig. 7. With this step size the large jump of 390 mV would correspond to 25 additional lines. 2) A measurement of the annihilation threshold gives  $\Omega_v = 0.155$  rad/s, which corresponds to 48 lines. 3) The rate Eq. (8) gives  $\dot{N} = 6.2$  lines/min or a total of 48 lines for an irradiation of 7.5 min duration with the measured threshold value of  $\Omega_{cn} = 0.75$  rad/s. For these three estimates to be consistent, the large jump cannot be 25 lines. Instead it is interpreted to represent one spin-mass vortex line. In this case the size of the jump is not related to the number of lines, but to the counterflow velocity  $v(R)$  (Eq. (7)). It controls the length  $v(R)/2\Omega$  of the soliton sheet (Fig. 18). The dispersion signal also displays a simultaneous large jump, while it behaves smoothly when usual mass-current vortex lines are formed. Outside the discontinuity the dispersion signal is slowly drifting, because it is very sensitive to a residual temperature creep. (From Eltsov et al. 2000).

case of Fig. 16 a comparison of the different line counts shows that, within the uncertainty limits, the large jump cannot represent more than a few vortex lines. As will be seen below, this is the signature from a spin-mass vortex, which in Fig. 16 should be counted as one line.

The identification of the spin-mass vortex is based on its peculiar NMR spectrum (Kopu and Krusius 2001). In an axially oriented magnetic field the NMR spectrum has a textural cut off frequency, beyond which no absorption is allowed (excepting line broadening effects). The distinguishing feature of the spin-mass vortex is the absorption which has been pushed to the maximum possible frequency shift, beyond that of the counterflow (CF) peak (which corresponds to 80% of the maximum value, see Fig. 17).

Because of this shifted absorption, the CF peak is slightly shifted both in frequency and in height in the presence of a spin-mass vortex, compared to its location without the spin-mass vortex. This difference is displayed in Fig. 17, where the spectrum plotted with the solid curve includes one spin-mass vortex while the dashed spectrum is without it. The small frequency shift between these two peaks is the reason why also the NMR dispersion signal is discontinuous when the spin-mass vortex is formed during the neutron irradiation in Fig. 16. Since both the NMR absorption and dispersion signals are continuously monitored at the lock-in-amplifier output, a jump in the dispersion channel provides the immediate alert for a spin-mass vortex. In contrast, no discontinuity in the dispersion signal is observed in first order when a small number of vortex lines is added to the cluster at high bias velocity (see spectra in Fig. 6). In this case some absorption intensity is shifted towards the Larmor edge to small frequency shifts, and the change in the dispersion signal at the site of the CF maximum is negligible.

The large-scale configuration, in which the spin-mass vortex appears, is shown in the top part of Fig. 18. It consists of a linear object and a planar domain-wall-like soliton sheet. The line defect provides one termination for the sheet while its second end is anchored on the cylindrical wall of the container. The line defect consists of a singular core, which supports a circulating superfluid mass current, but has additionally trapped a disclination line in spin-orbit coupling. The latter feature can also be described in terms of a spin vortex which supports a persistent spin current. Thus the composite object, the spin-mass vortex, has the combined properties of a usual mass-current vortex and a spin-current vortex. A gain in the core energy of the combined structure provides the energy barrier against their dissociation. The soliton sheet is the continuation into the bulk superfluid from the breaking of the spin-orbit coupling: It separates two degenerate domains with anti-parallel orientations of the B-phase anisotropy axis  $\hat{n}$  (lower part of Fig. 18). The spin-mass vortex feels the Magnus force from the applied bias flow, but this is partly compensated by the surface tension of the soliton sheet. The equilibrium position of the spin-mass vortex is therefore at the edge of the vortex cluster (top part of Fig. 18) from where it can be selectively removed by annihilation, as was done in the experiment of Fig. 17.

The origin of the two defects in the spin-mass vortex can be seen from the form which the B-phase order parameter takes (Vollhardt and Wölfle 1990):

$$A_{\alpha j} = \Delta_B(T, P) e^{i\phi} R_{\alpha j}(\hat{n}, \theta). \quad (16)$$

It includes the isotropic energy gap  $\Delta_B(T, P)$ , the phase factor  $e^{i\phi}$ , and the rotation matrix  $R_{\alpha j}(\hat{n}, \theta)$ . The latter defines the rotation by which the  $SO(3)_L$  orbital

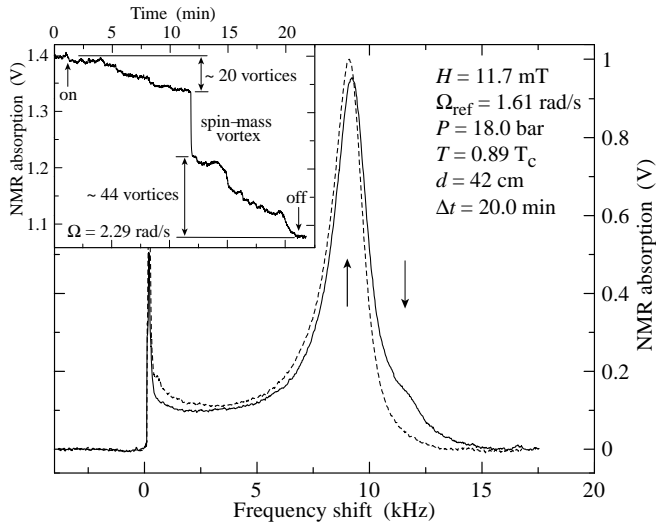


FIG. 17. NMR signal characteristics of the spin-mass vortex. (*Insert*) This 20 min irradiation session includes one large jump, in addition to vortex-line formation. The latter amounts to 64 lines, as determined from the measured annihilation threshold  $\Omega_v = 0.19$  rad/s. The rate Eq. (8) gives  $\dot{N} = 3.35$  lines/min or a total of 67 lines (with the measured  $\Omega_{cn} = 1.10$  rad/s). The combined drop in signal amplitude from these lines is 206 mV, which corresponds to 3.2 mV/line. Here at a lower temperature the step size per vortex is much reduced from that in Fig. 12. The single large jump corresponds to 36 additional lines, but like in Fig. 16 it is interpreted to represent one spin-mass vortex. (*Main panel*) NMR spectra of the accumulated vortex sample, recorded at a lower reference velocity  $\Omega_{ref}$ : The solid curve with the smaller counterflow peak is the original state after irradiation and deceleration from 2.29 to 1.61 rad/s. The dashed curve with the higher counterflow peak was traced later after cycling  $\Omega$  from 1.61 to 0.20 rad/s and back, i.e. after decelerating close to, but still above the annihilation threshold of the regular vortex cluster. In the former spectrum (solid curve) the soliton sheet shifts a sizeable fraction of the absorption to the maximum possible frequency shift (at right vertical arrow). After cycling  $\Omega$  the outermost spin-mass vortex (see Fig. 18 top panel) is annihilated (dashed curve) and the CF peak is shifted to the value (at left vertical arrow) without the soliton sheet. This shift in the frequency of the counterflow peak creates the jump in the dispersion signal in Fig. 16. Since the remaining regular cluster was not decelerated at any stage below its annihilation threshold of 0.19 rad/s, no usual vortex lines were annihilated from the dashed-curve spectrum.

and  $SO(3)_S$  spin spaces are rotated with respect to each other around the axis  $\hat{\mathbf{n}}$  by the angle  $\theta$ . To minimize the weak spin-orbit interaction, it is required that  $\theta = \arccos(-\frac{1}{4}) \approx 104^\circ$  homogeneously everywhere within the bulk superfluid. The mass-current vortex is associated with a  $2\pi$  circulation in the phase factor while the spin current involves a disclination line in  $R_{\alpha j}(\hat{\mathbf{n}}, \theta)$  field. The minimum energy configuration becomes then the structure depicted in the lower part of Fig. 18. Here

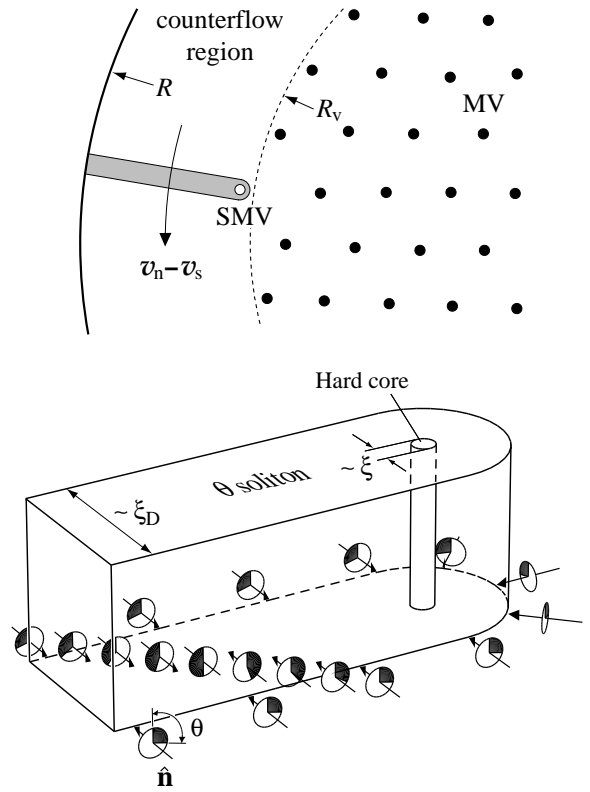


FIG. 18. (*Top*) The spin-mass vortex (SMV) is a composite object, which carries a trapped spin current as well as a mass current. In the rotating container it is confined by the Magnus force to the edge of the vortex cluster, which also includes usual mass-current vortex lines (MV). The extension of the spin vortex into the bulk liquid is a soliton tail (grey strip). The spin-mass vortex itself provides one termination line of the soliton while its second end is anchored on the cylindrical wall. (*Bottom*) Inside the soliton the angle  $\theta$  changes through  $\pi$  while outside it is homogeneously at  $104^\circ$ . At the soliton surface the rotation axis  $\hat{\mathbf{n}}$  is oriented perpendicular to the surface while further away it goes smoothly over into the flare-out texture of an ideal cylinder in an axially oriented magnetic field. The distortion of the  $\hat{\mathbf{n}}$  texture from the flare-out configuration in the region around the soliton (Kopu and Krusius 2001) gives rise to the NMR signature of the spin-mass vortex in Fig. 17.

the volume in the bulk, where the spin-orbit interaction is not minimized and  $\theta$  traverses through  $\pi$ , is concentrated within a soliton tail.

In  $^3\text{He-B}$  weak anisotropy energies arise in an external magnetic field. They produce an extended orientational distribution, or texture, of the anisotropy axis  $\hat{\mathbf{n}}$ . The characteristic length scale of this texture in the conditions of the rotating NMR measurements is  $\xi_H \propto 1/H \sim 1$  mm. Since the NMR frequency is controlled locally by the orientation of  $\hat{\mathbf{n}}$  with respect to  $\mathbf{H}$ , the NMR spectrum is an image of the  $\hat{\mathbf{n}}$  texture in the cylindrical container. In an axially oriented magnetic field and an infinitely long cylinder, the texture is known

to be of the “flare-out” form (Vollhardt and Wölfle 1990). In this texture there are no regions where  $\hat{\mathbf{n}}$  would lie in the transverse plane perpendicular to the field  $\mathbf{H}$ . In contrast, at the soliton sheet  $\hat{\mathbf{n}}$  is oriented strictly perpendicular to the sheet and thus to  $\mathbf{H}$ . This part of the texture is responsible for shifting NMR absorption into the region of maximum possible frequency shift and becomes thus the signature of the spin-mass vortex in the NMR spectrum (Fig. 17).

The presence of the soliton sheet has many important experimental implications: It determines the location of the spin-mass vortex at the edge of the cluster and it leaves a clear signature in the NMR spectrum at high bias velocities when the sheet becomes stretched. It also affects the threshold velocity at which a spin-mass vortex might be expected to escape from the neutron bubble. This was only observed to happen well above  $v_{\text{cn}}$ , the threshold velocity for usual mass-vortex rings (Fig. 13). It is explained by the fact that for spontaneous expansion a spin-mass vortex loop has to exceed, in addition to the usual barrier formed by the line tension of the small loop, also the surface tension from the soliton sheet.

The spin-mass vortex was originally discovered as a defect which is formed when an A  $\rightarrow$  B transition front moves slowly close to adiabatic conditions through a rotating container (Kondo et al. 1992; Korhonen et al. 1993). In this experiment the initial A-phase state is one with the equilibrium number of doubly quantized singularity-free vortex lines while the final state is found to contain less than the equilibrium number of singly quantized B-phase vortex lines plus some number of spin-mass vortices. This means that A-phase vortex lines interact with the moving AB interface, they are not easily converted to B-phase vorticity, a critical value of bias flow velocity has to be exceeded before the conversion becomes possible, and even then some fraction of the conversion leads to vorticity with the additional defect in  $R_{\alpha j}(\hat{\mathbf{n}}, \theta)$  (Parts et al. 1993; Krusius et al. 1994). In neutron measurements the spin-mass vortex was not observed at 2.0 bar, but at 18.0 bar. In the KZ scenario this is the pressure regime where the probability for the formation of A phase blobs in the neutron bubble increases (Fig. 15). Interestingly one might therefore surmise that even in the neutron bubble the spin-mass vortex could result from vorticity which originally was contained within A-phase blobs and which is partly transferred to the B phase when the A phase blobs shrink away.

The two NMR spectra in Fig. 17 illustrate the easy identification of the spin-mass vortex after neutron irradiation. Although the spin-mass vortex is a rare event in neutron irradiation, compared to the yield of vortex lines, its presence demonstrates that in addition to usual mass-current vortices also other order-parameter defects are created. This lends support to the discussion in Sec. 2.9.2 that also the AB interface could be among such defects.

The presence of the spin-mass vortex also limits the possible mechanisms of defect formation. An explanation in terms of the superflow instability at the neutron bubble boundary (Sec. 2.8) is not a probable alternative: The spin-mass vortex is not normally created at the bulk critical velocity limit  $v_{\text{cb}}(T, P)$  as a response to superflow.

## 2.11. Vortex formation in gamma radiation

To study the dependence of the vortex formation rate  $\dot{N}$  on the dimensions of the heated neutron bubble in the  $^3\text{He}$ -B bath, it would be useful to investigate alternative heating methods. In addition to thermal neutrons, beta and gamma radiation have frequently been used as a source of heat. In the rotating experiments a  $^{60}\text{Co}$  gamma source was experimented with, which emits  $\gamma$  rays at 1.17 and 1.33 MeV energy.

A gamma ray, which scatters in the container wall or in the liquid  $^3\text{He}$  bath, knocks off a secondary electron which gives rise to a heat release in the liquid  $^3\text{He}$  bath. The interaction probability is roughly proportional to the density of the material and thus a large fraction of the secondary electrons originate from the quartz glass wall. Although the initial energies of the secondary electrons cover a broad spectrum, the variation in the effective heat release is narrower. Energetic electrons knock off additional electrons which produce their own ionization tracks. However, once the energy has dropped in the regime of several keV, the remaining ionization track is short: roughly the rate of energy loss per unit distance travelled increases inversely proportional to the electron’s decreasing energy. Therefore the heating becomes concentrated within a distance  $\lesssim 10 \mu\text{m}$  of the final stopping point.

As a source for localized heating in liquid  $^3\text{He}$  experiments, gamma rays suffer from several shortcomings, compared to thermal neutrons: 1) It is not possible to concentrate on single heat-release events, since many secondary electrons can be produced by a single  $\gamma$  ray. Thus there is more variation in these events. For instance, the endpoints of different ionization tracks may fall close to each other and may merge to produce a large hot bubble of variable size. 2) The events are not localized in a well-determined location within the container. 3) It is not only the liquid  $^3\text{He}$  bath which preferentially absorbs the heat, but even more so the structural materials of the refrigerator. This interferes with the temperature control of the measurements: The heating produced by the  $\gamma$  radiation in the metal parts of the cryogenic equipment may rise to excessive levels, and radiation shielding and collimation need to be built into the experiment.

It was found that qualitatively vortex formation in gamma and neutron radiation are similar. But the measurements also showed that quantitative differences are



large: The threshold velocity  $v_{\text{cn}}$  is substantially increased and thus the yield  $\dot{N}(\Omega)$  at a given rotation velocity  $\Omega$  in the vortex-free state is smaller. So far no careful quantitative measurements have been carried out with  $\gamma$  radiation.

## 2.12. Bias dependence of loop extraction

The dependence of the vortex formation rate  $\dot{N}$  on the externally applied bias  $v$  is the most tangible quantitative result from the rotating measurements. It will be described and analyzed below (Ruutu et al. 1998a). The empirical rate equation (8) is shown to be consistent with the KZ model, including the measured value of the prefactor  $\gamma$ .

### 2.12.1. Experimental velocity dependence

The frequency and number of vortex lines can be counted from the accumulation record (Figs. 3, 12), when the NMR absorption is monitored as a function of time during neutron irradiation. Fig. 19 shows the vortex formation rate  $\dot{N}$  (a), the rate of those neutron absorption events  $\dot{N}_e$  which produce at least one line and thus become observable (b), and the average number of lines produced by each absorption event (c). All three quantities are determined independently and directly from the absorption records. In Fig. 19 the results are plotted as a function of the normalized bias  $v/v_{\text{cn}}$ . To construct the plot, the horizontal axis was divided into equal bins from which all individual measurements were averaged to yield the evenly distributed data points displayed in the graphs.

The rates in Fig. 19a,b are proportional to the intensity of the neutron flux, which is contained in the prefactors of the expressions given in the different panels of the figure. For counting the rates from the NMR absorption records it is vital that absorption events do not overlap, when the applied counterflow velocity is increased. Therefore three different source positions were used which were scaled to the same distance using the measured graph in Fig. 8.

The rates in Fig. 19 increase rapidly with the applied bias velocity  $v$ : At  $v/v_{\text{cn}} \approx 4.5$ , close to the maximum velocity limit imposed by the spontaneous instability limit (Fig. 13), there are almost no unsuccessful (or unobserved) absorption events left:  $\dot{N}_e(\infty) \approx \dot{N}_e(4.5 v_{\text{cn}})$ . The panel in the middle shows that this saturation corresponds to a flux of 20 neutrons/min. The same flux of neutrons was estimated to be absorbed in the sample based on independent measurements with commercial  $^3\text{He}$  counters. Also we note that in agreement with the scaling properties expressed by the rate equation (8), measurements at the two pressures of 2 and 18 bar fall on the same universal curves.

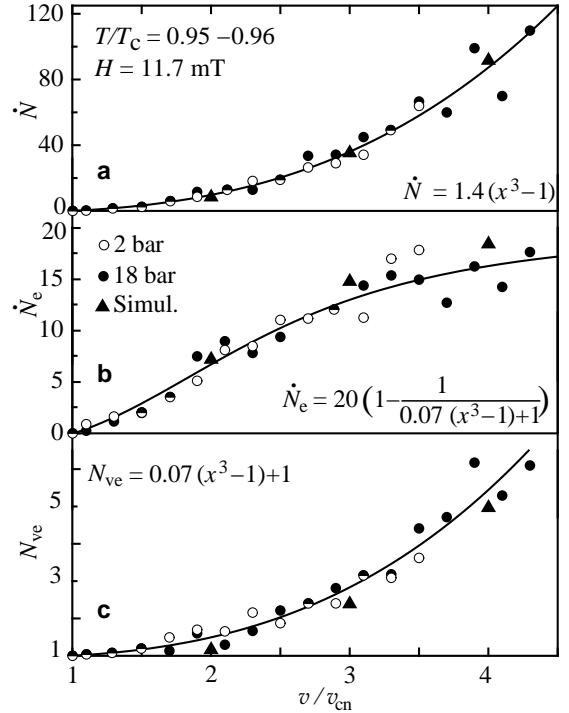


FIG. 19. Rates of vortex line formation plotted *vs* normalized bias velocity  $x = v/v_{\text{cn}}$ : (a) total number of lines formed per minute ( $\dot{N}$ ), (b) number of observed neutron absorption events per minute ( $\dot{N}_e$ ), and (c) average number of lines per observed event ( $N_{\text{ve}}$ ). All three quantities have been determined *independently* from discontinuities in NMR absorption, i.e. each data point is based on one or several accumulation plots like those in Fig. 3. The data in the two upper plots are proportional to the neutron flux, while the data in the bottom plot are neutron-flux independent. Solid curves are fits to the data, given by the expressions in each panel. Triangles are results from numerical simulations described in Sec. 2.14. (From Ruutu et al. 1998a).

Fig. 19 demonstrates that the neutron-induced vortex formation process involves a strong stochastic element: Close to the critical threshold at  $v = 1.1v_{\text{cn}}$  only one neutron capture event from 40 manages to produce a sufficiently large vortex loop for spontaneous expansion. On increasing the bias flow by a factor of four, almost all neutron capture events give rise to at least one escaping vortex loop. Secondly, the nonlinear increase of  $\dot{N}$  as a function of  $v/v_{\text{cn}}$  in the top panel has to be attributed to two factors: (i) the increase in the event rate  $\dot{N}_e$  in the middle panel and (ii) the rapid rise in the number of lines produced per event in the bottom panel. These conclusions fit with the KZ predictions, as we shall see in the next section.

The most detailed information from the rate measurements is the dispersion into events in which a given number of lines is formed. Fig. 20 displays the rates  $\dot{N}_{ei}$  of events which produce  $i = 1-5$  lines. This data ex-



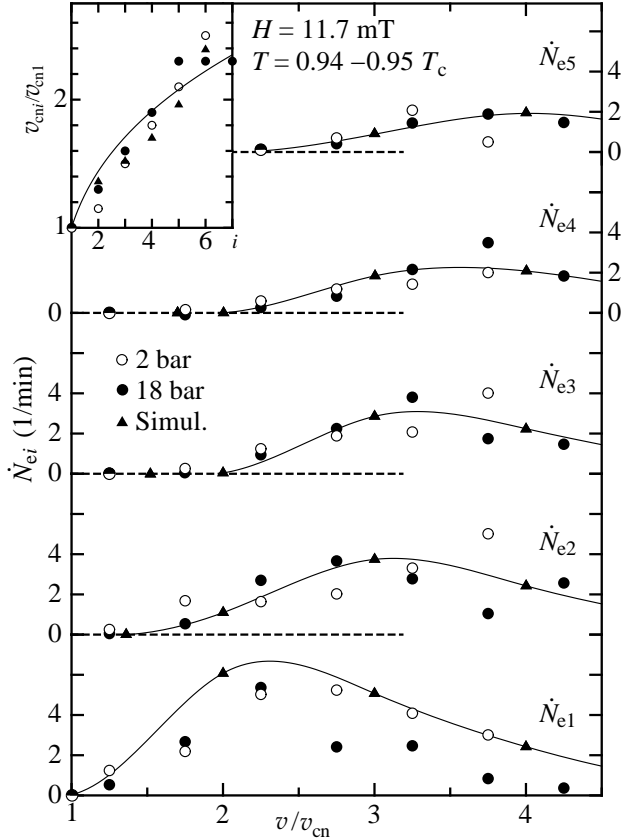


FIG. 20. Rates  $\dot{N}_{ei}$  of vortex formation events, grouped according to the number of lines  $i$  formed per absorption event, plotted vs  $v/v_{cn}$ . Triangles are result of numerical simulations described in Sec. 2.14. Solid curves are spline fits to simulation data. (*Inset*) Threshold velocity  $v_{cni}/v_{cn1}$  for the onset of an event with  $i$  lines, plotted vs the number of lines  $i$ . The solid curve represents the fit  $v_{cni}/v_{cn1} = [2.0(i-1) + 1]^{1/2}$ . (From Ruutu et al. 1998a).

hibits larger scatter, owing to its statistical variation, but again after averaging one gets for each value of  $i$  a curve, which peaks at a maximum, and then trails off. With increasing value of  $i$  the curves shift to successively higher velocities. The starting points of each curve, the threshold velocities  $v_{cni}$ , are plotted in the inset. Their values increase monotonically with each consecutive value of  $i$ . This means that at and immediately above the first threshold,  $v_{cn} = v_{cn1}$ , only single-vortex events occur.

A surprising finding from the measurements is the total absence of a background contribution to the measured rates. A number of tests were performed to look for spontaneous events in the absence of the neutron source, to check whether a contribution from the background radiation level should be subtracted from the measured rates. For instance, a vortex-free sample was rotated for 90 min at different velocities (0.9, 1.3, and 2.1 rad/s at 2.0 bar and  $0.94 T_c$ ), but not a single event was noted.

### 2.12.2. Analytic model of vortex loop escape

An analytic calculation can be constructed for independent vortex loops in the applied flow, which explains the cubic velocity dependence of the escape rate in Fig. 19. Vortex rings, which are part of the random vortex network after the quench, have a critical radius (Eq. (11)) below which they contract and above which they expand spontaneously in homogeneous superflow. By comparing this radius to the typical curvature in the random network, we arrive at the desired result (Ruutu et al. 1996a).

During the quench through the superfluid transition a random vortex network is formed with a characteristic length scale of the order of  $\xi_v$ . The later evolution of the network leads to a gradual increase in this length. The average inter-vortex distance or, equivalently, the typical radius of curvature of the loops increases with time. We shall call this length  $\tilde{\xi}(t)$ . This ‘‘coarse-graining’’ process preserves the random character of the network, in other words the network remains self similar or scale invariant. Only later a change occurs in this respect, when the loops become sufficiently large to interact with the externally applied bias flow: This causes large loops to expand, if they are oriented transverse to the flow with the correct winding direction, while small loops contract, and loops with the wrong sign of circulation tend to both contract and to change orientation. The time scale of these processes is determined by the magnitude of mutual friction between the normal and superfluid components. In the Ginzburg-Landau temperature range the evolution of the network occurs in milliseconds and the expansion of the extracted loops into rectilinear lines in a fraction of a second.

In superfluid  $^3\text{He}$  the large viscosity of the normal component clamps it to corotation with the container. In the rotating frame of reference we may write  $v_n = 0$  and  $v_s = v$ . The energy of a vortex loop, which is stationary with respect to the walls, is given by (Donnelly 1991)

$$\mathcal{E} = E_{\text{kin}} + \mathbf{p}\mathbf{v}, \quad (17)$$

where  $\mathbf{v}$  is the velocity of the applied superflow. In simple configurations, the hydrodynamic kinetic energy or self-energy of the loop arises from the trapped superfluid circulation with the velocity  $\mathbf{v}_{s,\text{vort}} = (\kappa/2\pi)\nabla\Phi$ ,

$$E_{\text{kin}} = \frac{1}{2} \int \rho_s v_{s,\text{vort}}^2 dV = \varepsilon L, \quad (18)$$

and is proportional to the length  $L$  of the loop and its line tension,

$$\varepsilon = \frac{\rho_s \kappa^2}{4\pi} \ln \frac{\tilde{\xi}(t)}{\xi}. \quad (19)$$

Here we neglect the small contribution from the core energy, use intervortex spacing  $\tilde{\xi}(t)$  as the upper cutoff, and

the superfluid coherence length  $\xi(T, P)$  as the lower cutoff for the integration in Eq. (18). This equation is valid in the logarithmic approximation, when  $\tilde{\xi}(t) \gg \xi(T, P)$ . While the first term in Eq. (17) is proportional to the length  $L$  of the loop, the second term involves its linear momentum,

$$\mathbf{p} = \int \rho_s \mathbf{v}_{s, \text{vort}} dV = \frac{1}{2\pi} \rho_s \kappa \int \nabla \Phi dV = \rho_s \kappa \mathbf{S} \quad , \quad (20)$$

where the last step follows from Gauss's theorem and involves the area  $S$  of the loop in the direction of the normal  $\mathbf{S}/S$  to the plane of the loop. Thus we write for the energy of a loop

$$\mathcal{E}(L, S, t) = \rho_s \kappa \left[ L \frac{\kappa}{4\pi} \ln \frac{\tilde{\xi}(t)}{\xi} - vS \right] \quad , \quad (21)$$

where  $S$  is the algebraic area, perpendicular to the flow and of proper winding direction. This equation expresses the balance between a contracting loop due to its own line tension, which dominates at small applied velocities, and expansion by the Magnus force from the external superflow, which dominates at high applied velocities. The divide is the equilibrium condition, which was expressed in Eq. (11) and corresponds to the situation when the height of the energy barrier, which resists loop expansion, vanishes. In this extremal configuration  $\mathbf{p}$  is antiparallel to  $\mathbf{v}$ , the loop moves with the velocity  $-\mathbf{v}$  in a frame of the superfluid component, but is stationary in the rotating frame. In a more general sense, if we consider loops in the random network which still deviate from circular shape, the extremal case degenerates to a saddle point. This is because the extremum requires also minimization with respect to deviations from circular shape, ie. the total energy is invariant under small variations of the radius of the ring, or  $\delta\mathcal{E} = \delta E_{\text{kin}} + \mathbf{v} \cdot \delta\mathbf{p} = 0$ .

The expansion of the vortex loop should be calculated by including the mutual friction forces. In our analytic description of vortex loop escape we shall neglect such complexity. Instead we shall make use of three scaling relations which apply to Brownian networks and are described in more detail in Sec. 2.14. These expressions relate the mean values in the statistical distributions of the loop diameter  $\mathcal{D}$ , area  $S$ , and density  $n$  to the length  $L$  of the loop:

$$\mathcal{D} = AL^\delta \tilde{\xi}^{1-\delta} \quad , \quad (A \approx 0.93, \delta \approx 0.47) \quad , \quad (22)$$

$$|S| = B\mathcal{D}^{2-\zeta} \tilde{\xi}^\zeta \quad , \quad (B \approx 0.14, \zeta \approx 0) \quad , \quad (23)$$

$$n = CL^{-\beta} \tilde{\xi}^{\beta-3} \quad , \quad (C \approx 0.29, \beta \approx 2.3) \quad . \quad (24)$$

For a Brownian random walk in infinite space the values of  $\delta$ ,  $\beta$  and  $\zeta$  are  $1/2$ ,  $5/2$  and  $0$ .

The important simplification here is that these relations are assumed valid during the entire evolution of the network, until sufficiently large rings are extracted by the bias flow into the bulk. Using Eqs. (22) and (23), we may write Eq. (21) for the energy of a loop in the form

$$\mathcal{E}(\mathcal{D}, t) = \rho_s \kappa \mathcal{D}^2 \left[ \frac{\kappa}{4\pi \tilde{\xi}(t) A^2} \ln \frac{\tilde{\xi}(t)}{\xi} - vB \right] \quad . \quad (25)$$

When the scale  $\tilde{\xi}(t)$  exceeds a critical size  $\tilde{\xi}_c(v)$ , which depends on the particular value of the applied superflow velocity  $v$ ,

$$\tilde{\xi}_c(v) = \frac{1}{A^2 B} \frac{\kappa}{4\pi v} \ln \frac{\tilde{\xi}_c}{\xi} \quad , \quad (26)$$

the energy in Eq. (25) becomes negative and the loops in the network start expanding spontaneously. The total number of loops  $N_b$ , which will be extracted from one neutron bubble, can then be obtained by integrating their density from the smallest size  $\tilde{\xi}_c$  to the upper cutoff, which is provided by the diameter of the entire network, or that of the heated bubble,  $2R_b$ :

$$N_b = V_b \int_{\tilde{\xi}_c}^{2R_b} d\mathcal{D} n(\mathcal{D}) \quad . \quad (27)$$

Here the density distribution  $n(L) = C \tilde{\xi}^{-3/2} L^{-5/2}$ , combined with that for the average diameter  $\mathcal{D}(L) = A(L\tilde{\xi})^{1/2}$ , gives  $n(\mathcal{D}) d\mathcal{D} = 2A^3 C \mathcal{D}^{-4} d\mathcal{D}$ . On inserting this into the integral (27) we obtain

$$N_b = \frac{1}{9} \pi A^3 C \left[ \left( \frac{2R_b}{\tilde{\xi}_c} \right)^3 - 1 \right] \quad . \quad (28)$$

From this equation we see that the requirement  $N_b(v_{\text{cn}}) = 0$  returns us the definition of the threshold velocity  $v_{\text{cn}}$ :  $\tilde{\xi}_c(v = v_{\text{cn}}) = 2R_b$ . This in turn gives us from Eq. (26) for the radius of the heated bubble

$$R_b = \frac{1}{A^2 B} \frac{\kappa}{8\pi v_{\text{cn}}} \ln \frac{2R_b}{\xi(T, P)} \quad , \quad (29)$$

which we used in Sec. 2.9.1 to derive the temperature dependence of the threshold velocity:  $v_{\text{cn}} \propto (1 - T/T_c)^{1/3}$ .

Eqs. (26) and (29) thus show that  $\xi_c \propto 1/v$  and  $R_b \propto 1/v_{\text{cn}}$ , so that we may write for the vortex-formation rate  $\dot{N} = \phi_n N_b$  from Eq. (28)

$$\dot{N} = \frac{1}{9} \pi A^3 C \phi_n \left[ \left( \frac{v}{v_{\text{cn}}} \right)^3 - 1 \right] \quad , \quad (30)$$

where  $\phi_n$  is the neutron flux. This is the form of the measured cubic velocity dependence in the empiric Eq. (8). By inserting  $A \approx 0.93$ ,  $C \approx 0.29$  from Eqs. (22) and (24)

respectively and  $\phi_n \approx 20$  neutrons/min, as determined from the saturation of the event rate  $\dot{N}_e$  in Fig. 19b, we obtain for the rate factor in Eq. (30)  $\gamma \approx 1.6 \text{ min}^{-1}$ , which agrees with the experimental value in Figs. 11 and 19a. We note that the cubic dependence on the applied bias flow in Eq. (30) comes only from the assumption that the whole volume of the heated bubble contributes equally to the production of vortices, while the values of the prefactor  $\gamma$  and of the constant term in Eq. (30) depend on the scaling relations (22–24).

The definition of the threshold velocity  $v_{cni}$ , which applies for an event in which  $i$  rings are formed simultaneously, is roughly consistent with the requirement  $N_b(v = v_{cni}) \approx i$ . This gives  $v_{cni}/v_{cn} \sim i^{1/3}$ , which agrees with the measured result in Fig. 20.

To summarize, we note that the KZ model, combined with the simplest possible interpretation for the loop escape from a random vortex network, reproduces both the measured cubic dependence on the normalized velocity,  $(v/v_{cn})^3$ , and the magnitude of the extraction rate.

### 2.13. Neutron-induced vortex formation at low temperatures

The low temperature properties of superfluid  $^3\text{He}$  could not have been extrapolated from measurements restricted to temperatures above  $0.80 T_c$ , even within the framework of the general theory. Similarly, to understand the neutron-induced vortex formation process, it is important to extend the measurements to lower temperatures. One such study has been performed with NMR down to  $0.4 T_c$  in a rotating sample (Finne et al. 2004a). This measurement is a continuation of the NMR work, which we have discussed so far above  $0.80 T_c$ . Another series of measurements has been performed calorimetrically below  $0.2 T_c$  in a quiescent bath (Bäuerle et al. 1996, 1998a). At these very low temperatures quantized vortex lines have a long life time in zero flow. Thus there is sufficient time after the neutron absorption event to detect the vortices.

NMR measurement in  $^3\text{He-B}$  loses rapidly in amplitude resolution on cooling to lower temperatures: the susceptibility drops with decreasing temperature and the width of the NMR spectrum increases. Thus the change of NMR absorption per one rectilinear vortex line quickly diminishes and single-vortex resolution is lost. Also below  $0.6 T_c$  a new phenomenon enters, namely superfluid turbulence (Finne et al. 2003). If here a few seed vortex loops are injected into rotating vortex-free superflow, they become easily unstable and form a turbulent vortex tangle. In the turbulent state the number of vortices rapidly multiplies and the final state becomes an equilibrium array of rectilinear lines.

In neutron-irradiated superflow this is exactly what happens: First vortex loops are extracted from the neutron bubble and injected into the bias flow. Their number

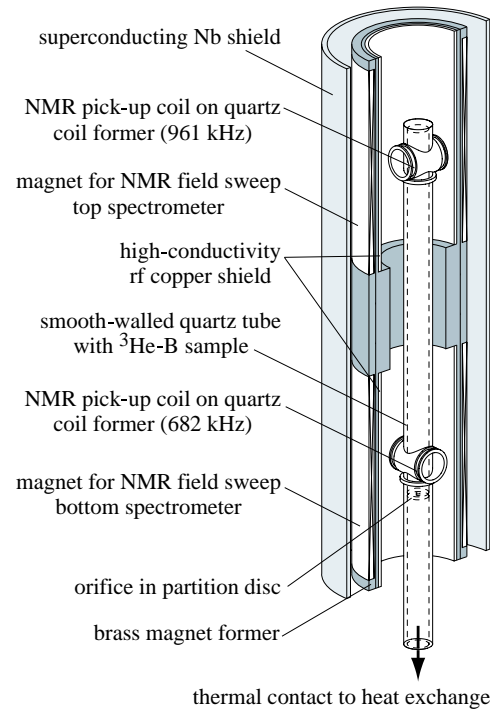


FIG. 21.  $^3\text{He}$  sample with NMR measuring setup. The sample is contained in a fused quartz tube which has a diameter of 6 mm and length 110 mm. This space is separated from the rest of the liquid  $^3\text{He}$  volume with a partition disc. In the center of the disc an orifice of 0.75 mm diameter provides the thermal contact to the liquid column which connects to the sintered heat exchanger on the nuclear cooling stage. Two superconducting solenoidal coil systems with end-compensation sections produce two independent homogeneous field regions with axially oriented magnetic fields. An exterior niobium cylinder provides shielding from external fields and additional homogenization of the NMR fields. The NMR magnets and the Nb shield are thermally connected to the mixing chamber of the pre-cooling dilution refrigerator and have no solid connection to the sample container in the center. The two split-half detection coils are fixed directly on the sample container. (From Finne et al. 2004a).

can be tuned to some extent (in the range 1–5), by choosing the value of the bias velocity (Fig. 19c). Then with some probability, which increases towards lower temperatures and higher bias velocities, turbulence starts. As a result the sample is suddenly filled with the equilibrium number of vortex lines, which means that instead of a few rectilinear lines the final state contains of order  $\sim 10^3$  lines. In these conditions the final state has little connection with the loop extraction process and the details of the neutron-induced vortex formation become lost. But we can use this method to start turbulence in a rotating superfluid column.

### 2.13.1. Experimental techniques

The rotating NMR measurements at low temperatures are performed in the setup of Fig. 21. For the study of turbulence it proved fortunate that this arrangement includes two NMR detection coils at both ends of the long sample cylinder. A second bonus is the relatively high critical velocity of the container so that vortex-free superflow could be maintained to above 3.5 rad/s below  $0.8 T_c$  at 29.0 bar.

On cooling to lower temperatures vortex-free superflow generally becomes more and more difficult to generate and maintain. The lower section of the  $^3\text{He}$  volume below the orifice is directly connected with the sintered heat exchanger. This region is flooded with remanent vortices from the porous sinter already at low rotation. Generally one finds that these vortices start to leak through the orifice into the sample volume on cooling below  $0.6 T_c$ . Surprisingly the sample tube, with which the neutron measurements were performed, seemed immune to this problem in spite of the fact that the orifice had a relatively large diameter of 0.75 mm.

Below  $0.5 T_c$  remanent vortices become a problem. Here successive accelerations to rotation have to be separated by extensive waiting periods at stand still, to allow the slow annihilation of remanent vortices. If rotation is started too soon, remanent vortices are still present and become easily unstable in rotation. As a result vortex-free rotation at velocities above 1 rad/s is then not possible to achieve. Just below  $0.60 T_c$  the waiting time is around 5 min in the container of Fig. 21, but at  $0.40 T_c$  it is found to be 30 min or more. No procedure using rotation in different directions or with different deceleration rates seemed to help in cutting down on the waiting period.

The experimental setup in Fig. 21 is equipped with two independent continuous-wave NMR spectrometers. Each spectrometer includes a split-half excitation/detection coil, wound from thin superconducting wire. The two coils are installed at both ends of the sample cylinder. Each coil is part of a high-Q tank circuit, with a resonance frequency approaching 1 MHz and  $Q \sim 10^4$ . Fig. 22 shows a number of absorption spectra measured with the bottom spectrometer, similar to the high-temperature examples in the left panel of Fig. 6. The spectra illustrate the relevant NMR line shapes and their large width at low temperatures, with varying numbers of rectilinear vortex lines in the sample. Again the peak height of the CF maximum can be calibrated to yield the number of lines  $N$  in the linear limit, when  $N \ll N_{\text{eq}}$ . Often enough, to determine  $N$ , one has to increase  $\Omega$  to some higher reference value where the sensitivity of the CF peak is restored.

Fig. 23 shows an example of a calibration where the CF peak height is measured as a function of  $N$  (or equiva-

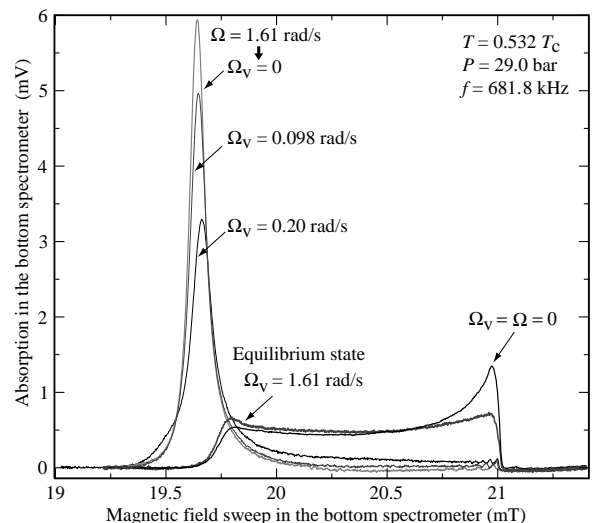


FIG. 22. NMR absorption spectra of  $^3\text{He}$ -B in rotation at low temperatures. As in the left panel of Fig. 6, changes in the line shape can be calibrated to give the number of vortex lines  $N$ . Here  $N$  is characterized by the rotation velocity  $\Omega_v(N)$  at which a given number of lines  $N$  is in the equilibrium state. The different spectra have been measured with the RF excitation at constant frequency  $f$ , using a linear sweep of the axially oriented polarization field  $H$ . The spectra have been recorded at constant temperature and thus all have the same integrated total absorption. The sharp absorption maximum at low field is the counterflow peak (CF). Its shift from the Larmor field (at 21.02 mT) is used for temperature measurement. When a central cluster of rectilinear vortex lines is formed, the height of the CF peak is reduced. In the equilibrium vortex state ( $\Omega = \Omega_v$ ), where the number of vortex lines reaches its maximum, the spectrum looks very different: it has appreciable absorption at high fields and borders prominently to the Larmor edge. This spectrum is more similar to that of the non-rotating state ( $\Omega = 0$ ). As shown in Fig. 23, when the vortex number is small,  $\Omega_v \ll \Omega$ , the reduction in the CF peak height can be calibrated to give  $\Omega_v$  and thus  $N$ . (From Finne et al. 2004a).

lently  $\Omega_v$ ). The measurement has been performed for small vortex clusters ( $N \lesssim 100$ ), by measuring each calibration point in a four step process: 1) First the spectrum is recorded in the vortex-free state in the reference conditions and the CF peak height  $A_0(\Omega_{\text{ref}})$  is obtained. 2) Next a large number of vortex lines is created by irradiating with neutrons (with the rotation at  $\Omega_{\text{ref}}$  or higher). 3) The sample is then decelerated to the low rotation velocity  $\Omega_{\text{low}} \ll \Omega_{\text{ref}}$  so that part of the vortex lines are observed to annihilate. Since the long cylinder is oriented along the rotation axis only within a precision of  $\sim 0.5^\circ$ , this means that any annihilation barrier must be negligible or that at  $\Omega_{\text{low}}$  the sample is in the equilibrium vortex state  $\Omega_{\text{low}} = \Omega_v(N)$ , with a known number of vortex lines  $N$ . 4) Finally the rotation is increased back to the reference value  $\Omega_{\text{ref}}$  and the spectrum is recorded in

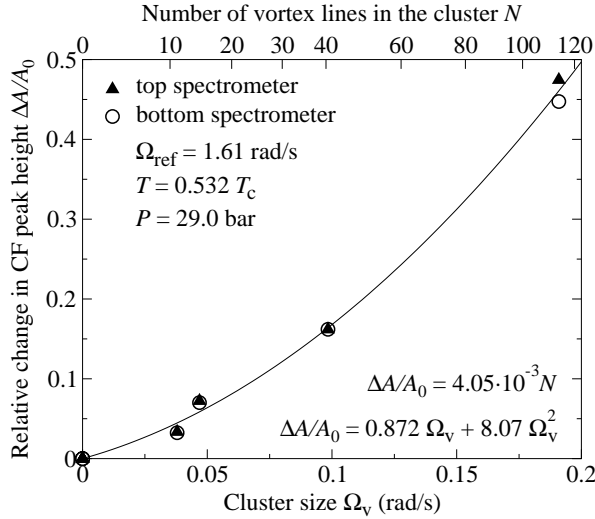


FIG. 23. Calibration of CF peak height  $A$  versus vortex line number  $N$ . The CF peak height in the vortex-free state,  $A_0(\Omega_{\text{ref}})$ , is compared to the peak height  $A(\Omega_{\text{ref}}, \Omega_v(N))$ , which is measured at the same rotation velocity  $\Omega_{\text{ref}}$  for a small vortex cluster of size  $\Omega_v$ , which is prepared as described in the text. The quantity plotted on the vertical scale is the relative reduction in peak heights,  $\Delta A/A_0 = [A_0(\Omega_{\text{ref}}) - A(\Omega_{\text{ref}}, \Omega_v(N))]/A_0(\Omega_{\text{ref}})$ , measured in constant conditions. The solid line is a fit, given by the expression in the figure. The conversion from  $\Omega_v$  (bottom axis) to  $N$  (top axis) in the continuum picture is (Ruutu et al. 1998b)  $N = N_0(1 - d_{\text{eq}}/R)^2$ , where  $N_0 = \pi R^2(2\Omega_v/\kappa)$  and  $d_{\text{eq}} = [\kappa/(8\pi\Omega_v) \ln(\kappa/2\pi\Omega_v r_c^2)]^{1/2}$ . Here  $r_c \sim \xi(T, P)$  is the radius of the vortex core. Using this conversion it is found that  $\Delta A/A_0$  is a linear function of  $N$ , similar to the right panel in Fig. 6. (From Finne et al. 2004a).

order to measure the CF peak height  $A(\Omega_{\text{ref}}, \Omega_v(N))$ . In Fig. 23 the reduction  $\Delta A = A_0(\Omega_{\text{ref}}) - A(\Omega_{\text{ref}}, \Omega_v)$  in the CF peak height of the two spectra is plotted as a function of  $\Omega_v$ . To reduce the dependence on drift and other irregularities it is normalized to the CF peak height  $A_0(\Omega_{\text{ref}})$  of the vortex-free reference state. In contrast to the calibration in the right panel of Fig. 6, this procedure does not rely on single-vortex resolution. However like always, it does require that the order parameter texture is stable and reproducible and that new vortices are not formed during rotational acceleration.

The result in Fig. 23 is a smooth parabola, which becomes a straight line if  $\Delta A/A_0$  is plotted as a function of the number of rectilinear lines  $N$ . Any sample with an unknown number of lines, which is less than the maximum calibrated number, can then be measured in the same reference conditions ( $\Omega_{\text{ref}}$ ,  $T$ , and  $P$ ) and compared to this plot, to determine  $N$ . In Fig. 24 a measurement of vortex formation in neutron irradiation is shown for which the calibration was used. After each irradiation session at different bias flow velocity  $v = \Omega R$  the rotation is changed to  $\Omega_{\text{ref}}$  and the NMR absorption spectrum is recorded. From this spectrum the reduction in CF peak

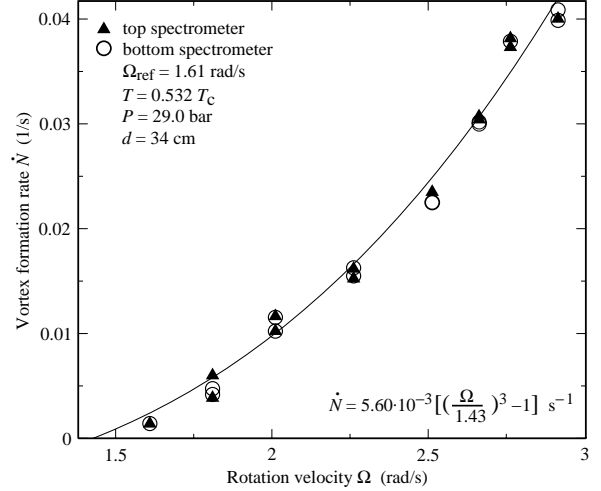


FIG. 24. Rate of vortex formation in neutron irradiation. The average number of rectilinear vortex lines created per unit time during the irradiation period is shown as a function of the rotation velocity  $\Omega$ . The data are fitted with the expression  $\dot{N} = 0.336 [(\Omega/1.43)^3 - 1] \text{ min}^{-1}$  (with  $\Omega$  in rad/s). Depending on the rate  $\dot{N}$ , the irradiation time varies here from 30 min to 4.5 h, so that the number of accumulated vortices remains within the range of the calibration in Fig. 23. This calibration is used to determine the number of vortices from the relative reduction in the CF peak height,  $\Delta A/A_0$ . The distance of the neutron source from the sample was  $d = 34$  cm. The range of the bias flow is limited in these measurements between the critical velocity  $\Omega_{\text{cn}} = 1.43$  rad/s and the upper limit  $\Omega = 3.0$  rad/s, where the turbulent events start to occur. (From Finne et al. 2004a).

height is determined, by comparing to the spectra of the vortex-free state which are measured regularly between neutron irradiation sessions.

### 2.13.2. Measurement of vortex formation rate

In Fig. 24 the rate of vortex formation  $\dot{N}$  is measured at  $0.53 T_c$  as a function of the bias velocity  $v = \Omega R$ , during neutron irradiation. The result supports the cubic rate equation (30). The critical velocity  $v_{\text{cn}} = \Omega_{\text{cn}} R = 4.3$  mm/s is in the same range as the data in Fig. 13. This is plausible if the critical velocity is determined only by the size of the neutron bubble which does not change appreciably with decreasing temperature, Eq. (14). However, the rate factor  $\gamma$  is 40 times smaller than in the measurements above  $0.80 T_c$  and below 21.2 bar (when scaled to the same neutron flux). A second similar measurement at 10.2 bar and  $0.57 T_c$  gives a critical velocity  $v_{\text{cn}} = 3.6$  mm/s and a rate constant  $\gamma$  which is 3 times larger than the measurement in Fig. 24.

These results raise the question how do  $v_{\text{cn}}$  and  $\gamma$  vary over a wider temperature and pressure range. In particular this becomes a problem at high pressures, where a

wide range of stable A phase exists between  $T_c$  and the ambient B-phase bath temperature  $T_0$ , where the irradiation is performed. In the 10 bar measurement A phase is not stable. In both of these measurements the available range of bias velocities is limited (to approximately  $v_{\text{cn}} < v \lesssim 2v_{\text{cn}}$ ), by the appearance of turbulent events at higher velocities. Both of these low temperature measurements are consistent with the cubic form of the rate equation, but do not conclusively prove it owing to the limited velocity range (unlike the high-temperature result in Fig. 19). Clearly more extensive measurements as a function of pressure and temperature are called for.

### 2.13.3. Superfluid turbulence in neutron irradiation

At high rotation and low temperatures below  $0.60 T_c$  neutron irradiation events may become turbulent, similar to vortex formation from other sources (Finne et al. 2003). This means that vortex loops, which have been extracted from the neutron bubble and are injected into the bias flow, may start to interact, to produce a vortex network of large scale. This tangle then blows up and fills the rotating sample with the equilibrium number of vortex lines. Some NMR characteristics of such a neutron capture event are illustrated in Fig. 25. The basic experimental feature here is that the sample is suddenly filled with the equilibrium number of rectilinear vortex lines, apparently as a result of one neutron capture event: The NMR absorption spectrum jumps (via a brief transitory period) from a line shape with a large CF peak to that of the rotating equilibrium state of totally different form (Fig. 22).

Turbulent events are observed in neutron irradiation only if (i) the rotation velocity exceeds  $\Omega_{\text{cn}}$  and (ii) the temperature is sufficiently low so that vortex motion is not heavily damped by mutual friction. Even then these processes are stochastic such that the vortex loops extracted from the neutron bubble only rarely achieve the proper initial conditions in which turbulent loop expansion starts to evolve. With decreasing temperature and increasing rotation the probability of turbulent events increases. This is understandable for the following reasons: (i) With decreasing temperature mutual friction damping is reduced, Kelvin wave excitations on the existing vortices grow in amplitude, more new loops are formed, and via reconnection processes the intersecting loops multiply to a turbulent cascade. (ii) With increasing bias velocity the number of vortex loops, which are injected into the bias flow, rapidly increases (Fig. 19, bottom) and the probability of their intersections increases. Here we shall not discuss general features of turbulent superfluid dynamics, only describe the main signatures of the neutron-induced turbulent events.

Fig. 25 illustrates how the height of the CF peak suddenly drops to zero in the NMR spectrum when a tur-

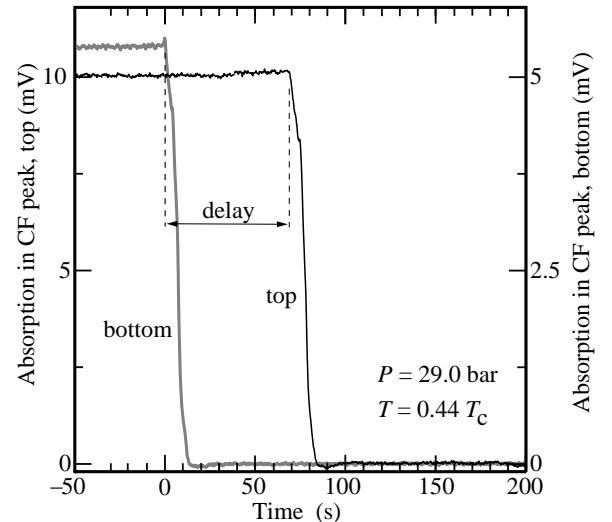


FIG. 25. NMR signatures of turbulent vortex formation in neutron irradiation. The CF peak height (Fig. 22) is monitored as a function of time in the two NMR detection coils. Here a vortex tangle suddenly starts to expand, first in the bottom coil (at  $t = 0$ ), when its CF peak rapidly drops to zero. After a delay of 70 s, which the turbulent front needs to travel to the lower edge of the top coil 90 mm higher along the column, a similar collapse is recorded by the top spectrometer. The flight time  $\tau = z/(\alpha\Omega R)$  corresponds to the situation where  $z = 95$  mm and turbulence is first formed in the middle of the bottom coil. This sequence of events is schematically displayed here at  $\Omega = 1.61$  rad/s. The sudden collapse of the CF peak means that the turbulent tangle is rapidly polarized at these large flow velocities and that the global counterflow between the normal and superfluid components is thereby removed. Measurements of this type show that from the initial injection site, where the extracted vortex loops first start to intersect in the bias flow, turbulence expands by forming two fronts which move at constant velocity towards the top and bottom ends of the rotating column. (From Finne et al. 2004a).

bulent event starts to evolve. In this schematic example the turbulent tangle first appears inside the bottom coil. The collapse of the CF peak height is the first feature in the NMR absorption spectrum which signals the turbulence: Its rapid decay shows that the turbulent state becomes polarized, to mimic on an average solid-body rotation. Simultaneously the NMR absorption intensity from the CF peak is transferred close to the Larmor edge of the spectrum where a new sharp peak rapidly grows in intensity. This new peak then slowly decays to the line shape of the equilibrium state (Fig. 22). The intensity in the Larmor region reflects how the vortex density evolves within the coil: It first rapidly overshoots to a value which is about twice that in equilibrium and then slowly rarefies to the equilibrium value.

The decaying CF signals from the two coils do not overlap in Fig. 25. Even the more slowly relaxing over-

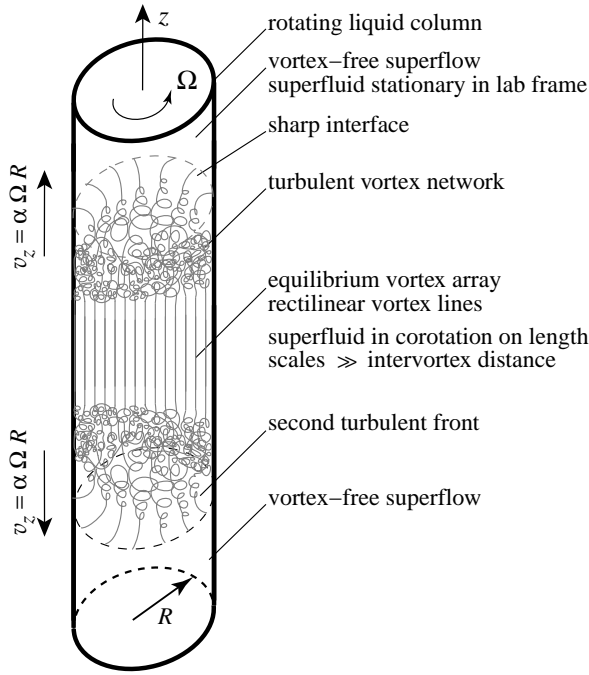


FIG. 26. Turbulent expansion of quantized vorticity in a rotating superfluid column. Initially the column rotates in the vortex-free state. If sufficiently many loops are extracted from a neutron bubble, they may interact to develop a superfluid tangle. The tangle forms with a sharp advancing front and a trailing tail which decays into the equilibrium rotating state with rectilinear lines. Two turbulent fronts thus propagate along the column in opposite directions, while in the middle there exists already an ordered array of rectilinear vortex lines, if the column is sufficiently long. The axial velocity of the fronts is controlled by the dissipative mutual friction  $\alpha$ . The ordered array in the middle remains fixed in the rotating frame, while the two fronts rotate, as determined by the reactive mutual friction  $\alpha'$ .

shoots in the Larmor region do not overlap in time when  $T < 0.5T_c$  and turbulence is initiated at one end of the sample tube. This means that turbulence propagates along the column as a stratified layer: By the time the NMR absorption in the top coil gives the first indication of the approaching turbulent front, the bottom coil has already settled into its stable equilibrium line shape. The turbulent front is formed from a relatively thin layer of disordered tangle. Here the polarization of the circulation reaches its final equilibrium value almost immediately, even before the vortex density has reached its peak, and well before the vortex configuration has stabilized to its equilibrium state of rectilinear lines. These observations suggest that vorticity propagates in the rotating column in the peculiar configuration shown in Fig. 26. Here turbulence does not fill the entire column, only short sections, before it straightens into rectilinear lines. Such a configuration has not been described before – simply

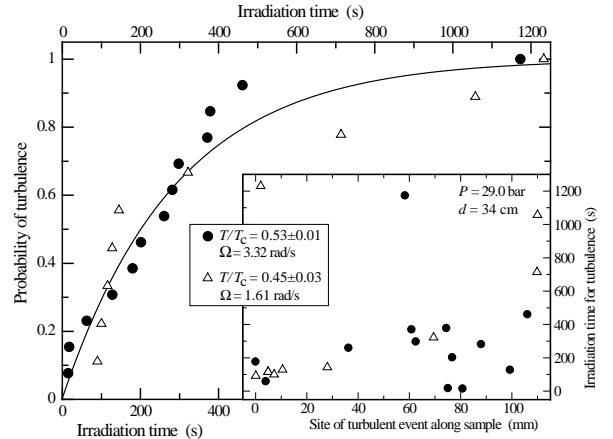


FIG. 27. Turbulent vortex formation in neutron irradiation at 29.0 bar pressure. The sample is irradiated in constant conditions until a turbulent vortex expansion event takes place. The irradiation time required to achieve the turbulent event is measured. Results from measurements at two different constant conditions are shown in this plot in the form of cumulative probability distributions. The solid curve is a fit of the data measured at  $0.53 T_c$  to a distribution function of the form  $P(t) = 1 - (1 - p_n)^{\dot{N}_e t}$ , where the probability of a single neutron absorption event to start turbulence is  $p_n = 0.092$ . The rate  $\dot{N}_e$  of the neutron-induced vortex injection events is taken as  $0.55 \dot{N}$  from Fig. 24 as appropriate for  $v/v_{cn} = 2.32$  (see Fig. 19). There were no cases among the two sets of measurements where a turbulent event would not have been observed after an irradiation period of 20 min. The *inset* shows the axial location of the initial turbulent seed, the site of the neutron capture, measured from the orifice upward with a technique explained in Fig. 25. The corresponding irradiation time needed to achieve the event is shown on the vertical axis. As expected, the sites are randomly distributed along the sample.

because it has not been possible to set up this situation in  $^4\text{He-II}$ , *ie.* one where vortices are injected in high-velocity rotating superflow.

The turbulent front moves along the column with a fixed velocity which was measured by Finne et al. (2004b). This velocity has the same value as that of a single short vortex filament moving along the cylinder wall in the initial vortex-free bias flow:  $v_z = \alpha\Omega R$ . Here  $\alpha$  is the dissipative mutual friction coefficient which was measured by Bevan et al. (1997a). This means that from the delay between the signals of the two detector coils (as marked in Fig. 25), we may calculate the axial location  $z$  where the turbulent event started. This location has been plotted for the data in Fig. 27 in the inset of this figure.

The probability of a neutron capture to trigger a turbulent process is studied in Fig. 27. Two measurements are shown, at different temperatures and rotation velocities. The cumulative probability distribution has been plotted for the irradiation time needed to achieve the

turbulent event. The sample is irradiated at constant conditions until the CF peak is observed to collapse suddenly. The irradiation time is plotted on the horizontal axis. On the vertical axis the number of turbulent events observed within this time is shown, normalized to the total number of events: 13 events in one case (at  $0.53 T_c$ ) and 9 in the second (at  $0.45 T_c$ ). As seen from the plot, the number of events is insufficient to produce smooth probability distributions, but the irradiation times are observed to be distributed over the same range in the two cases, *ie.* their distributions have similar average values and widths. This in spite of the fact that the measurements at  $0.45 T_c$  were performed at half the rotation of those at  $0.53 T_c$ . At high temperatures a reduction by two in velocity results in a significant decrease in the yield of vortex loops from one neutron absorption event (Fig. 19). The fact that the two distributions in Fig. 27 do not differ significantly indicates that with decreasing temperature the transition to turbulence becomes more probable and less sensitive to the initial configuration of the injected loops.

Let us consider the measurement at  $0.53 T_c$  in more detail. The state of the sample changes during the irradiation at constant  $\Omega$ : (i) the initial state is vortex-free, (ii) during the irradiation rectilinear vortex lines are formed at a rate which can be extrapolated from Fig. 24, (iii) until finally all vortex-free CF is completely terminated in a turbulent event. In the final step the state of the sample changes from one with only a small central vortex cluster to one with the equilibrium number of vortex lines ( $N_{\text{eq}} \sim 2600$ ). Note that to observe a new turbulent event the existing vortices have to be annihilated, by stopping rotation. Then the vortex-free state can be prepared again and a new irradiation session can be started. The longest irradiation time is here  $\sim 20$  min. During this period the cluster grows at the rate  $\dot{N} = 3.9$  vortices/min, so that it contains about 80 vortices when the turbulent event finally starts. At this point the CF velocity at the sample boundary  $v = v_n - v_s = \Omega R - \kappa N / (2\pi R)$  has been reduced by 2.7% from the initial state. Since the mean irradiation time in the measured distribution is only  $\sim 250$  s, the reduction in CF velocity by vortices formed before a turbulent event is minor. We may thus view the result in Fig. 27 as representative of these particular values of rotation and temperature.

One may wonder whether a turbulent process results from a single neutron capture event or from the coincidence of two or more events. In the latter case the simultaneous events need to be sufficiently close not only in time, but also in space, so that expanding loops, which have been extracted from the two neutron bubbles, have a possibility to intersect. (The probability of the bubbles themselves to intersect is very small.) The intersection of the loops expanding from the two random positions

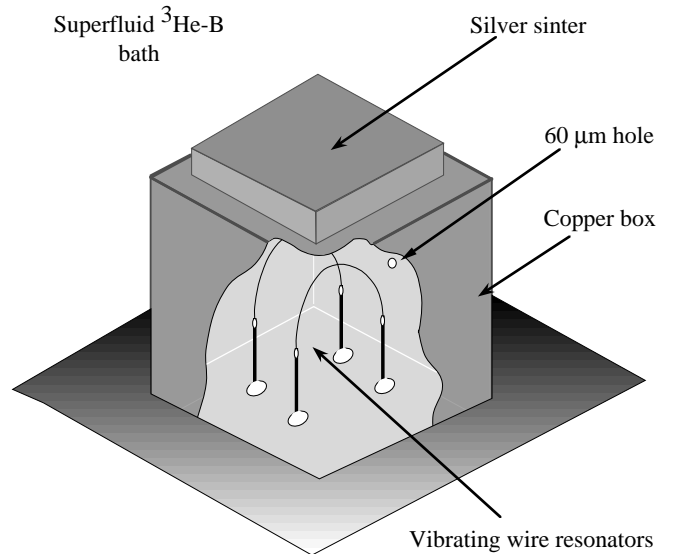


FIG. 28. Bolometer box, which is used to measure calorimetrically the energy balance of the neutron capture reaction in the low temperature limit of ballistic quasiparticle motion. Two vibrating superconducting wire loops are included, one for measuring the temperature of the liquid within the box and the other as a heater to calibrate the calorimetric measurement. (From Bäuerle et al. 1998b).

along the height of the cylindrical sample is more likely to occur closer to the middle than at the top or bottom end. However, the events listed in the inset of Fig. 27 occur randomly along the sample. In all cases the NMR signatures from the turbulent events are similar, there is no prominent variation in their appearance depending on where the event starts. Additionally, at lower temperatures, the turbulent events occur close above  $\Omega_{\text{cn}}$ . Here successful neutron absorption events, which lead to the extraction of loops to the bulk, are rare but, nevertheless, turbulence becomes more probable. From this we presume that a single neutron capture event in suitable conditions must be able to start the turbulence. For a more careful proof of this point the measurements should be repeated as a function of the neutron flux.

To conclude, with decreasing temperature turbulence moves closer to the critical threshold  $v_{\text{cn}}$ . This means that the range of bias velocities, in which the neutron-induced vortex formation process can be studied, decreases and ultimately below  $0.45 T_c$  a measurement of the bias dependence becomes obsolete. Nevertheless, here and at lower temperatures it is a practical technique to start turbulence.

#### 2.13.4. Calorimetry of vortex network

Another type of low temperature experiments are the calorimetric measurements of Bäuerle et al. (1996, 1998a)



which determine the amount of heat which is dumped into the liquid  $^3\text{He-B}$  bath in each individual neutron absorption event. They allow quantitative comparison to the KZ model. These measurements are performed in the very low temperature limit of ballistic quasiparticle motion in a quiescent bath, with zero bias flow.

The measuring probe is a superconducting wire loop. It is oscillated in the liquid with a frequency of a few hundred Hz and a high  $Q$  value, by driving the loop at resonance with an ac current in a dc magnetic field oriented perpendicular to the wire. The damping of the wire oscillations measures the density of quasiparticle excitations in the liquid and can be calibrated to give the temperature. For this a second vibrating wire loop is used as a heater (Fig. 28). The latter is excited with a known current pulse to heat up the liquid, by driving the wire at supercritical velocities where the break-down of Cooper pairs gives rise to a shower of quasiparticles. To contain the ballistically moving quasiparticles, both wire loops are placed inside a box from which the particles leak out through a pin hole at a well-known rate (Bäuerle et al. 1998b).

The thermal connection between the liquid in the calorimeter box and that in the surrounding  $^3\text{He-B}$  bath is only via the small pin hole. A neutron absorption event inside the box heats up the liquid and a thermal pulse is recorded with the wire resonator. The rise time is determined by the resonator properties, while the trailing edge (with a time constant of about 1 min) monitors the much slower leakage of quasiparticle excitations from the box through the orifice. If energy is released into the box on a still longer time scale it is not recorded in the form of pulses.

It is found that neutron absorption events amount to roughly 100 keV smaller thermal pulses than the 764 keV, which a slow neutron is expected to yield for the absorption reaction with a  $^3\text{He}$  nucleus. Since the various recombination channels of the ionized charge and the subsequent thermalization processes in liquid  $^3\text{He}$  are poorly known, it is not quite clear how large an energy deficit one should expect. Obvious losses include the ultraviolet radiation absorbed in the walls of the bolometer box and the retarded relaxation of excited electronic states of helium atoms and molecular complexes. However, Bäuerle et al. (1996, 1998a) expect that these contributions are not strongly pressure dependent and on the order of 7% of the reaction energy. They then ascribe the remaining energy deficit to the random vortex network which is created in the neutron bubble and which in the low temperature limit should have a long life time, when mutual friction approaches zero and no flow is applied.

In Table I the measured missing energy at three different liquid pressures has been compared to that estimated from the KZ model. The measured result  $\Delta E_{\text{exp}}$  is recorded on the top most line while the calculated com-

parison proceeds stepwise from one line to the next in the downward direction of the table. The final result  $\Delta E_{\text{theor}}$  can be found on the lower most line. The thermal diffusion constant,  $D = 3k_{\text{T}}/C_{\text{v}} = v_{\text{F}}^2\tau_{\text{T}}$ , is derived from the conductivity  $k_{\text{T}}$ , which has been tabulated by Wheatley (1975) while all other liquid  $^3\text{He}$  values are taken from Greywall (1986). The agreement between the top and bottom lines is within a factor of 2, which is surprising, if we remember the uncertainties which are built into this comparison. Table I has been included in this context to draw attention on the magnitudes of the different quantities.

The significance of the calorimetric measurement rests entirely on the quantitative analysis of the measured data – whether an energy deficit is present and can be ascribed to vortices. The quantitative analysis is hampered by three kinds of uncertainties:

(1) The proportions of the radiative and retarded contributions in the thermalization after neutron absorption are not known sufficiently well (Leggett 2002).

(2) To calibrate the bolometer box, the heater wire is vibrated at a velocity which exceeds the pair-breaking limit. It is now known that when the vibrating wire loop reaches this limit, then a beam of quasiparticles and vortex loops is created. The fraction of energy spent on generating vortices is temperature dependent and appears to decrease rapidly with increasing temperature. With increasing drive level more and more vortices are formed at different points along the wire loop (Fisher et al. 2001; Bradley et al. 2004). The calibration of the bolometer box then becomes uncertain, if a sizeable fraction of the energy of the calibrating electrical pulse ends up in a long lived turbulent vortex network.

(3) The decay time of a vortex tangle is unknown in the zero temperature limit. The calorimetric measurement of the energy deficit in the neutron absorption event requires a time constant of tens of seconds so that the decay of the tangle would not contribute to the measured thermal pulse. On the other hand, the measurements of Fisher et al. (2001) on vibrating-wire-generated tangles suggest that their time constant of decay is seconds. The simulation calculations of Barenghi and Samuels (2002) suggest even faster decay. However, the decay time is expected to depend on the topology and line density of the vortex tangle since it proceeds via reconnection into loops which fly away in the quiescent bath and finally annihilate on solid surfaces (where part of the energy may go directly to the wall, escaping the liquid). In this respect the random vortex network created in the neutron absorption event (Sec. 2.14.1) is expected to be quite different from the vortex tangle generated by the vibrating wire: According to the measurements of Bradley et al. (2004), during stationary state vortex generation and decay by a vibrating wire the line density reaches only a very low value of  $20\text{mm}^{-2}$  (an inter-vortex dis-

|  | $P$ (bar) |       |       | Source  |
|--|-----------|-------|-------|---|
|  | 0         | 6     | 19.4  |   |
| $\Delta E$ exper. (keV)                | 85        | 95    | 150   | Bäuerle et al. (1996, 1998a)  |
| $T_c$ (mK)                             | 0.93      | 1.56  | 2.22  | Greywall (1986)   |
| $v_F$ ( $10^3$ cm/s)                   | 5.95      | 5.04  | 3.94  | Greywall (1986)   |
| $C_v$ [ $10^3$ erg/( $\text{cm}^3$ K)] | 5.83      | 12.8  | 25.4  | Greywall (1986)   |
| $\xi_0$ (nm)                           | 65        | 33    | 18    | $\xi_0 = \sqrt{7\zeta(3)/(48\pi^2)} \hbar v_F / (k_B T_c)$                      |
| $\tau_0$ (ns)                          | 1.1       | 0.65  | 0.46  | $\tau_0 = \xi_0 / v_F$  |
| $R_b$ ( $\mu\text{m}$ )                | 27        | 17    | 12    | $R_b = \sqrt{\frac{3}{2\pi e}} \left( \frac{E_0}{C_v(T_c - T_0)} \right)^{1/3}$ |
| $\tau_T$ ( $\mu\text{s}$ )             | 0.59      | 0.17  | 0.12  | Wheatley (1975)   |
| $D$ ( $\text{cm}^2/\text{s}$ )         | 21        | 4.3   | 0.94  | $D = v_F^2 \tau_T$  |
| $\tau_Q$ ( $\mu\text{s}$ )             | 0.16      | 0.31  | 0.69  | $\tau_Q = (e/6) R_b^2 / D$  |
| $\xi_v$ ( $\mu\text{m}$ )              | 0.23      | 0.15  | 0.11  | $\xi_v = \xi_0 (\tau_Q / \tau_0)^{1/4}$   |
| $\tilde{D}_b$                          | 210       | 200   | 190   | $\tilde{D}_b = \left( \frac{4}{3} \pi R_b^3 / \xi_v^3 \right)^{1/3}$            |
| $L_v$ (cm)                             | 79        | 43    | 28    | $L_v = (4\pi/3a_l) R_b^3 / \xi_v^2$   |
| $\rho_s$ ( $\text{g}/\text{cm}^3$ )    | 0.081     | 0.094 | 0.108 | $\rho_s \approx \rho$ , Greywall (1986)   |
| $\Delta E$ theor. (keV)                | 170       | 140   | 120   | $\Delta E = (\rho_s \kappa^2 / 4\pi) L_v \ln(\xi_v / \xi_0)$                    |

TABLE I. Comparison of measured and estimated total vortex line energies at different pressures in a random vortex network, as generated by a neutron absorption event according to the KZ model. The ambient temperature of the  $^3\text{He-B}$  bath is taken to be  $T_0 = 0.16$  mK. For the value of  $\tau_Q$  we use the time it takes for the normal phase bubble to disappear. The coefficient  $a_l = 2.1$ , for estimating the total vortex-line length  $L_v$ , is taken from the simulation results in Sec. 2.14.1, when the value of the dimensionless bubble diameter is  $\tilde{D}_b = 200$ .

tance  $\sim 0.2$  mm). In comparison, in Table I the initial line density expected in the neutron bubble, as precipitated by the KZ process, is of order  $10^7 \text{ mm}^{-2}$ .

The original interpretation of the calorimetric measurements supports the KZ model of vortex formation. However, to keep this statement valid in view of recent developments on vortex dynamics at ultra low temperatures, more work is required. In principle a calorimetric measurement of the energy in the random vortex network, which is generated in a neutron absorption event, provides more direct proof of the KZ mechanism, than rotating measurements: Here in the absence of applied flow, the discussion about the superflow instability at the neutron bubble boundary is irrelevant. Also the calorimetric measurement gives directly the domain size  $\xi_v$  of the inhomogeneity in the order parameter distribution (Eq. (3)) right after the quench, which can otherwise be inferred only indirectly from other types of measurement.

It is interesting to note that the understanding gained from the calorimetric work has turned  $^3\text{He-B}$  into an attractive absorber material in the search for dark matter particles. In such a dark matter detector the collision energy will be measured with an array of bolometer boxes equipped with micro-mechanically fabricated vibrating

resonators (Collin et al. 2004). In the next sections we shall analyze further the initial loop formation in the neutron bubble and its later evolution, which we so far have omitted.

## 2.14. Simulation of loop extraction

In spite of the agreement, which we have listed so far between the measured characteristics of neutron-induced vortex formation and the KZ model, a deeper understanding of the processes involved would be important. Owing to its phenomenological content, the KZ model is based on general concepts and contains few media-dependent parameters (such as the superfluid coherence length  $\xi$  or the order-parameter relaxation time  $\tau$ ). These are known in the case of superfluid  $^3\text{He}$ , hence the predictions of the model for the initial state of the vortex network can be calculated. In the rotating experiments the initial state is connected with observable quantities only through the complex evolution of the network, governed by superfluid hydrodynamics. This means that a more rigorous comparison requires numerical simulation.

A number of numerical simulations exist on the evolu-

tion of a network of linear defects. These apply to cosmic strings, liquid crystals, and vortices in superfluid  $^4\text{He}$ . Such results cannot be directly transferred to neutron-induced vortex formation in  $^3\text{He-B}$ . The differences with the cosmic string and liquid crystal calculations arise from the different boundary conditions and the equations which govern the evolution of the network in the applied external bias fields. In the case of superfluid  $^4\text{He}$ , studies of random vortex networks often concentrate on vortex flow driven by thermal counterflow between the normal and superfluid components in a stationary situation (Tough 1982). In contrast, the vortex network, which is produced in  $^3\text{He-B}$  in a neutron absorption event, is in a state of rapid non-stationary evolution. Nevertheless, standard techniques exist (see eg. Schwarz 1978, 1985, 1988) and can be applied for solving also the transient problem in  $^3\text{He-B}$ . Here we describe calculations which address the dependence of the vortex-formation rate on the normalized bias velocity  $x = v/v_{\text{cn}}$  (Ruutu et al. 1998a).

#### 2.14.1. Initial loop distribution

Vachaspati and Vilenkin (1984) developed an approach for the simulation of the initial network of linear defects after a rapid phase transition, adapted to the case of cosmic strings. This technique has been used in most studies since then (see e.g. the reviews by Hindmarsh and Kibble 1995 and Bray 1994).

We approximate the neutron bubble with a cubic volume which is subdivided into smaller cubes, such that the size of these volume elements equals the length scale of the initial inhomogeneity in the order-parameter distribution at the moment of defect formation. This length is on the order of the coherence length and in the simulation it plays the role of a “unit” length: It is a parameter of the model, which has to be derived by other means. In the case of the superfluid transition this length is given by Eq. (3).

An arbitrary phase is assigned to each vertex of the grid, to model the initial random inhomogeneity of the order parameter. It is usually assumed that the distribution of the phase in each segment of the grid between two vertices corresponds to the shortest path in the phase circle. Thus it is possible to determine whether a line defect pierces a given face. Then the centers of the corresponding faces are connected to form closed or open (depending upon specific boundary conditions) linear defects, strings in the cosmological case and vortices in the superfluid.

Vachaspati and Vilenkin assigned to each vertex a value of the phase from the following set:  $\{0, 2\pi/3, 4\pi/3\}$  and then studied the statistical properties of the resulting network of strings. They found that most (70%) of the strings were in the form of open segments, which ex-

tended from one boundary of the system to another. For closed loops they found two scaling relations to hold:

$$n = CL^{-\beta}, \quad (31)$$

and

$$\mathcal{D} = AL^\delta, \quad (32)$$

where  $\beta \approx \frac{5}{2}$ ,  $\delta \approx \frac{1}{2}$ ,  $n$  is the density of loops with a given length  $L$ , and  $\mathcal{D}$  is the average spatial size of a loop. It is usually defined as an average of straight-line dimensions in  $x$ ,  $y$  and  $z$  directions. In this model both the characteristic inter-vortex distance and the radius of curvature are on the order of the length scale of the spatial inhomogeneity (i.e. the size of the small cubes, which here has been set equal to unity). Later, other variations of this model have been studied, including other types of grids and other sets of allowed phases. However, it has been found that the scaling relations (31) and (32) hold universally in each case.

The direct applicability of these results to the case of vortex formation in  $^3\text{He-B}$  is not evident. In cosmology the open lines are the most significant ones: only these strings may survive during the later evolution if no bias field exists to prevent closed loops from contracting and annihilating. In the case of a normal-liquid bubble within the bulk superfluid there exists an obvious boundary condition: the phase is fixed at the boundary and there are no open lines at all. Thus it is of interest to find out the influence of the boundary conditions on the scaling relations (31) and (32).

Another question, which arises in the case of superfluid vortices, concerns the interaction of the loops with the external bias field due to the normal-superfluid counterflow. The energy of a tangled vortex loop in the counterflow is proportional to its algebraic area  $S = \oint y dz$  in the direction  $x$  of the counterflow velocity, Eq. (21). Thus the dependence of  $S$  on the length of the loop is of interest as well.

The simulation is performed in a cubic lattice with a fixed (zero) phase at the outer boundary. The set of allowed phases is not limited. It is known that such limitations affect the number of open lines in cosmic-string simulations, but this should be irrelevant for the network in the neutron bubble. Several vortices may pass through one cell in the grid. In this case the corresponding faces of the cell are connected at random. For calculating the length of a loop, it is assumed that both straight and curved segments of the loop inside one cell have unit length. The size of a loop in the direction of a specific coordinate axis is measured as the number of cells in the projection of the loop along this axis.

The size of the volume, which undergoes the superfluid transition in the neutron absorption event, is about  $50 \mu\text{m}$ , while the characteristic inter-vortex distance in

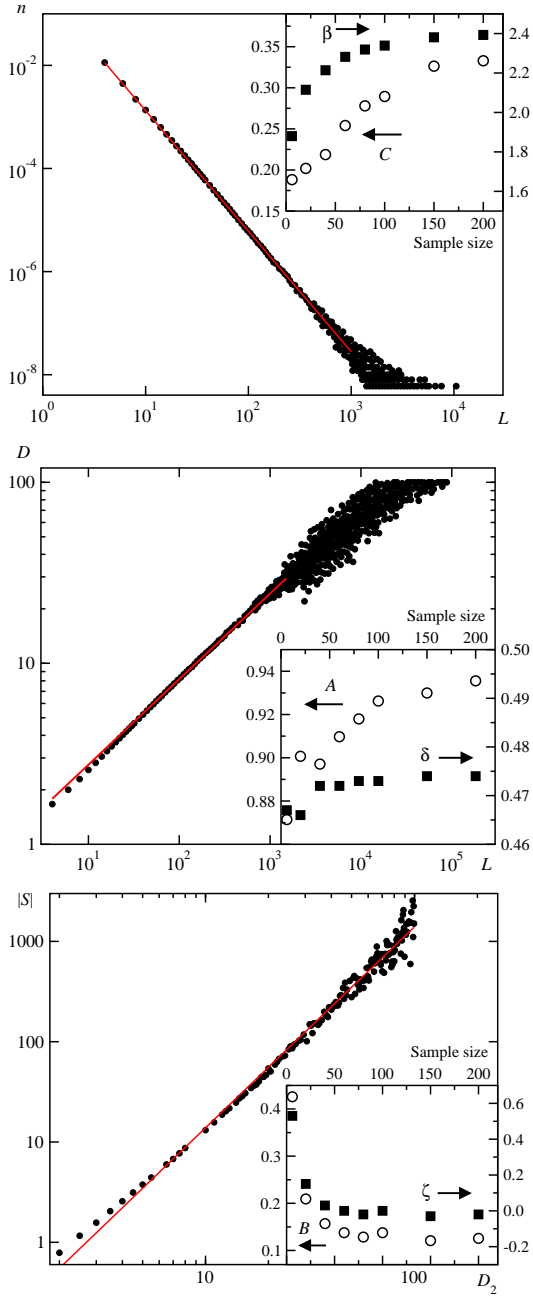


FIG. 29. Scaling properties of vortex loops in the initial network: density  $n$  (*top*) and average spatial size  $\mathcal{D}$  (*middle*), plotted as a function of the length  $L$  of the loops. Below their algebraic area  $|S|$  is shown (*bottom*), as a function of the 2-dimensional spatial size  $\mathcal{D}_2$  of the loop. The calculations are performed on a lattice of  $100 \times 100 \times 100$  cells. The solid lines are fits to scaling laws obeying equations of the form of (31), (32), and (33), respectively. The inset in each plot shows the dependence of the scaling parameters on the size of the cubic neutron “bubble”.

the initial network is of the order of  $1 \mu\text{m}$ . Calculations have been performed for several “bubble” volumes: starting from  $6 \times 6 \times 6$  up to  $200 \times 200 \times 200$ . For each bubble

size the loop distributions obtained from a large number of (up to 1000) initial distributions of random phases are averaged. The resulting distributions of  $n$ ,  $\mathcal{D}$ , and  $S$  are shown in Fig. 29. One can see that despite differences in the boundary conditions the Vachaspati-Vilenkin relations (31) and (32) hold in the case of vortices in superfluid helium, but the exponents and prefactors are slightly different and depend on the size of the bubble.

For the algebraic area  $S$  of a loop as a function of the corresponding 2-dimensional diameter  $\mathcal{D}_2$  the additional scaling law is

$$|S| = B\mathcal{D}_2^{2-\zeta}, \quad (33)$$

where  $\zeta \approx 0$ . Here  $\mathcal{D}_2$  is the average of the straight-line dimensions of a loop in  $y$  and  $z$ -directions. Thus the oriented area of a tangled loop is proportional to the area of a circle of the same straight-line size. The scaling relation (33), as well as (31) and (32), are of the form expected for a Brownian particle, for which the square of the average displacement on the  $i$ -th step is proportional to  $i$  and therefore the mean value of the square of the oriented area is given by

$$\begin{aligned} \langle S^2 \rangle &= \left\langle \left( \sum_{1 \leq i \leq L} y_i \Delta z_i \right)^2 \right\rangle = \sum_{1 \leq i, j \leq L} \langle y_i \Delta z_i y_j \Delta z_j \rangle = \\ &= \sum_{i, j} \langle y_i y_j \rangle \langle \Delta z_i \Delta z_j \rangle = \sum_i \langle y_i^2 \rangle \langle \Delta z_i^2 \rangle \propto \sum_i i \propto L^2 \quad . \end{aligned}$$

These scaling relations were used in the analytic model of vortex-loop extraction from the cooling neutron bubble in the bias flow [*ie.* Eqs. (22) – (24)].

#### 2.14.2. Network evolution under scaling assumptions

After its formation, the vortex network evolves under the influence of the inter-vortex interactions and the normal-superfluid counterflow  $v$ . Its characteristic length scale  $\xi(t)$  increases with time. Vortices start to escape from the bubble when the energy gain due to the external counterflow becomes larger than the energy of the superflow associated with the vortex itself. This corresponds to the critical value of  $\xi$ , expressed by Eqs. (11) or (26).

Tangled vortex flow in superfluid  $^4\text{He}$  has been studied numerically by Schwarz (1978, 1985, 1988), Samuels (1992), Aarts and de Waele (1994), Nemirovskii and Fiszdon (1994), Barenghi et al. (1997), Tsubota and Yoneda (1995), and others. A large number of calculations has been devoted to the evolution of the initial network of cosmic strings (see reviews by Hindmarsh and Kibble 1995; Bray 1994) and also of linear defects in liquid crystals (Toyoki 1994; Zapotocky et al. 1995). In all three cases the initial state is quite similar, but the equations controlling the evolution are different. The common feature is that the interaction between the loops leads to reconnections when the loops cross each other. It has been

shown by Kagan and Svistunov (1994) that the scaling relations remain valid in a random network if the vortices are allowed to reconnect when they cross each other, but all other interactions are neglected for simplicity. In most simulation work, both in the case of cosmic strings and liquid crystals, it has been found that the scaling relations are preserved during the evolution, even if inter-vortex interactions are included.

To calculate the escape rate from the network, two crude assumptions are made, which are essentially the same as in the analytic treatment in Sec. 2.12.2: 1) We assume that the scaling laws remain valid until  $\tilde{\xi}$  grows comparable in size to the critical value in Eq. (26). 2) At this point the influence of the external counterflow becomes suddenly so significant that all sufficiently large loops immediately escape by expanding to a rectilinear vortex line. In the numerical simulations the state before escape is modelled by the same method as was used to construct the initial state. It is assumed that not only the scaling relations but also the statistical properties of the vortex tangle remain the same during the evolution as in the “initial” state with the characteristic length  $\tilde{\xi}$ .

At the moment of escape,  $\tilde{\xi} \sim r_o \propto v_{\text{cn}}/v = 1/x$ , and  $\tilde{\xi}$  is used as the size of a cell in the Vachaspati-Vilenkin method. For integer values of  $x$  the bubble is represented by a grid with  $x \times x \times x$  vertices and a random phase is assigned to each vertex. To satisfy the boundary condition, this grid is surrounded by a shell of vertices with fixed zero phase, representing the uniform bulk superfluid outside the heated bubble. Thus the whole grid contains  $(x+1) \times (x+1) \times (x+1)$  cells. Such a correspondence between the size of the grid and the velocity is not too artificial even at small values of  $x$ : for example, at the critical velocity  $v = v_{\text{cn}}$  one gets a grid with  $(x+1)^3 = 8$  cells and  $3 \times 3 \times 3$  vertices, but the phase can be non-zero only at one vertex in the middle of the grid. In this case no vortices can appear in agreement with the definition of  $v_{\text{cn}}$ .

By counting the vortex lines produced from a number of random-phase distributions it is possible to calculate the probability distribution for the number of loops escaping per absorption event. For these calculations it is assumed that each loop, which survives until the moment when  $\tilde{\xi} \sim r_o$ , will form an observable vortex line: In the case of a tangled loop the probability is high that at least one arc is oriented favorably with respect to the counterflow and will be extracted.

In Fig. 30 the calculated probability distribution is plotted for observed neutron absorption events at different values of  $x$  ( $x = 2, 3$ , and  $4$ ) expressed as the fraction of those neutron absorption events which produce a given number of vortices, normalized by the number of all events which give rise to at least one vortex. These results are in remarkably good agreement with the experimental data (without any fitting parameters). However, the

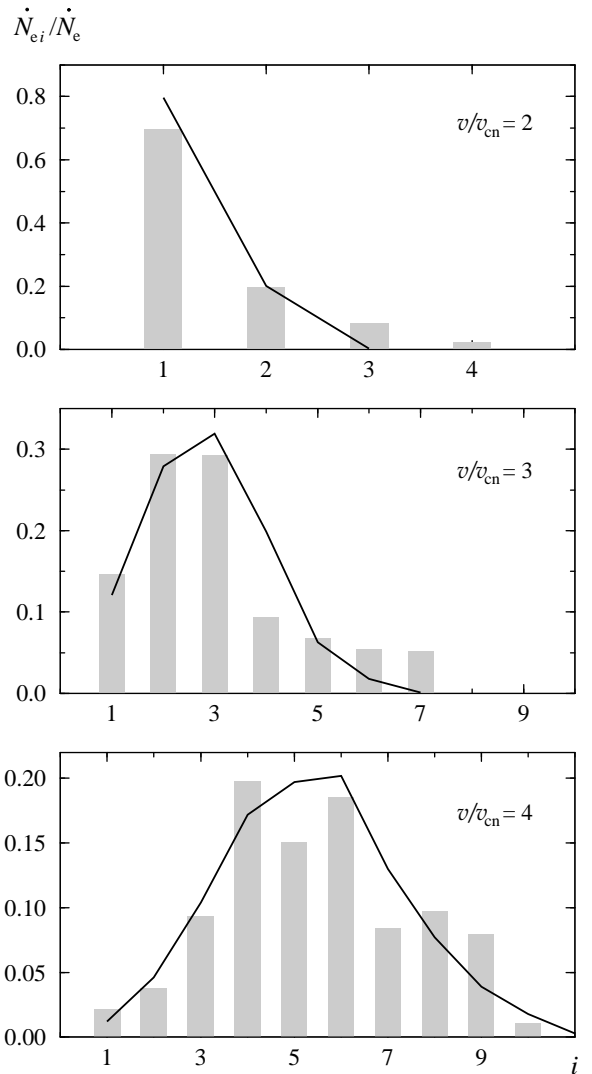


FIG. 30. Distribution of the number of loops escaping per absorption event, normalized to the total number of absorption events and given at three different values of the external bias field,  $v/v_{\text{cn}}$ . The solid lines represent the simulations while the bars denote the experiment.

agreement with the fraction of “zero” events, i.e. absorption events which produce no vortices at all, is poorer, underestimating their number, especially at  $x = 2$ . Experimentally the “zero” events can be extracted from the measured data by comparing the event rate at a given rotation velocity with the saturated event rate at the highest velocity.

One reason for this discrepancy is that at low  $R_b/r_o$  ratio (ie. at low velocities) loops with a radius of curvature  $\sim r_o$ , which are capable of escape into the bulk superfluid, have a rather large probability to be oriented in such a way that they do not have sufficiently large segments oriented favorably with respect to the counterflow, owing to space constraints. Hence they contract and do

not give a contribution to the observed signal. Taking this into account one could develop more elaborate techniques for counting vortices than the simple “count all” method described above. In this case better agreement with all experimental data could be achieved. Particularly, if only vortices with positive algebraic area with respect to the counterflow ( $S = \oint y dz$ ) are counted, then good agreement with the number of “zero” events would be obtained. However, such refinements do not change the results essentially, compared to uncertainties of the model.

### 2.14.3. Direct simulation of network evolution

There is no direct evidence for the validity of the assumptions, which were made in the previous section about the evolution of the network, ie. whether the network remains self-similar (or scale invariant) and the scaling laws Eqs. (31) – (33) can be applied during its later evolution. Preliminary calculations have been carried out using the techniques developed by Schwarz for the simulation of superfluid turbulence in  $^4\text{He}$ . These methods give good numerical agreement with experimental data in  $^4\text{He}$  (Schwarz 1978, 1985, 1988) and have been used extensively by Schwarz and many others (Aarts and de Waele 1994; Nemirovskii and Fiszdon 1994; Samuels 1992; Barenghi et al. 1997; Tsubota and Yoneda 1995).

In such calculations vortices are generally considered to be 1-dimensional objects without internal structure. In  $^4\text{He}$  the diameter of the core is much smaller than other characteristic lengths, foremost the average radius of curvature for the loops or the inter-vortex distance, and even  $\ln(\tilde{\xi}/\xi)$  can be treated as a large parameter. This is not the case in  $^3\text{He-B}$  due to the large coherence length, especially in the early stages of the evolution when the vortex density is largest. However, as mentioned in Sec. 2.3, the characteristic inter-vortex distance and the radius of curvature may still be several times larger than the coherence length and the diameter of the vortex core. For now, we shall continue considering the vortices as linear objects.

There are several forces acting on a vortex line in a superfluid (Donnelly 1991). The Magnus force appears in the presence of superflow,

$$\mathbf{f}_M = \rho_s \kappa \nu \mathbf{s}' \times (\mathbf{v}_L - \mathbf{v}_{sl}), \quad (34)$$

where  $\mathbf{s}$  is the radius vector of a point on the vortex line and the prime denotes the derivative with respect to the length of the line (ie.  $\mathbf{s}'$  is a unit vector tangent to the vortex line at  $\mathbf{s}$ ),  $\mathbf{v}_L = \dot{\mathbf{s}}$  is the local velocity of the vortex line, and  $\mathbf{v}_{sl}$  is the local superfluid velocity at this point. For singular vortices in  $^3\text{He-B}$  the number of circulation quanta is  $\nu = 1$ . The local superfluid velocity  $\mathbf{v}_{sl}$  is a

sum of the superfluid velocity  $\mathbf{v}_s$  far from the network and the velocity induced by all the vortices in the tangle:

$$\mathbf{v}_{sl}(\mathbf{r}) = \mathbf{v}_s + \frac{\kappa}{4\pi} \int_{\text{all loops}} \frac{(\mathbf{s} - \mathbf{r}) \times d\mathbf{s}}{|\mathbf{s} - \mathbf{r}|^3}. \quad (35)$$

The Iordanskii force arises from the Aharonov-Bohm scattering of quasiparticles from the velocity field of the vortex,

$$\mathbf{f}_{\text{Iordanskii}} = \rho_n \kappa \nu \mathbf{s}' \times (\mathbf{v}_L - \mathbf{v}_n), \quad (36)$$

where  $\mathbf{v}_n$  is the velocity of the normal component (ie. the heat bath of the fermionic quasiparticles). The Kopnin or spectral flow force has the same form, but originates from the spectral flow of the quasiparticle levels in the vortex core:

$$\mathbf{f}_{\text{sf}} = m_3 \mathcal{C}(T) \kappa \nu \mathbf{s}' \times (\mathbf{v}_L - \mathbf{v}_n), \quad (37)$$

where the temperature dependent parameter  $\mathcal{C}(T)$  determines the spectral flow in the core. All these three forces are of topological origin: they act in the transverse direction and are thus nondissipative. They are discussed in more details in Sec. 3.

In contrast, the nontopological friction force  $\mathbf{f}_{\text{fr}}$  acts in the longitudinal direction,

$$\mathbf{f}_{\text{fr}} = -d_{\parallel} \rho_s \kappa \nu \mathbf{s}' \times [\mathbf{s}' \times (\mathbf{v}_n - \mathbf{v}_L)]. \quad (38)$$

Here the factor  $\rho_s \kappa \nu$  is the same as in the Magnus force.

Neglecting the vortex mass, we may write the force balance equation for the vortex element:

$$\mathbf{f}_M + \mathbf{f}_{\text{Iordanskii}} + \mathbf{f}_{\text{sf}} + \mathbf{f}_{\text{fr}} = 0. \quad (39)$$

It is convenient to rewrite the balance of forces in the following form:

$$\mathbf{s}' \times [(\mathbf{v}_L - \mathbf{v}_{sl}) - \alpha'(\mathbf{v}_n - \mathbf{v}_{sl})] = \alpha \mathbf{s}' \times [\mathbf{s}' \times (\mathbf{v}_n - \mathbf{v}_{sl})], \quad (40)$$

where  $\alpha$  and  $\alpha'$  are the dimensionless mutual friction coefficients. The  $\alpha$  parameters are actually the experimentally determined mutual friction quantities (see eg. Bevan et al. 1997b). The inverse coefficients are the  $d$  parameters:

$$\alpha + i(1 - \alpha') = \frac{1}{d_{\parallel} - i(1 - d_{\perp})}, \quad (41)$$

where  $i = \sqrt{-1}$ . The transverse mutual friction parameter  $d_{\perp}$  is expressed in terms of three temperature dependent functions which determine the Magnus, Iordanskii and spectral-flow forces:

$$d_{\perp}(T) = (m_3 \mathcal{C}(T) - \rho_n(T)) / \rho_s(T). \quad (42)$$

Eq. (40) is complicated because of the term (35) which contains the integral over the vortex network. To solve Eq. (40), one may follow Schwarz and neglect the influence of all other vortex segments on  $\mathbf{v}_{sl}$  except the one containing the point of interest (the so called local self-induced approximation). In this case

$$\mathbf{v}_{sl} \approx \mathbf{v}_s + \beta \mathbf{s}' \times \mathbf{s}'', \quad \text{where } \beta = \frac{\kappa}{4\pi} \ln \frac{\tilde{\xi}}{\xi}. \quad (43)$$

The leading correction to this simplification comes from the nearest neglected vortex segments and can be estimated to be of order  $\tilde{\xi}/[b \ln(\tilde{\xi}/\xi)]$ , where  $b$  is the average inter-vortex distance. For a network in  $^3\text{He-B}$ ,  $\tilde{\xi} \sim b$  and  $\ln(\tilde{\xi}/\xi) \sim 1$  in the early stages of the evolution and thus at this point the approximation is rather crude. However, the main effect in the initial stages arises from the reconnection of vortex lines which happen to cross each other and this effect is taken into account below.

A second simplification close to  $T_c$  comes from  $\alpha' \ll \alpha$ . We may rewrite the equation of vortex motion in the form:

$$\mathbf{v}_L = \mathbf{v}_s + \beta \mathbf{s}' \times \mathbf{s}'' + \alpha \mathbf{s}' \times [(\mathbf{v}_n - \mathbf{v}_s) - \beta \mathbf{s}' \times \mathbf{s}'']. \quad (44)$$

In the rotating reference frame the normal component is at rest,  $\mathbf{v}_n = 0$ , and one has  $\mathbf{v}_s = -\mathbf{v}$ , where  $\mathbf{v} = \mathbf{v}_n - \mathbf{v}_s$  is the counterflow velocity. We shall be comparing to experimental results measured at  $T = 0.96 T_c$  and  $P = 18$  bar, where the most detailed data were collected. In these conditions  $\alpha \approx 10$  (Bevan et al. 1995) and in the rotating frame Eq. (44) can be simplified further to the form

$$\dot{\mathbf{s}} = \alpha \beta \mathbf{s}'' + \alpha \mathbf{s}' \times \mathbf{v}, \quad (45)$$

The first term on the right hand side of Eq. (45) causes a loop to shrink while the second represents growth or shrinking, depending upon the orientation of the loop with respect to the counterflow.

In the numerical calculation vortices are considered as lines in the same 3-dimensional lattice as before. The temporal and spatial coordinates are discrete and therefore the network evolves in discrete steps: During each step in time a vertex of a loop can jump to one of the adjacent vertices of the lattice. The probability of a jump in any direction is proportional to the component of  $\dot{\mathbf{s}}$  in Eq. (45) in this direction, so that the average velocity equals  $\dot{\mathbf{s}}$ . Other more elaborate representations of vortex loops, based on splines for instance, have been used to model the dynamics of smooth vortex lines in the continuous space. However, for the preliminary study of the network evolution the simplest lattice representation was used. The simple case of one circular loop in the counterflow, where the result is known analytically, can be checked separately and it is found to give correct results.

It is well known that the interactions between neighboring vortex segments in the tangle play an important role in the evolution of a dense network. These interactions lead to the reconnection of loops which cross each other. The reconnections are the main source for the rarefication of the network at the initial stages of evolution, which process through formation and decay of small loops. The reconnection process has been studied numerically (Schwarz 1985; Koplik and Levine 1993) and was found to occur with a probability close to unity for vortex lines approaching each other. In the simulations the vertices are connected in such a way that closed loops are obtained after each time step during the evolution. If a cell is pierced by two vortices, the two segments coming in and the two segments going out are connected randomly. This corresponds to a reconnection probability of 0.5. It is reasonable to suppose that this convention leads to a slowing down in the evolution, in particular in the initial phase, but does not produce gross qualitative changes.

The vortex tangle is initially produced by the procedure described in Sec. 2.14.2, in a lattice  $40 \times 40 \times 40$ , and its evolution is followed until all vortices have disappeared or loops have expanded and formed circular planar rings far from their location of origin. These large rings are counted, since it is fair to assume that each one of them will produce a detectable rectilinear vortex line in the rotating container. The calculation is repeated for a large number of random initial distributions of the phase at any given value of  $v$ . The results are averaged to obtain the average number of vortices  $N_b$ , which are produced from one simulated bubble as a function of  $v$ , and are compared to experimental data in Fig. 31. It is also possible to study the validity of the scaling law (31) at different stages of the evolution in the course of these simulations. In the absence of counterflow ( $v = 0$ ) it is found that the relation is valid for large loops,  $L > 4\tilde{\xi}$ , at least during much of the early evolution (in the late stages, when  $n$  approaches zero, the statistical noise exceeds  $n$ ).

Fig. 31 illustrates the simulation results. No vortices are obtained at low counterflow velocity  $v < v_{cn}$ , but when  $v > v_{cn}$ , their number  $N_b$  starts to increase rapidly with  $v$ . The value of the threshold velocity  $v_{cn}$  corresponds to the situation when the largest radius of curvature  $r_o(v_{cn})$  becomes equal to the diameter of the initial volume of the vortex network (ie. the diameter of the heated bubble). It then becomes possible for a loop to escape into the bulk superfluid if it consists of at least one arc with sufficiently large radius of curvature  $\geq r_o$ . The same calculations were also performed for a tangle with an initial volume of  $20 \times 20 \times 20$ , but no differences were found in the dependence  $N_b(v/v_{cn})$ . This is additional circumstantial evidence for the fact that the scaling relations approximately survive during the evolution of the

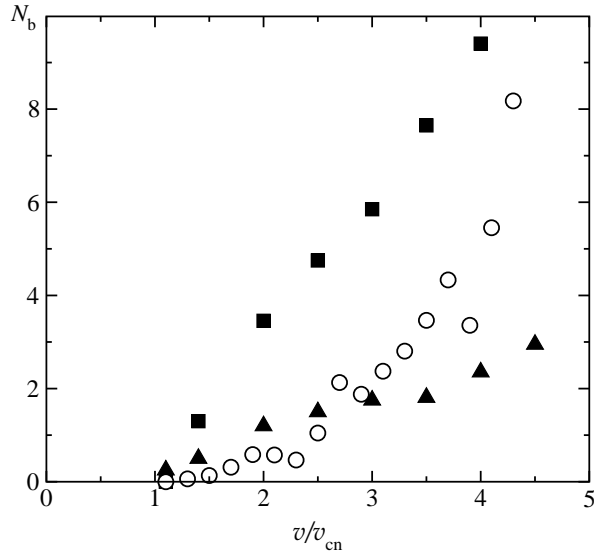


FIG. 31. The number of vortices  $N_b$  escaped from the bubble heated by one absorbed neutron as a function of  $v/v_{cn}$ : (■) simulation of the network evolution in the local self-induced approximation (Eq. (43)) and (▲) by including in addition approximately the polarization of the tangle by the superflow (Eq. (46)). Both calculations were performed on a  $40 \times 40 \times 40$  lattice, but the results remain unchanged if the lattice is reduced in size to  $20 \times 20 \times 20$ . The experimental data (○) represent measurements at  $P = 18$  bar and  $T = 0.96 T_c$  (Ruutu et al. 1998a).

network also in the counterflow until the moment of escape and that the network can be approximated as scale invariant.

The experimental data (denoted with (○) in Fig. 31) fit the universal dependence  $N_b(v/v_{cn}) = \tilde{\gamma}[(v/v_{cn})^3 - 1]$ , where  $\tilde{\gamma}$  equals  $\gamma$  in Eq. (8) divided by the neutron flux. The numerical results (■) lie higher (note that no fitting parameters are involved) and do not display a cubic dependence in the experimental range  $1 < v/v_{cn} < 4$ . The differences could be explained by the approximations in the expression for  $\mathbf{v}_{sl}$ , which neglect significant contributions from the inter-vortex interactions. The polarization by the external counterflow causes the loops with unfavourable orientation to contract and loops with the proper winding direction and orientation to grow. However, as the polarization evolves, it also screens the vortex tangle from the external counterflow. To check whether the polarization has a significant effect on the results, the calculations were repeated by taking the screening approximately into account in the expression for  $\mathbf{v}_{sl}$ :

$$\mathbf{v}_{sl} = \mathbf{v}_s + \beta \mathbf{s}' \times \mathbf{s}'' + \frac{\kappa}{4\pi} \int_{\text{other loops}} \frac{1}{V} \int d\mathbf{r} \frac{(\mathbf{s} - \mathbf{r}) \times d\mathbf{s}}{|\mathbf{s} - \mathbf{r}|^3}. \quad (46)$$

Here the contribution from each loop to the superflow is averaged over the volume. The results (▲) show that this

effect is significant and should be taken into account more accurately, to reproduce the network evolution correctly.

To summarize we note that the preliminary simulation work shows that it is possible to obtain numerical agreement between the KZ mechanism and the rotating experiments, if one assumes that the scaling relations of the initial vortex tangle are roughly obeyed also during its later evolution in the presence of the external superflow. This assumption should still be checked with sufficiently accurate simulation, with full account of the non-local inter-vortex interactions. Future simulation of transient networks should then answer the question how much information about the initial state of the vortex tangle can be retrieved from the rotating experiment, where only the final stationary state result is measured.

## 2.15. Superfluid transition as a moving phase front

In any real laboratory system a rapid phase transition becomes inhomogeneous: The transition will be driven by a strong gradient in one or several of the externally controlled variables. In the case of the superfluid transition in the aftermath of a neutron absorption event it is a steep and rapidly relaxing thermal gradient. In this situation even a second order transition becomes spatially inhomogeneous and is localized into a phase front. In the limit of very fast transitions the order-parameter relaxation slows down the propagation of the superfluid phase and the thermal front, where the temperature drops below  $T_c$ , may escape ahead. This means that the moving phase boundary breaks down into a leading thermal front and a trailing superfluid interface. The width of the region between these two zones is determined by the relative velocities of thermal and superfluid relaxations. Thermal fluctuations in this region are amplified in the transition process and are carried over as order-parameter inhomogeneity into the new symmetry-broken phase. This is the central claim of the KZ model. Below we shall briefly discuss the influence of the thermal gradient on defect formation, as analyzed by Kibble and Volovik (1997) and Kopnin and Thuneberg (1999).

### 2.15.1. Neutron absorption and heating

The decay products from the neutron absorption reaction generate ionization tracks which can be estimated from a standard calculation of stopping power (Meyer and Sloan 1997). This leads to a cigar-shaped volume of ionized particles, with the largest concentration at the end points of the two tracks. The probabilities and relaxation times of the different recombination channels for the ionized charge are not well known in liquid  $^3\text{He}$ . Also the thermalization of the reaction energy may not pro-



duce a heated region which preserves the shape of the original volume with the ionized charge.

Initially the recombination processes are expected to lead to particles with large kinetic energies in the eV range, which are well outside the thermal distribution and for which the recoil velocities become more and more randomly oriented. Energetic particles suffer collisions with their nearest neighbors and the mean free path increases only slowly for atoms participating in these collisions, until all particles are slowed down and become thermalized to the ambient conditions (Bunkov and Timofeevskaya 1998a,b). This means that the reaction energy remains initially localized. In the calorimetric experiments at the lowest temperatures (Bäuerle et al. 1996, 1998a) the thermal mean free path exceeds the container dimensions. Nevertheless, the energy is probably not immediately dispersed into the entire container volume, but remains centralized within a bubble of limited size during cooling through  $T_c$ , when the vortex network is formed. This is the conclusion to be drawn from the comparison between experiment and the KZ mechanism in Table I, where it is assumed that the thermal diffusion mean free path is the same as in the normal fluid at  $T_c$ .

In an inhomogeneous initial state with large thermal gradients the second order phase transition is turned into one where a normal-to-superfluid phase front with finite width sweeps through the heated bubble. If the velocity of the phase front,  $v_T \sim R_b/\tau_Q \sim 6$  m/s, is sufficiently high, comparable to a critical value  $v_{Tc} \sim v_F (\tau_0/\tau_Q)^{1/4}$ , then the KZ mechanism is again expected to dominate, similarly as in the homogeneous case (Kibble and Volovik 1997).

In contrast, if the majority of the kinetic energy is assumed to be thermalized by quasiparticles with energies comparable to the high-energy tail of the thermal Maxwellian velocity distribution, then the mean free paths are long, the volume heated above the ambient becomes large, and its temperature distribution may even become nonmonotonic like in a “Baked Alaska”, as has been described by Leggett (1992). The Baked Alaska scenario is also popular in high energy physics, where the formation of the false vacuum with a chiral condensate after a hadron-hadron collision is considered (Bjorken 1997; Amelino-Camelia et al. 1997). In both cases a rather thin shell of radiated high energy particles expands, with the speed of light in a relativistic system and with the Fermi velocity  $v_F$  in  ${}^3\text{He}$ , leaving behind a region at reduced temperature. Since this interior region is separated from the exterior vacuum by the hot shell, the cooldown into the broken symmetry state in the center is not biased by the external order parameter state. The Baked Alaska mechanism thus can solve the problem of the neutron-mediated formation of B phase from supercooled bulk A liquid (Leggett 1992), while in high energy physics it opens the possibility for the formation of a bubble of chi-

ral condensate in a high energy collision (Bjorken 1997; Amelino-Camelia et al. 1997).

In such conditions, when the quasiparticle mean free path exceeds or is comparable to the dimensions of the heated bubble, temperature is not a useful quantity for the description of its cooling. Most of the analysis of the previous sections is applicable only if we assume that the reaction energy remains reasonably well localized while the hot bubble cools through  $T_c$ . In this case there is no Baked-Alaska effect: No hot shell will be formed which would separate the interior from the exterior region. In this situation the exterior region could be imagined to fix the phase in the cooling bubble, while the phase front is moving inward, suppressing the formation of new order-parameter states, which are different from that in the bulk superfluid outside, and in the same manner suppressing the formation of vortices. However, it appears that there also exists another alternative: The influence of the exterior region may not be decisive if the phase transition front moves sufficiently rapidly. Which of these alternatives is realized in a particular situation is still very much a subject of discussion.

For the interpretation of the measurements in neutron irradiation, a sophisticated understanding of the shape and size of the constant temperature contours within the heated bubble is not vitally necessary. In the final results the bubble size does not enter, since the data can be normalized in terms of the measured threshold velocity  $v_{cn}$ . Its measurement provides an estimate of the circumference of the bubble, since the largest possible vortex ring has to be comparable in size to the neutron bubble. The diameter of this ring is 1–2 orders of magnitude larger than the expected average inter-vortex distance  $\xi_v$  in the initial random network which is created by the KZ mechanism.

### 2.15.2. Thermal gradient and velocity of phase front

For a rough understanding of the superfluid transition in a temperature gradient let us consider the time dependent Ginzburg-Landau (TDGL) equation for a one-component order parameter  $\Psi = \Delta/\Delta_0$ :

$$\tau_0 \frac{\partial \Psi}{\partial t} = \left(1 - \frac{T(\mathbf{r}, t)}{T_c}\right) \Psi - \Psi |\Psi|^2 + \xi_0^2 \nabla^2 \Psi \quad , \quad (47)$$

where the notations for  $\tau_0 \propto 1/\Delta_0$  and  $\xi_0$  are the same as in Sec. 2.3. This equation is the so-called over-damped limit of the more general TDGL equation which has a time derivative of second order. The over-damped limit has been used in numerical simulations (Laguna and Zurek 1997; Antunes et al. 1999; Aranson et al. 1999) and analytical estimations (Dziarmaga 1998, 1999) of the density of topological defects in a homogeneous quench.

An extension of the above equation to superconductivity was used by Ibaceta and Calzetta (1999) to study the formation of defects after a homogeneous quench in a 2-dimensional type II superconductor.

If the quench occurs homogeneously in the whole space  $\mathbf{r}$ , the temperature depends only on one parameter, the quench time  $\tau_Q$ :

$$T(t) = \left(1 - \frac{t}{\tau_Q}\right) T_c . \quad (48)$$

In the presence of a temperature gradient, say, along  $x$ , a new parameter appears, which together with  $\tau_Q$  characterizes the evolution of the temperature:

$$T(x - v_T t) = \left(1 - \frac{t - x/v_T}{\tau_Q}\right) T_c . \quad (49)$$

Here  $v_T$  is the velocity of the temperature front which is related to the temperature gradient (Kibble and Volovik 1997)

$$\nabla_x T = \frac{T_c}{v_T \tau_Q} . \quad (50)$$

With this new parameter  $v_T$  we may classify transitions to belong to one of two limiting regimes: slow or fast propagation of the transition front. At slow velocities,  $v_T \rightarrow 0$ , the order parameter moves in step with the temperature front and

$$|\Psi(x, t)|^2 = \left(1 - \frac{T(x - v_T t)}{T_c}\right) \Theta(1 - T(x - v_T t)/T_c) . \quad (51)$$

Here  $\Theta$  is the step function. In this case phase coherence is preserved behind the transition front and no defect formation is possible.

The opposite limit of large velocities,  $v_T \rightarrow \infty$ , is more interesting. Here the phase transition front lags behind the temperature front (Kopnin and Thuneberg 1999). In the space between these two boundaries the temperature is already below  $T_c$ , but the phase transition did not yet happen, and the order parameter has not yet formed,  $\Psi = 0$ . This situation is unstable towards the formation of blobs of the new phase with  $\Psi \neq 0$ . This occurs independently in different regions of space, leading to vortex formation via the KZ mechanism. At a given point  $\mathbf{r}$  the development of the instability can be found from the linearized TDGL equation, since during the initial growth of the order parameter  $\Psi$  from zero the cubic term can be neglected:

$$\tau_0 \frac{\partial \Psi}{\partial t} = \frac{t}{\tau_Q} \Psi . \quad (52)$$

This gives an exponentially growing order parameter, which starts from some seed  $\Psi_{\text{fluc}}$ , caused by fluctuations:

$$\Psi(\mathbf{r}, t) = \Psi_{\text{fluc}}(\mathbf{r}) \exp \frac{t^2}{2\tau_Q \tau_0} . \quad (53)$$

Because of exponential growth, even if the seed is small, the modulus of the order parameter reaches its equilibrium value  $|\Psi_{\text{eq}}| = \sqrt{1 - T/T_c}$  after the Zurek time  $t_{\text{Zurek}}$ :

$$t_{\text{Zurek}} = \sqrt{\tau_Q \tau_0} . \quad (54)$$

This occurs independently in different regions of space and thus their order-parameter phases are not correlated. The spatial correlation is lost over distances exceeding  $\xi_v$  when the gradient term in Eq. (47) becomes comparable to the other terms at  $t = t_{\text{Zurek}}$ . Equating the gradient term  $\xi_0^2 \nabla^2 \Psi \sim (\xi_0^2 / \xi_v^2) \Psi$  to, say, the term  $\tau_0 \partial \Psi / \partial t|_{t_{\text{Zurek}}} = \sqrt{\tau_0 / \tau_Q} \Psi$ , one obtains the characteristic Zurek length which determines the initial length scale of defects,

$$\xi_v = \xi_0 (\tau_Q / \tau_0)^{1/4} , \quad (55)$$

which is the same as in Eq. (3).

We can estimate the lower limit for the characteristic value of the fluctuations  $\Psi_{\text{fluc}} = \Delta_{\text{fluc}} / \Delta_0$ , which serve as a seed for vortex formation. If there are no other sources of fluctuations, caused by external noise for example, the initial seed is provided by thermal fluctuations of the order parameter in the volume  $\xi_v^3$ . The energy of such fluctuations is  $\xi_v^3 \Delta_{\text{fluc}}^2 N_F / E_F$ , where  $E_F \sim k_B T_F$  is the Fermi energy and  $N_F$  the fermionic density of states in normal Fermi liquid. Equating this energy to temperature  $T \approx T_c$  one obtains the magnitude of the thermal fluctuations

$$\frac{|\Psi_{\text{fluc}}|}{|\Psi_{\text{eq}}|} \sim \left(\frac{\tau_0}{\tau_Q}\right)^{1/8} \frac{k_B T_c}{E_F} . \quad (56)$$

The same small parameter  $k_B T_c / E_F \sim a / \xi_0 \sim 10^{-3} - 10^{-2}$  enters here, which is responsible for the extremely narrow temperature region of the critical fluctuations in  $^3\text{He}$  near  $T_c$ . But in our case it only slightly increases the Zurek time by the factor  $\sqrt{\ln[|\Psi_{\text{eq}}| / |\Psi_{\text{fluc}}|]}$  and thus does not influence vortex formation in a homogeneous quench or in an inhomogeneous quench at large velocities of the temperature front.

Clearly there must exist a characteristic velocity  $v_{T_c}$  of the propagating temperature front, which separates the fast and slow regimes, or correspondingly transitions with and without defect formation. The criterion for defect formation is that the Zurek time  $t_{\text{Zurek}} = \sqrt{\tau_Q \tau_0}$  should be shorter than the time  $t_{\text{sw}}$  in which the phase transition front sweeps through the space between the two boundaries. The latter time is  $t_{\text{sw}} = x_0 / v_T$ , where  $x_0$  is the lag – the distance between the temperature front  $T = T_c$  and the region where superfluid coherence starts (order parameter front). If  $t_{\text{Zurek}} < t_{\text{sw}}$ , instabilities have time

to develop. If  $t_{\text{Zurek}} > t_{\text{sw}}$ , both fronts move coherently and the phase is continuous. Let us consider the latter case, with “laminar” motion, and find how the lag  $x_0$  depends on  $v_{\text{T}}$ . From the equation  $t_{\text{Zurek}} = x_0(v_{\text{T}_c})/v_{\text{T}_c}$  we find the criterion for the threshold where laminar motion becomes unstable and defect formation starts.

In steady laminar motion the order parameter depends on  $x - v_{\text{T}}t$ . Introducing a dimensionless variable  $z$  and a dimensionless parameter  $h$ ,

$$z = (x - v_{\text{T}}t)(v_{\text{T}}\tau_{\text{Q}}\xi_0^2)^{-1/3}, \quad h = \left(\frac{v_{\text{T}}\tau_0}{\xi_0}\right)^{4/3} \left(\frac{\tau_{\text{Q}}}{\tau_0}\right)^{1/3}, \quad (57)$$

the linearized TDGL equation becomes

$$\frac{d^2\Psi}{dz^2} + h\frac{d\Psi}{dz} - z\Psi = 0, \quad (58)$$

or

$$\Psi(z) = \text{const} \cdot e^{-hz/2}\chi(z), \quad \frac{d^2\chi}{dz^2} - \left(z + \frac{h^2}{4}\right)\chi = 0. \quad (59)$$

This means that  $\Psi$  is an Airy function,  $\chi(z - z_0)$ , centered at  $z = z_0 = -h^2/4$  and attenuated by the exponential factor  $e^{-hz/2}$ .

When  $h \gg 1$ , it follows from Eq. (59) that  $\Psi(z)$  quickly vanishes as  $z$  increases above  $-h^2/4$ . Thus there is a supercooled region  $-h^2/4 < z < 0$ , where  $T < T_c$ , but the order parameter is not yet formed: the solution is essentially  $\Psi = 0$ . The lag between the order parameter and temperature fronts is  $|z_0| = h^2/4$  or in conventional units

$$x_0 = \frac{1}{4} \frac{v_{\text{T}}^3 \tau_{\text{Q}} \tau_0^2}{\xi_0^2}. \quad (60)$$

Setting  $t_{\text{Zurek}} = x_0(v_{\text{T}_c})/v_{\text{T}_c}$  one can estimate the value for the velocity of the temperature front where laminar propagation becomes unstable:

$$v_{\text{T}_c} \sim \frac{\xi_0}{\tau_0} \left(\frac{\tau_0}{\tau_{\text{Q}}}\right)^{1/4}. \quad (61)$$

This result corresponds to  $h \sim 1$  and is in agreement with that obtained from scaling arguments by Kibble and Volovik (1997). Here an exact numerical value cannot be offered for the threshold where laminar motion ends, but this can in principle be done using the complete TDGL equation (Kopnin and Thuneberg 1999). For the neutron bubble we might take  $v_{\text{T}} \sim R_{\text{b}}/\tau_{\text{Q}}$ , which gives  $v_{\text{T}} \sim 10$  m/s. This value provides also an estimate for the limiting velocity  $v_{\text{T}_c}$ . These considerations suggest that the thermal gradient should be sufficiently steep in the neutron bubble such that defect formation is to be expected.

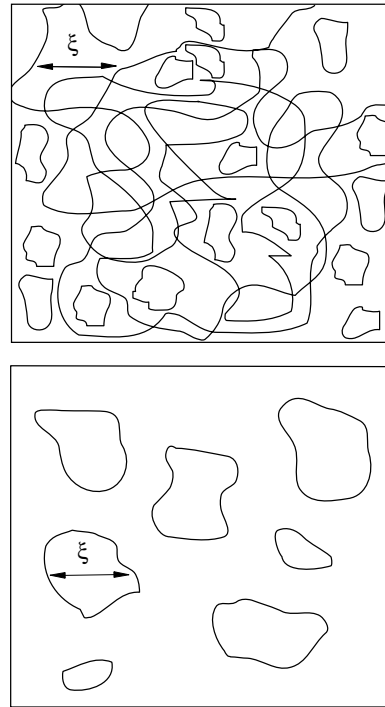


FIG. 32. Normal-to-superfluid transition, when described as a change-over from an infinite to a finite vortex network. (Top) The disordered phase ( $T > T_c$ ) is an infinite network of the defects in the ordered phase – the vacuum of tangled closed loops. The coherence length  $\xi$  is the mean distance between the elements in this network. (Bottom) In the ordered phase ( $T < T_c$ ) the defects also form closed loops, but the coherence length is now the upper limit in the distribution of loop sizes.

## 2.16. Quench of infinite vortex tangle

### 2.16.1. Vorticity on microscopic and macroscopic scales

Onsager (1949) was the first to interpret the  $\lambda$ -transition in liquid  $^4\text{He}$  from the superfluid to the normal state in terms of quantized vortices: When the concentration of the thermally activated quantized vortices reaches the point where they form a connected tangle throughout the liquid (and their line tension vanishes), the liquid goes normal (Fig. 32). This proliferation of vortices to an infinite network destroys superfluidity, since the phase slippage processes caused by the back reaction from the tangle to the superfluid current lead to the decay of this current.

In Ginzburg-Landau theory vortices are identified as lines of zeroes in the scalar complex order parameter  $\Psi = |\Psi|e^{i\Phi}$ , around which the phase winding number  $\nu$  is nonzero. Above the transition, in the symmetric phase, thermal fluctuations of the order parameter give rise to an infinite network of zeroes – to vortices which exist on the microscopic scale but are absent on the macroscopic

scale (Kleinert 1989). This is another way of describing the fact that there is no long range order in the symmetric phase. The properties of such microscopic vortices – topologically nontrivial zeroes – have been followed across the thermodynamic phase transition in numerical investigations (Antunes and Bettencourt 1998; Antunes et al. 1998; Rajantie et al. 1998; Kajantie et al. 1998; Rajantie 1998). The renormalization group description of the phase transition, based on the Ginzburg-Landau free energy functional, also contains the microscopic quantized vortices, but in an implicit form of zeroes (see e.g. Guillou and Zinn-Justin 1980 and Albert 1982).

Some attempts have been made to reformulate the 3-dimensional phase transition in terms of this vortex picture in the renormalization group approach (Williams 1993a,b, 1999; Chattopadhyay et al. 1993), in a manner similar to the 2-dimensional Berezinskii-Kosterlitz-Thouless transition (Nelson and Kosterlitz 1977), i.e. by avoiding consideration of the Ginzburg-Landau free energy functional altogether. It is possible, though it has not been proven, that the Ginzburg-Landau model and the vortex model belong to the same universality class and thus give the same critical exponents for the heat capacity and superfluid density. Both ground and space-based measurements of the critical exponents (Lipa et al. 2003, 1996; Goldner and Ahlers 1992) have generally been consistent with renormalization-group estimations (Strösser and Dohm 2003; Camprostrini et al. 2001; Kleinert and den Bossche 2001).

In an equilibrium phase transition the infinite network disappears below  $T_c$ , but in a non-equilibrium phase transition the tangle of microscopic vortices persists even into the ordered phase, due to critical slowing down. These vortices finally transform to conventional macroscopic vortices, when the latter become well defined. In this language the Kibble-Zurek mechanism corresponds to a quench of the infinite vortex network across the non-equilibrium transition from the normal to the superfluid phase (Yates and Zurek 1998). What is important for us here, is the scaling law for the distribution of vortices. According to numerical simulations (Antunes and Bettencourt 1998; Antunes et al. 1998) and the phenomenological vortex model (Williams 1993a,b, 1999; Chattopadhyay et al. 1993) the scaling exponent  $\delta$ , which characterizes the distribution of vortex loops in Eq. 32), is close to the value  $\delta = 2/(d+2) = 0.4$  obtained using the concept of Flory calculations for self-avoiding polymers. It is different from the value given by the Vachaspati-Vilenkin model for a Brownian-walk network. On the other hand, this model was applied to the Ginzburg region of critical fluctuations in  $^4\text{He}$ , which might not be valid for  $^3\text{He}$ .

## 2.16.2. Scaling in equilibrium phase transitions

Important differences exist between the phase transitions in the  $^4\text{He}$  and  $^3\text{He}$  liquids. These also are involved in a number of other phenomena. Let us therefore recall some of these differences. The temperature region of the critical fluctuations, where the simple Ginzburg-Landau theory does not work and one must introduce the thermal renormalization of the Ginzburg-Landau functional, can be derived from the following simplified considerations. Let us estimate the length  $L_T$  of the thermal vortex loop, i.e. a loop whose energy is comparable to temperature:

$$\rho_s(T) \frac{\kappa^2}{4\pi} L_T \ln \left( \frac{L_T}{\xi(T)} \right) = k_B T \approx k_B T_c . \quad (62)$$

In the broken symmetry phase far below  $T_c$ , this length is less than the coherence length  $\xi(T)$ , which means that there are no real vortices with the energy of order  $k_B T$ , and real vortices with higher energy are exponentially suppressed. When the temperature increases, one approaches the point at which the length  $L_T$  becomes comparable to the coherence length  $\xi$ . This is the Ginzburg temperature  $T_{\text{Gi}}$ , determined by the condition  $L_T(T = T_{\text{Gi}}) \sim \xi(T = T_{\text{Gi}})$ :

$$\rho_s(T_{\text{Gi}}) \xi(T_{\text{Gi}}) \sim \frac{k_B T_c}{\kappa^2} . \quad (63)$$

or

$$\left( 1 - \frac{T_{\text{Gi}}}{T_c} \right) \sim \left( \frac{k_B T_c}{\rho \xi_0 \kappa^2} \right)^2 \sim \left( \frac{T_c}{T_F} \right)^4 . \quad (64)$$

Here as before  $T_F \sim \hbar^2/ma^2 \sim 1\text{K}$  is the degeneracy temperature of the quantum fluid, with  $a$  being the inter-atomic spacing. The region of critical fluctuations – the Ginzburg region  $T_{\text{Gi}} < T < T_c$  – is broad for  $^4\text{He}$ , where  $T_c \sim T_F$ , and extremely small for  $^3\text{He}$ , where  $T_c < 10^{-2} T_F$ .

In the region of Ginzburg fluctuations the scaling exponents for the thermodynamic quantities, such as  $\xi(T)$  and  $\rho_s(T)$ , are different from those in the Ginzburg-Landau region,  $T_c - T_{\text{Gi}} < T_c - T \ll T_c$ :

$$\frac{\xi(T)}{\xi_0} \sim \left( 1 - \frac{T}{T_c} \right)^{-\frac{1}{2}} , \quad T_c - T_{\text{Gi}} < T_c - T \ll T_c , \quad (65)$$

$$\frac{\xi(T)}{\xi_0} \sim \left( 1 - \frac{T_{\text{Gi}}}{T_c} \right)^{\nu - \frac{1}{2}} \left( 1 - \frac{T}{T_c} \right)^{-\nu} , \quad T_{\text{Gi}} < T < T_c , \quad (66)$$

$$\frac{\rho_s(T)}{\rho} \sim \left( 1 - \frac{T}{T_c} \right) , \quad T_c - T_{\text{Gi}} < T_c - T \ll T_c , \quad (67)$$

$$\frac{\rho_s(T)}{\rho} \sim \left( 1 - \frac{T_{\text{Gi}}}{T_c} \right)^{1-\zeta} \left( 1 - \frac{T}{T_c} \right)^{\zeta} , \quad T_{\text{Gi}} < T < T_c . \quad (68)$$

There are two relations, the scaling hypotheses, which connect the critical exponents for  $\xi(T)$  and  $\rho_s(T)$  in the

Ginzburg region, with the exponent of the heat capacity. In the Ginzburg region  $T_{\text{Gi}} < T < T_c$ , the coherence length is determined by thermal fluctuations, or which is the same thing, by thermal vortices. This gives for the relation between the coherence length  $\xi(T)$  and superfluid density  $\rho_s(T)$  in the Ginzburg region:

$$\rho_s(T)\xi(T) \sim \frac{k_B T_c}{\kappa^2} \sim \rho a \left( \frac{T_c}{T_F} \right), \quad T_{\text{Gi}} < T < T_c. \quad (69)$$

This equation gives the Josephson scaling hypothesis:  $\nu = \zeta$ .

Another relation between these exponents comes from a consideration of the free energy, which has the same scaling law as the kinetic energy of superflow:

$$F(T) \sim \left(1 - \frac{T}{T_c}\right)^{2-\alpha} \sim \rho_s v_s^2 \sim \frac{\rho_s(T)}{\xi^2(T)} \sim \frac{\rho}{\xi_0^2} \left(1 - \frac{T}{T_c}\right)^{\zeta+2\nu}. \quad (70)$$

Here  $\alpha$  is the the critical exponent for the heat capacity in the critical region,  $C(T) = -T\partial_T^2 F \sim (1 - T/T_c)^{-\alpha}$ . Eqs. (69) and (70) give  $\nu = \zeta = (2 - \alpha)/3$ .

### 2.16.3. Non-equilibrium phase transitions

The formation of vortices during a rapid transition into the broken-symmetry phase is the subject of dynamic scaling and a poorly known area in the field of critical phenomena. Dynamic scaling is characterized by an additional set of critical exponents, which depend not only on the symmetry and topology of the order parameter, but also on the interaction of the order parameter with the different dynamic modes of the normal liquid. The question first posed by Zurek was the following: What is the initial density  $\xi_v$  of macroscopic vortices at the moment when they become well defined? According to the general scaling hypothesis one has

$$\xi_v \sim \xi_0 (\omega \tau_0)^{-\lambda} \text{ and } \omega = \frac{1}{\tau_Q}, \quad (71)$$

where  $\omega$  is the characteristic frequency of the dynamic process.

In the time-dependent Ginzburg-Landau model (Eq. (47)) and also in its extension based on the renormalization group approach, the exponent  $\lambda$  is determined by the static exponents and by the exponent for the relaxation time  $\tau = \tau_0(1 - T/T_c)^{-\mu}$ :

$$\lambda = \frac{\nu}{1 + \mu}. \quad (72)$$

This follows from the following consideration. When we approach the critical temperature from the normal phase, at some moment  $t_{\text{Zurek}}$  the relaxation time  $\tau(t)$  becomes

comparable to the time  $t$  which is left until the transition takes place. At this moment

$$t_{\text{Zurek}} = \tau_0 \left( \frac{\tau_Q}{\tau_0} \right)^{\mu/(1+\mu)}, \quad (73)$$

the vortex network is frozen out. After the transition it becomes “unfrozen” when  $\tau(t)$  again becomes smaller than  $t$ , the time after passing the transition. The initial distance between the vortices is determined as the coherence length  $\xi = \xi_0(t/\tau_Q)^{-\nu}$  at  $t = t_{\text{Zurek}}$ , which gives Eq. (71) with  $\lambda$  as in Eq. (72). For the conventional time-dependent Ginzburg-Landau model in Eq. (47) one has  $\mu = 1$ ,  $\nu = 1/2$ , and thus  $\lambda = 1/4$ . In the Ginzburg regime, if one assumes that  $\mu$  remains the same, while  $\nu \approx 2/3$ , one obtains  $\lambda \approx 1/3$ .

In numerical simulation of a quench in the time-dependent Ginzburg-Landau model, the main problem becomes how to resolve between the microscopic vortices (ie. the zeroes in the order parameter) and real macroscopic vortices. This requires some coarse-graining procedure, which is not well established. Also speculations exist (Rivers 2000) that if the quench is limited to within the region of the Ginzburg fluctuations, then the network of microscopic vortices might effectively screen out the real macroscopic vortices, so that the density of the real vortices after the quench is essentially less than its Zurek estimate. This could explain the negative result of the recent pressure-quench experiments in liquid  $^4\text{He}$  (Dodd et al. 1998), where the final state after the decompression was well within the region of critical fluctuations.

To summarize, we note that vortices play an important role, not only in the ordered state, but also in the physics of the broken symmetry phase transitions. The proliferation of vortex loops with infinite size can be interpreted to destroy the superfluid long range order above the phase transition. In a non-equilibrium phase transition from the symmetric normal phase to the superfluid state, the infinite vortex cluster from the normal state survives after the rapid quench and becomes the source for the remanent vorticity in the superfluid state. This is an alternative picture in which one may understand the formation of vortices in a rapid non-equilibrium transition.

## 2.17. Implications of the quench-cooled experiments

### 2.17.1. Topological-defect formation

It is not obvious that a phenomenological model like the KZ mechanism, which is based on scaling arguments, should work at all: It describes a time-dependent phase transition in terms of quantities characterizing the equilibrium properties of the system. Numerical calculations

on simple quantum systems, where one studies the fluctuations in the amplitude of the system wave function while it is quenched below a second order phase transition, have provided much evidence for the KZ model and appear to agree with its qualitative features. Most attempts of experimental verification suffer from shortcomings. Measurements on superfluid  $^3\text{He}$  are the first to test the KZ model more quantitatively. In this case the experimental deviations from the ideal KZ setup include the presence of a strict boundary condition and a strong thermal gradient. At present time we can conclude that the experiments and the model are in reasonable harmony, assuming that open questions from Sec. 2.14 can be answered satisfactorily, as seems likely.

However, even good agreement leaves us with an interesting question: What is the microscopic basis for the applicability of the KZ mechanism to such experiments? A rapid quench through the superfluid transition is more amenable to microscopic analysis in the case of liquid  $^3\text{He}$  than in most other systems, since the freeze out of order-parameter domains can be demonstrated with physically acceptable calculations. The consequences from this are exciting and the prospects for a better understanding of non-equilibrium phase transitions look promising. Although detailed agreement has not yet been reached between experimental and theoretical work, nevertheless the effort by Aranson et al. (1999, 2001) illustrates that many aspects of the neutron absorption event in  $^3\text{He-B}$  can be treated in realistic ways.

Are there implications from such work to cosmological large-scale structure formation? The combined existing evidence from condensed matter experiments supports the KZ mechanism at high transition velocities. This says that the KZ mechanism is an important process in rapid non-equilibrium phase transitions and cannot be neglected. Whether it was effective in the Early Universe and led to the formation of large-scale structure, rather than some other phenomenon like inflationary expansion, is a separate question. It can only be answered by measurements and investigations on the cosmological scale which directly search for the evidence on topological defect formation or its exclusion. The fact that no direct traces from topological defects have been identified, excepting the large-scale structure itself, is not yet sufficient proof that they can be discarded altogether. As measurements of the moving first-order AB interface in  $^3\text{He}$  superfluids show, the interactions of the defects with the phase front and across it are complicated and no simple general rule exist on the final outcome.

### 2.17.2. Phase transitions

As discussed in Secs. 2.10.1 and 2.10.2, the KZ mechanism provides an attractive explanation for the radia-

tion induced first order transition from supercooled  $^3\text{He-A}$  to  $^3\text{He-B}$ . The nucleation of competing phases, with different symmetries and local minima of the energy functional, has been discussed both in superfluid  $^3\text{He}$  (Volovik 2003) and in the cosmological context (Linde 1990).

Above the critical phase-transition temperature  $T_c$ , liquid  $^3\text{He}$  is in its symmetric phase: it has all the symmetries allowed in non-relativistic condensed matter. The continuous symmetries, whose breaking are relevant for the topological classification of the defects in the non-symmetric phases of  $^3\text{He}$ , form the symmetry group

$$\mathbf{G} = SO(3)_{\mathbf{L}} \times SO(3)_{\mathbf{S}} \times U(1)_{\mathbf{N}} . \quad (74)$$

Here  $SO(3)_{\mathbf{L}}$  is the group of solid rotations of the coordinate space. The spin rotations of the group  $SO(3)_{\mathbf{S}}$  may be considered as a separate symmetry operation if one neglects the dipolar spin-orbit interaction. The magnetic dipole interaction between the nuclear spins is tiny in comparison with the energies characterizing the superfluid transition. The group  $U(1)_{\mathbf{N}}$  is the *global* symmetry group of gauge transformations, which stems from the conservation of the particle number  $N$  for the  $^3\text{He}$  atoms in their ground states.  $U(1)$  is an exact symmetry if one neglects extremely rare processes of excitations and ionization of the  $^3\text{He}$  atoms, as well as the transformation of  $^3\text{He}$  nuclei, in neutron radiation.

Below  $T_c$  the “unified GUT symmetry”  $SO(3)_{\mathbf{L}} \times SO(3)_{\mathbf{S}} \times U(1)_{\mathbf{N}}$  can be broken to the  $U(1) \times U(1)$  symmetry of the A phase or to the  $SO(3)$  symmetry of the B-phase, with a small energy difference between these two states, but separated by an extremely high energy barrier ( $\sim 10^6 k_B T$ ) from each other. In this situation a thermally activated A $\rightarrow$ B transition becomes impossible. For the radiation-induced A $\rightarrow$ B transition two solutions have been suggested: 1) the baked Alaska configuration where the transition takes place inside a cool bubble isolated by a warm shell from the surrounding A-phase bath (Leggett 1984), and 2) the KZ mechanism, first proposed by Volovik (1996) and then put on quantitative ground by Bunkov and Timofeevskaya (1998a,b).

This situation can be compared to that in the early Universe. It is believed that the  $SU(3) \times SU(2) \times U(1)$  symmetries of the strong, weak, and electromagnetic interactions (respectively) were united at high energies (or at high temperatures). The underlying Grand Unification (GUT) symmetry ( $SU(5)$ ,  $SO(10)$ , or a larger group) was broken at an early stage during the cooling of the Universe. Even the simplest GUT symmetry  $SU(5)$  can be broken in different ways: into the phase  $SU(3) \times SU(2) \times U(1)$ , which is our world, and into  $SU(4) \times U(1)$ , which apparently corresponds to a higher energy state. In supersymmetric models both phases represent local minima of almost equal depth, but are separated from each other by a high energy barrier.

In the cosmological scenario, after the symmetry break

of the  $SU(5)$  GUT state, both new phases are created simultaneously with domain walls between them. The calculated probability for the creation of our world — the  $SU(3) \times SU(2) \times U(1)$  state — appears to be smaller than that of the false vacuum state of  $SU(4) \times U(1)$  symmetry at higher energy. Thus initially the state corresponding to our world appears to have occupied only a fraction of the total volume. Later bubbles of this energetically preferred state grew at the expense of the false vacuum state and finally completely expelled it. However, before that interfaces between the two states were created in those places where blobs of the two phases met. Such an interface is an additional topologically stable defect, which is formed in the transition process and interacts with other topological defects.

### 3. VORTEX DYNAMICS AND QUANTUM FIELD THEORY ANALOGUES

From the phenomenological point of view, vortex dynamics in  $^3\text{He-B}$  is similar to  $^4\text{He-II}$ , but the properties which govern the dynamics arise from the quite different microscopics of the p-wave Cooper-paired fermion superfluid. These properties turn out to have interesting analogies with various problems in quantum field theory (Volovik 2003). It is these connections which are in the focus of the discussion in this section.

The fundamental starting point is the notion that the bosonic and fermionic excitations in superfluid  $^3\text{He}$  are in many respects similar to the excitations of the energetic physical vacuum of elementary particle physics – the modern ether. This similarity allows us to model, with concepts borrowed from  $^3\text{He}$  physics, the interactions of elementary particles with the evolving strings and domain walls, which are formed in a rapid phase transition, for instance. Such processes become important after defect formation in the initial quench and give rise to the cosmological consequences which we are measuring today.

The quantum physical vacuum – the former empty space – is in reality a richly structured and asymmetric medium. Because the new quantum ether is such a complicated material with many degrees of freedom, one can learn to analyze it by studying other materials, *ie.* condensed matter (Wilczek 1998). Fermi superfluids, especially  $^3\text{He-A}$ , are the best examples, which provide opportunities for such modelling. The most pronounced property of  $^3\text{He-A}$  is that, in addition to the numerous bosonic fields (collective modes of the order parameter which play the part of gauge fields in electromagnetic, weak, and strong interactions) it contains gapless fermionic quasiparticles, which are similar to the elementary excitations of the quantum physical vacuum (leptons and quarks).

It is important that the quantum physical vacuum belongs to the same class of fermionic condensed matter as  $^3\text{He-A}$ : both contain topologically stable nodes in the energy spectrum of the fermionic excitations. As a result both of these fermionic systems display, for example, the gravitational and gauge fields as collective bosonic modes. Other fermionic systems belong either to a class, which is characterized by Fermi surfaces (such as normal metals and the normal  $^3\text{He}$  liquid), or to a class with a gap in the fermionic spectrum (such as conventional superconductors and  $^3\text{He-B}$ ). High-temperature superconductors seem to belong to a marginal class, with topologically unstable lines of gap nodes. Thus  $^3\text{He-A}$  (together with  $^3\text{He-A}_1$ ) is the condensed matter system in which the properties of the physical vacuum can, in principle, be probed with laboratory experiments.

#### 3.1. Three topological forces acting on a vortex and their analogues

Here we consider the experimentally observed forces which act on a moving vortex in superfluid  $^3\text{He}$ . As listed in Sec. 2.14.3, there are 3 different topological contributions to the total force. The more familiar Magnus force arises when the vortex moves with respect to the superfluid vacuum. In the case of a relativistic cosmic string this force is absent, since the corresponding superfluid density of the quantum physical vacuum is zero. However, the analog of this force appears if the cosmic string moves in a uniform background charge density (Davis and Shellard 1989; Lee 1994). The other two forces of topological origin – the Iordanskii force and spectral flow force – also have analogues in the case of a cosmic string (Volovik and Vachaspati 1996; Volovik 1998; Sonin 1997; Wexler 1997; Shelankov 1998a,b).

We start with the Iordanskii force (Iordanskii 1964, 1965; Sonin 1975), which arises when the vortex moves with respect to the heat bath represented by the normal component of the liquid, or the quasiparticle excitations. The latter corresponds to the matter of particle physics. The interaction of quasiparticles with the velocity field of the vortex resembles the interaction of matter with the gravitational field induced by such a cosmic string, which has an angular momentum, – the so-called spinning cosmic string (Mazur 1986). The spinning string induces a peculiar space-time metric, which leads to a difference in the time which a particle needs to orbit around the string at same speed, but in opposite directions (Harari and Polychronakos 1988). This gives rise to the quantum gravitational Aharonov-Bohm effect (Mazur 1986, 1987, 1996). We discuss how the same effect leads to an asymmetry in the scattering of particles from the spinning string and to the Iordanskii lifting force which acts on the spinning string or on the moving vortex.

The spectral flow force, which also arises when the vortex moves with respect to the heat bath, is a direct consequence from the chiral anomaly effect. The latter violates the conservation of fermionic charge. The anomalous generation by the moving vortex of fermionic charge or momentum (called “momentogenesis”) leads to a net force acting on the vortex. The existence of this force was experimentally confirmed in the  $^3\text{He}$  measurements of Bevan et al. (1997b). This phenomenon is based on the same physics as the anomalous generation of matter in particle physics and bears directly on the cosmological problem of baryonic asymmetry of our Universe: the question why the Universe contains so much more matter than antimatter (“baryogenesis”).

The experimental observation of the opposite effect to momentogenesis has been reported by Krusius et al. (1998): the conversion of quasiparticle momentum into a non-trivial order parameter configuration or “texture”. The corresponding process in a cosmological setting would be the creation of a primordial magnetic field due to changes in the matter content. Processes, in which magnetic fields are generated, are very relevant to cosmology since magnetic fields are ubiquitous now in the Universe. Our Milky Way and other galaxies, as well as clusters of galaxies, are observed to have a magnetic field whose generation is still not understood. One possible mechanism is that a seed field was amplified by the complex motions associated with galaxies and clusters of galaxies. The seed field itself is usually assumed to be of cosmological origin.

It has been noted that the two problems of cosmological genesis – baryo- and magnetogenesis – may be related to each other (Roberge 1989; Vachaspati and Field 1994, 1995; Vachaspati 1994). More recently an even stronger reason for a possible connection was proposed (Joyce and Shaposhnikov 1997; Giovannini and Shaposhnikov 1997). In this same way their analogs are related in  $^3\text{He}$ , where the order parameter texture is the analog of magnetic field, while the normal component of the superfluid represents the matter: the moving vortex texture leads to an anomalous production of quasiparticles, while an excess of the quasiparticle momentum – the net quasiparticle current of the normal component – leads to the formation of textures. This mapping of cosmology to condensed matter is not simply a picture: the corresponding effects in the two systems are described by the same equations in the low-energy regime, by quantum field theory and the axial anomaly.

## 3.2. Iordanskii force

### 3.2.1. Superfluid vortex vs spinning cosmic string

To clarify the analogy between the Iordanskii force and the Aharonov-Bohm effect, let us consider the simplest

case of phonons propagating in the velocity field of the quantized vortex in the Bose superfluid  $^4\text{He-II}$ . According to the Landau theory of superfluidity, the energy of a quasiparticle moving in the superfluidity velocity field  $\mathbf{v}_s(\mathbf{r})$  is Doppler shifted:  $E(\mathbf{p}) = \epsilon(\mathbf{p}) + \mathbf{p} \cdot \mathbf{v}_s(\mathbf{r})$ . In the case of the phonons with the spectrum  $\epsilon(\mathbf{p}) = cp$ , where  $c$  is the sound velocity, the energy-momentum relation is thus

$$(E - \mathbf{p} \cdot \mathbf{v}_s(\mathbf{r}))^2 = c^2 p^2. \quad (75)$$

Eq. (75) can be written in the general Lorentzian form with  $p_\mu = (-E, \mathbf{p})$ :

$$g^{\mu\nu} p_\mu p_\nu = 0 \quad (76)$$

where the metric is

$$g^{00} = 1, \quad g^{0i} = -v_s^i, \quad g^{ik} = -c^2 \delta^{ik} + v_s^i v_s^k. \quad (77)$$

We use the convention to denote indices in the 0–3 range by Greek letters and indices in the 1–3 range by Latin letters. Thus the dynamics of phonons in the presence of the velocity field is the same as the dynamics of photons in the gravity field (Unruh 1976): both are described by the light-cone equation  $ds = 0$ . The interval  $ds$  for phonons is given by the inverse metric  $g_{\mu\nu}$  which determines the geometry of the effective space:

$$ds^2 = g_{\mu\nu} dx^\mu dx^\nu, \quad (78)$$

where  $x = (t, \mathbf{r})$  are physical (Galilean) coordinates in the laboratory frame.

A similar relativistic equation holds for the fermionic quasiparticles in superfluid  $^3\text{He-A}$  in the linear approximation close to the gap nodes. In general, i.e. far from the gap nodes, the spectrum of quasiparticle in  $^3\text{He-A}$  is not relativistic:

$$\epsilon^2(\mathbf{p}) = v_F^2 (p - p_F)^2 + \frac{\Delta_A^2}{p_F^2} (\hat{\mathbf{l}} \times \mathbf{p})^2. \quad (79)$$

Here  $v_F(p - p_F)$  is the quasiparticle energy in the normal Fermi liquid state above the transition, with  $p_F$  the Fermi momentum and  $v_F = p_F/m^*$ ;  $m^*$  is the effective mass, which is of order of the mass  $m_3$  of the  $^3\text{He}$  atom;  $\Delta_A$  is the so-called gap amplitude and the unit vector  $\hat{\mathbf{l}}$  points in the direction of the gap nodes.

The energy in Eq. (79) is zero at two points  $\mathbf{p} = e\mathbf{A}$  with  $\mathbf{A} = p_F \hat{\mathbf{l}}$  and  $e = \pm 1$ . Close to the two zeroes of the energy spectrum one can expand the equation  $(E - \mathbf{p} \cdot \mathbf{v}_s(\mathbf{r}))^2 = \epsilon^2(\mathbf{p})$  in  $\mathbf{p} - e\mathbf{A}$  and write it in a form similar to the propagation equation for a massless relativistic particle in curved spacetime in the presence of an electromagnetic vector potential:

$$g^{\mu\nu} (p_\mu - eA_\mu)(p_\nu - eA_\nu) = 0. \quad (80)$$

Here  $A_0 = p_F(\hat{\mathbf{l}} \cdot \mathbf{v}_s)$  and the metric is anisotropic with the anisotropy axis along the  $\hat{\mathbf{l}}$ -vector:



$$\begin{aligned}
g^{00} &= 1, & g^{0i} &= -v_s^i, \\
g^{ik} &= -c_\perp^2 (\delta^{ik} - \hat{l}^i \hat{l}^k) - c_\parallel^2 \hat{l}^i \hat{l}^k + v_s^i v_s^k, \\
c_\parallel &= v_F, & c_\perp &= \Delta_A / v_F.
\end{aligned} \tag{81}$$

The quantities  $c_\parallel$  and  $c_\perp$  correspond to the speeds of light propagating along or transverse to  $\hat{\mathbf{l}}$ .

For simplicity, let us turn back to the case of phonons and vortices in  $^4\text{He-II}$  which is described by Eqs. (76), (77). If the velocity field is generated by one vortex with  $\nu$  quanta of circulation,  $\mathbf{v}_s = \nu \kappa \hat{\phi} / 2\pi r$ , then the interval (78) in the effective space, where the phonon is propagating along geodesic curves, becomes:

$$\begin{aligned}
ds^2 &= \left(1 - \frac{v_s^2}{c^2}\right) \left(dt + \frac{\nu \kappa d\phi}{2\pi(c^2 - v_s^2)}\right)^2 \\
&\quad - \frac{dr^2}{c^2} - \frac{dz^2}{c^2} - \frac{r^2 d\phi^2}{c^2 - v_s^2}. \tag{82}
\end{aligned}$$

The origin of the Iordanskii force lies in the scattering of quasiparticles for small angles, so large distances from the vortex core are important. Far from the vortex  $v_s^2/c^2$  is small and can be neglected, and one has

$$ds^2 = \left(dt + \frac{d\phi}{\omega}\right)^2 - \frac{1}{c^2}(dz^2 + dr^2 + r^2 d\phi^2), \quad \omega = \frac{2\pi c^2}{\nu \kappa}, \tag{83}$$

The connection between time and the azimuthal angle  $\phi$  in the interval suggests that there is a characteristic angular velocity  $\omega$ . A similar metric with rotation was obtained for the so-called spinning cosmic string in 3 + 1 space-time, which has the rotational angular momentum  $J$  concentrated in the string core, and for the spinning particle in the 2+1 gravity (Mazur 1986, 1996; Staruszkiewicz 1963; Deser et al. 1984):

$$ds^2 = \left(dt + \frac{d\phi}{\omega}\right)^2 - \frac{1}{c^2}(dz^2 + dr^2 + r^2 d\phi^2), \quad \omega = \frac{1}{4JG} \tag{84}$$

where  $G$  is the gravitational constant. This gives the following correspondence between the circulation  $\nu \kappa$  around the vortex and the angular momentum  $J$  of the spinning string

$$\kappa \nu = 8\pi JG. \tag{85}$$

Although we here consider the analogy between the spinning string and vortices in  $^4\text{He-II}$ , there exists a general statement that vortices in any superfluid have the properties of spinning cosmic strings (Davis and Sheldard 1989). In particular, the spinning string generates a density of angular momentum in the vacuum outside the string (Jensen and Kuvcera 1993). The density of

angular momentum in the superfluid vacuum outside the vortex is also nonzero and equals at  $T = 0$

$$\mathbf{r} \times \rho \mathbf{v}_s = \hbar \nu n_B \hat{\mathbf{z}}, \tag{86}$$

where  $n_B$  is the density of elementary bosons in the superfluid vacuum: the density  $\rho/m_4$  of  $^4\text{He}$  atoms in superfluid  $^4\text{He-II}$  or the density  $\rho/2m_3$  of Cooper pairs in superfluid  $^3\text{He}$ .

### 3.2.2. Gravitational Aharonov-Bohm effect

For the spinning string the gravitational Aharonov-Bohm effect is a peculiar topological phenomenon (Mazur 1986) which can be modeled in condensed matter. On the classical level the propagation of particles is described by the relativistic equation  $ds^2 = 0$ . Outside the string the space metric, which enters the interval  $ds$ , is flat, Eq. (84). But there is a difference in the travel time for particles along closed paths around the spinning string in opposite directions. As can be seen from Eq. (84), this time difference is (Harari and Polychronakos 1988)

$$2\tau = \frac{4\pi}{\omega}. \tag{87}$$

At large distances from the core the same equation is approximately valid due to the equivalence of the metrics in Eqs. (83) and (84). The asymmetry between the particles orbiting in different directions around the vortex implies that, in addition to the symmetric part of the cross section,

$$\sigma_\parallel = \int_0^{2\pi} d\theta (1 - \cos \theta) |a(\theta)|^2, \tag{88}$$

where  $a(\theta)$  is a scattering amplitude, there should be an asymmetric part of the scattering cross section,

$$\sigma_\perp = \int_0^{2\pi} d\theta \sin \theta |a(\theta)|^2. \tag{89}$$

The latter is the origin of the Iordanskii force acting on the vortex in the presence of a net momentum from the quasiparticles. Another consequence of Eqs. (83), (84) is displayed on the quantum level: the connection between the time variable  $t$  and the angular variable  $\phi$  in Eqs. (83), (84) implies that the scattering cross sections of phonons (photons) from the vortex (string) should be periodic functions of energy, with the period equal to  $\hbar\omega$ .

Calculations which allow us to find both symmetric and asymmetric contributions to the scattering of quasiparticles in the velocity field of the vortex have been performed by Sonin (1997) for phonons and rotons in  $^4\text{He-II}$  and by Cleary (1968) for the Bogoliubov-Nambu quasiparticles in conventional superconductors. In the case of phonons the propagation is described by the Lorentzian

equation for the scalar field  $\Phi$ :  $g^{\mu\nu}\partial_\mu\partial_\nu\Phi = 0$ , with  $g^{\mu\nu}$  from Eq. (77). We are interested in large distances from the vortex core. Thus the quadratic terms  $\mathbf{v}_s^2/c^2$  can be neglected and the equation can be rewritten as (Sonin 1997)

$$E^2\Phi - c^2\left(-i\nabla + \frac{E}{c}\mathbf{v}_s(\mathbf{r})\right)^2\Phi = 0. \quad (90)$$

This equation maps the problem under discussion to the Aharonov-Bohm (AB) problem for the magnetic flux tube (Aharonov and Bohm 1959) with the effective vector potential  $\mathbf{A} = \mathbf{v}_s$ , where the electric charge  $e$  is substituted by the mass  $E/c^2$  of the particle (Mazur 1987; Jensen and Kuvcera 1993; Gal'tsov and Letelier 1993). Actually  $\mathbf{v}_s$  plays the part of the vector potential of the so called gravimagnetic field (Volovik 2003). Because of the mapping between the electric charge and the mass of the particle, one obtains the AB expression (Aharonov and Bohm 1959) for the symmetric differential cross section

$$\frac{d\sigma_{\parallel}}{d\theta} = \frac{\hbar c}{2\pi E \sin^2(\theta/2)} \sin^2 \frac{\pi E}{\hbar\omega}. \quad (91)$$

This expression was obtained for the scattering of particles with energy  $E$  in the background of a spinning string with zero mass (Mazur 1987, 1996) and represented the gravitational AB effect. Note the singularity at  $\theta \rightarrow 0$ .

Returning back to vortices, one finds that the analogue with the spinning string is not exact. In more accurate calculations one should take into account that as distinct from the charged particles in the AB effect, the current in the case of phonons is not gauge invariant. As a result the scattering of the phonon with momentum  $p$  and energy  $E$  from the vortex is somewhat different (Sonin 1997):

$$\frac{d\sigma_{\parallel}}{d\theta} = \frac{\hbar c}{2\pi E} \cot^2 \frac{\theta}{2} \sin^2 \frac{\pi E}{\hbar\omega}. \quad (92)$$

The algebraic difference between the AB results in Eqs. (91) and (92) is  $(\hbar c/2\pi E) \sin^2(\pi E/\omega)$ , which is independent of the scattering angle  $\theta$  and thus is not important for the singularity at small scattering angles, which is present in Eq. (92) as well. For small  $E$  the result in Eq. (92) was obtained by Fetter (1964). The generalization of the Fetter result for quasiparticles with arbitrary spectrum  $\epsilon(\mathbf{p})$  (rotons in  $^4\text{He-II}$  and the Bogoliubov-Nambu fermions in superconductors) was recently suggested by Demircan et al. (1995): In our notations it is  $(\nu\kappa^2 p/8\pi v_G^2) \cot^2(\theta/2)$ , where  $v_G = d\epsilon/dp$  is the group velocity of a quasiparticle.

### 3.2.3. Asymmetric cross section of scattering from a vortex

The Lorentz force, which acts on the flux tube in the presence of an electric current, has its counterpart – the

Iordanskii force, which acts on the vortex in the presence of a mass current of the normal component. The Lorentz-type Iordanskii force comes from the asymmetric contribution to the cross section (Sonin 1997; Shelankov 1998a,b), which has the same origin as the singularity at small angles in the symmetric cross section and leads to a non-zero transverse cross section.

For the phonons in  $^4\text{He-II}$  with the spectrum  $E(\mathbf{p}) = cp$  the transverse cross section is (Sonin 1997)

$$\sigma_{\perp} = \frac{\hbar}{p} \sin \frac{2\pi E}{\hbar\omega}. \quad (93)$$

At low  $E \ll \hbar\omega$  the result becomes classical:  $\sigma_{\perp} = 2\pi c/\omega$  does not contain the Planck constant  $\hbar$ . This means that in the low energy limit the asymmetric cross section can be obtained from the classical theory of scattering. In this case it can be generalized for an arbitrary spectrum  $E(\mathbf{p})$  of scattering particles (Sonin 1997). Let us consider a particle with the spectrum  $E(\mathbf{p})$  moving in the background of the velocity field  $\mathbf{v}_s(\mathbf{r})$  around the vortex. The velocity field modifies the particle energy due to the Doppler shift,  $E(\mathbf{p}, \mathbf{r}) = E(\mathbf{p}) + \mathbf{p} \cdot \mathbf{v}_s(\mathbf{r})$ . Far from the vortex, where the circulating velocity is small, the trajectory of the quasiparticle is almost a straight line parallel to, say, the axis  $y$ , with the distance from the vortex line being the impact parameter  $x$ . It moves along this line with almost constant momentum  $p_y \approx p$  and almost constant group velocity  $dy/dt = v_G = d\epsilon/dp$ . The change in transverse momentum during this motion is determined by the Hamiltonian equation  $dp_x/dt = -\partial E/\partial x = -p_y \partial v_{sy}/\partial x$ , or  $dp_x/dy = -(p/v_G) \partial v_{sy}/\partial x$ . The transverse cross section is obtained by integration of  $\Delta p_x/p$  over the impact parameter  $x$ :

$$\sigma_{\perp} = \int_{-\infty}^{+\infty} \frac{dx}{v_G} \int_{-\infty}^{+\infty} dy \frac{\partial v_{sy}}{\partial x} = \frac{\nu\kappa}{v_G}. \quad (94)$$

This result is purely classical: Planck's constant  $\hbar$  drops out (it enters only via the quantized circulation  $\nu\kappa$  which characterizes the vortex).

### 3.2.4. Iordanskii force: quantized vortex and spinning string

The asymmetric part of scattering, which describes the momentum transfer in the transverse direction, after integration over the distribution of excitations gives rise to the transverse force acting on the vortex if the vortex moves with respect to the normal component. This is the Iordanskii force:

$$\begin{aligned} \mathbf{f}_{\text{Iordanskii}} &= \int \frac{d^3p}{(2\pi)^3} \sigma_{\perp}(p) v_G n(\mathbf{p}) \mathbf{p} \times \hat{\mathbf{z}} = \\ &= -\nu\kappa \hat{\mathbf{z}} \times \int \frac{d^3p}{(2\pi)^3} n(\mathbf{p}) \mathbf{p} = \nu\kappa \mathbf{P}_n \times \hat{\mathbf{z}}. \end{aligned} \quad (95)$$

It is proportional to the density of mass current  $\mathbf{P}_n$  carried by excitations (matter). Of all the parameters describing the vortex, it depends only on the circulation  $\nu\kappa$ . This confirms the topological origin of this force. In the case of the equilibrium distribution of quasiparticles one has  $\mathbf{P}_n = \rho_n \mathbf{v}_n$ , where  $\rho_n$  and  $\mathbf{v}_n$  are the density and velocity of the normal component of the liquid. Thus one obtains Eq. (36). To avoid the conventional Magnus force in this derivation, we assumed that the asymptotic velocity of the superfluid component of the liquid is zero in the frame of the vortex.

Eq. (95) was obtained using the asymptotic behavior of the flow field  $\mathbf{v}_s$ , which induces the same effective metric (83) as the metric around the spinning string (84). We can thus apply this result directly to the spinning string. The asymmetric scattering cross-section of relativistic particles from the spinning string is given by Eq. (93). This means that in the presence of momentum from matter the spinning cosmic string experiences a lifting force, which corresponds to the Iordanskii force in superfluids. This force can be obtained from a relativistic generalization of Eq. (95). The momentum density  $\mathbf{P}_n$  of quasiparticles should be substituted by the component  $T_0^i$  of the energy-momentum tensor. As a result, for 2+1 space-time and for low energy  $E$ , which corresponds to low temperatures  $T$  for matter, the Iordanskii force on a spinning string moving with respect to the matter is

$$f_{\text{Iordanskii}}^\alpha = 8\pi J G \varepsilon^{\alpha\beta\gamma} u_\beta u_\mu T_\gamma^\mu. \quad (96)$$

Here  $u_\alpha$  is the 3-velocity of the string and  $T_\gamma^\mu$  is the asymptotic value of the energy-momentum tensor of the matter at the site of the string. Using the Einstein equations one can rewrite this as

$$f_{\text{Iordanskii}}^\alpha = J \varepsilon^{\alpha\beta\gamma} u_\beta u_\mu R_\gamma^\mu, \quad (97)$$

where  $R_\gamma^\mu$  is the Riemannian curvature at the location of the string. This corresponds to the force which acts on a particle with spin  $J$  from the gravitational field owing to the interaction of the spin with the Riemann tensor (Thorne and Hartle 1985; Mino et al. 1997).

Note that previously we have shown how ideas first developed in the cosmological context (such as nucleation of bubbles of different broken symmetry phases during a rapid phase transition) could be applied to superfluid helium. Here we have the opposite case when ideas originating in helium physics have found application in other systems described by quantum field theory.

The Iordanskii force has been experimentally identified in rotating  $^3\text{He-B}$  (Bevan et al. 1997a). Eq. (42) describes the temperature dependence of the mutual friction coefficient  $d_\perp$ . Here the term  $m_3\mathcal{C}(T)$  arises from the spectral flow force which is discussed in Sec. 3.3.3 and vanishes at low temperatures. Thus at low temperatures  $d_\perp \approx -\rho_n/\rho$  (Kopnin et al. 1995), where  $\rho$  is the total

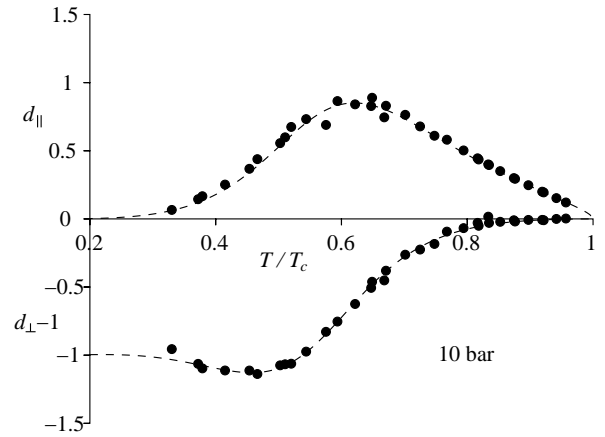


FIG. 33. Mutual friction parameters  $d_{\parallel,\perp}$  as a function of temperature in  $^3\text{He-B}$  at 10 bar. The negative sign of  $d_\perp - 1$  at  $T/T_c \approx 0.4-0.5$  constitutes experimental verification for the existence of the Iordanskii force. The curves are fits to measured data. (From Bevan et al. 1997a).

density of the liquid. The negative value of  $d_\perp$  arises entirely from the existence of the Iordanskii force. This is in accordance with the experimental data, which show that  $d_\perp$  does have negative values at low  $T$  (Fig. 33). At higher  $T$  the spectral flow force dominates, which leads to the sign reversal of  $d_\perp$ . This fact can be interpreted to represent experimental verification of the analog of the gravitational Aharonov-Bohm effect for a spinning cosmic string.

### 3.3. Spectral flow force and chiral anomaly

#### 3.3.1. Chiral anomaly

In the standard model of electroweak interactions there are certain quantities, like the baryon number  $Q_B$ , which are classically conserved but can be violated by quantum mechanical effects known generically as “chiral anomalies”. (Each of the quarks is assigned  $Q_B = 1/3$  while the leptons (neutrinos and the electron) have  $Q_B = 0$ .) The process leading to particle creation is called “spectral flow”, and can be pictured as a process in which fermions flow under an external perturbation from negative energy levels towards positive energy levels. Some fermions therefore cross zero energy and move from the Dirac sea into the observable positive energy world.

The origin for the axial anomaly can be seen from the behavior of a chiral particle in constant magnetic field,  $\mathbf{A} = (1/2)\mathbf{B} \times \mathbf{r}$ . A chiral particle we call a particle without mass, but with spin  $\vec{\sigma} [=1/2]$ . It can be classified as a right or left particle, depending on whether its spin is parallel or antiparallel to its momentum. The Hamiltonians for the right particle with the electric charge  $e_R$  and for the left particle with the electric charge  $e_L$  are

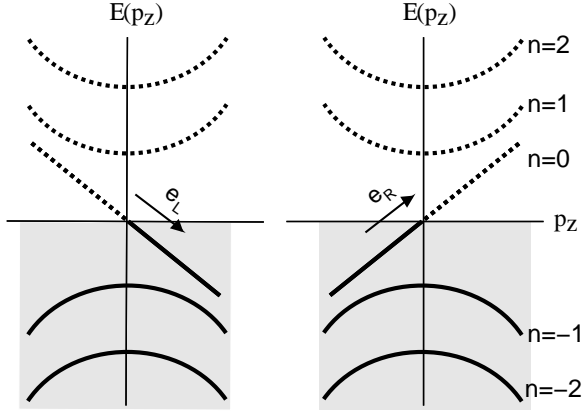


FIG. 34. The energy spectrum of a chiral particle in constant magnetic fields along  $\hat{z}$  (Landau levels). The plots on left and right show spectra for left and right particles, respectively.

$$\mathcal{H} = c\vec{\sigma} \cdot (\mathbf{p} - e_R \mathbf{A}), \quad \mathcal{H} = -c\vec{\sigma} \cdot (\mathbf{p} - e_L \mathbf{A}). \quad (98)$$

As usual, the motion of the particles in the plane perpendicular to  $\mathbf{B} \parallel \hat{z}$  is quantized in Landau levels. Thus the free motion is effectively reduced to one-dimensional motion along  $\mathbf{B}$  with momentum  $p_z$ . Fig. 34 shows the energy spectrum where the thick lines represent the occupied negative-energy states. The peculiar feature of the spectrum is that, because of the chirality of the particles, the lowest ( $n = 0$ ) Landau level is asymmetric. It crosses zero only in one direction:  $E = cp_z$  for the right particle and  $E = -cp_z$  for the left. If we now apply an electric field  $\mathbf{E}$  along  $z$ , particles are pushed from negative to positive energy levels according to the equation of motion  $\dot{p}_z = e_R E_z$  ( $\dot{p}_z = e_L E_z$ ) and the whole Dirac sea moves up (down) creating particles and electric charge from the vacuum. This motion of particles along the “anomalous” branch of the spectrum is called *spectral flow*. The rate of particle production is proportional to the density of states at the Landau level, which is

$$N_R(0) = \frac{|e_R \mathbf{B}|}{4\pi^2}, \quad N_L(0) = \frac{|e_L \mathbf{B}|}{4\pi^2}. \quad (99)$$

The production rate of particle number  $n = n_R + n_L$  and of charge  $Q = n_R e_R + n_L e_L$  from vacuum is

$$\dot{n} = \frac{1}{4\pi^2} (e_R^2 - e_L^2) \mathbf{E} \cdot \mathbf{B}, \quad \dot{Q} = \frac{1}{4\pi^2} (e_R^3 - e_L^3) \mathbf{E} \cdot \mathbf{B}. \quad (100)$$

This is an anomaly equation for the production of particles from vacuum of the type found by Adler (1969) and by Bell and Jackiw (1969) in the context of neutral pion decay. We see that for particle or charge creation, without creation of corresponding antiparticles, it is necessary to have an asymmetric branch in the dispersion

relations  $E(p)$ , which crosses the axis from negative to positive energy. Additionally, the symmetry between the left and right particles has to be violated:  $e_R \neq e_L$  for charge creation and  $e_R^2 \neq e_L^2$  for particle creation.

In the electroweak model there are two gauge fields whose “electric” and “magnetic” fields may become a source for baryoproduction: The hypercharge field  $U(1)$  and the weak field  $SU(2)$ . Anomalous zero mode branches exist in the core of a  $Z$ -string, where quarks, electrons and neutrinos are all chiral particles with known hypercharge and weak charges. If we consider a process in which one electron, two  $u$ -quarks and one  $d$ -quark are created, then lepton and baryon numbers are changed by one unit while electric charge is conserved (Bevan et al. 1997b). If we sum appropriate charges for all particles according to Eq. (100) the rate of this process is

$$\dot{n}_{\text{bar}} = \dot{n}_{\text{lept}} = \frac{N_F}{8\pi^2} (-\mathbf{B}_W^a \cdot \mathbf{E}_{aW} + \mathbf{B}_Y \cdot \mathbf{E}_Y) \quad (101)$$

where  $N_F = 3$  is the number of families (generations) of fermions,  $\mathbf{B}_W^a$  and  $\mathbf{E}_{aW}$  are the colored  $SU(2)$  magnetic and electric fields, while  $\mathbf{B}_Y$  and  $\mathbf{E}_Y$  are the magnetic and electric fields of the  $U(1)$  hypercharge. While a color and hypercharge magnetic flux is always present in the  $Z$ -string core, a color and hypercharge electric field can also be present along the string if the string is moving across a background electromagnetic field (Witten 1985) or in certain other processes such as the decoupling of two linked loops (Vachaspati and Field 1994, 1995; Garriga and Vachaspati 1995). Thus parallel electric and magnetic fields in the string change the baryonic charge and can lead to cosmological baryogenesis (Barriola 1995) and to the presence of antimatter in cosmic rays (Starkman 1996).

In superconductors and in superfluid  ${}^3\text{He}$  an anomalous zero mode branch exists for fermions in the core of quantized vortices. For electrons in superconductors it was first found by Caroli et al. (1964), and for vortices in superfluid  ${}^3\text{He}$  by Kopnin (1993). One of the physically important fermionic charges in  ${}^3\text{He-A}$ ,  ${}^3\text{He-B}$  and superconductors which, like baryonic charge in the standard model, is not conserved due to the anomaly, is linear momentum. The spectral flow of momentum along the zero mode branch leads to an additional “lift” force which acts on a moving vortex.

The analogy is clearest for the continuous vortex in  ${}^3\text{He-A}$ , which has two quanta of superfluid circulation,  $\nu = 2$  (Blaauwgeers et al. 2000). This vortex is similar to the continuous  $Z$ -vortex in electroweak theory: it is characterized by a continuous distribution of the order parameter vector  $\hat{\mathbf{I}}$ , which denotes the direction of the angular momentum of the Cooper pairs (Fig. 35). When multiplied by the Fermi wave number  $k_F = p_F/\hbar$ , this vector acts on the quasiparticles like an effective “electromagnetic” vector potential  $\mathbf{A} = k_F \hat{\mathbf{I}}$ . The quasiparticles

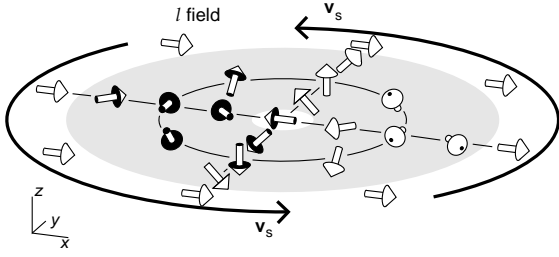


FIG. 35. The order parameter  $\hat{\mathbf{l}}$ -texture in the soft core of the continuous Anderson-Toulouse-Chechetkin vortex.

in  $^3\text{He-A}$ , which are close to the gap nodes, are chiral: they are either left or right handed (Volovik and Vachaspati 1996). As follows from the BCS theory of  $^3\text{He-A}$  the sign of the “electric” charge  $e$ , introduced in Sec. 3.2.1, simultaneously determines the chirality of the fermions. This is clearly seen from a simple isotropic example (with  $c_{\parallel} = c_{\perp} = c$ ):

$$\mathcal{H} = -ec\vec{\sigma} \cdot (\mathbf{p} - e\mathbf{A}) . \quad (102)$$

A particle with positive (negative)  $e$  at the north (south) pole is left-handed (right-handed). Here  $\vec{\sigma}$  is a Bogoliubov spin.

For such gapless chiral fermions the Adler-Bell-Jackiw anomaly applies and the momentum (“chiral charge”) of quasiparticles is not conserved in the presence of “electric” and “magnetic” fields, which are defined by

$$\mathbf{E} = k_F \partial_t \hat{\mathbf{l}}, \quad \mathbf{B} = k_F \nabla \times \hat{\mathbf{l}} . \quad (103)$$

In  $^3\text{He-A}$  each right-handed quasiparticle carries the momentum  $\mathbf{p}_R = p_F \hat{\mathbf{l}}$  (we reverse the sign of momentum when it is used as fermionic charge), and a left-handed quasiparticle has  $\mathbf{p}_L = -\mathbf{p}_R$ . According to Eq. (100) the production rates for right and left handed quasiparticles are (since  $e_R^2 = e_L^2 = 1$  in this case)

$$\dot{n}_R = -\dot{n}_L = \frac{1}{4\pi} \mathbf{E} \cdot \mathbf{B} . \quad (104)$$

As a result there is a net creation of quasiparticle momentum  $\mathbf{P}$  in a time-dependent texture:

$$\partial_t \mathbf{P} = \int d^3r (\mathbf{p}_R \dot{n}_R + \mathbf{p}_L \dot{n}_L) = \frac{1}{2\pi^2} \int d^3r p_F \hat{\mathbf{l}} (\mathbf{E} \cdot \mathbf{B}) . \quad (105)$$

What we know for sure is that the total linear momentum is conserved. Then Eq. (105) means that, in the presence of the time-dependent texture, the momentum is transferred from the superfluid motion of *vacuum* to *matter* (ie to the heat bath of quasiparticles which form the normal component).

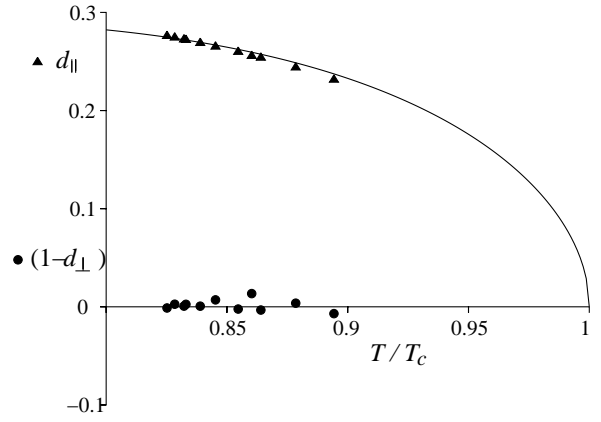


FIG. 36. Mutual friction parameters  $d_{\parallel}$  and  $(1-d_{\perp})$  in  $^3\text{He-A}$  at 29.3 bar. The curve is a theoretical fit to the data points. (From Bevan et al. 1997a).

### 3.3.2. Anomalous force acting on a continuous vortex and baryogenesis from textures

Let us take as an example the simplest model, namely the vortex with a *continuous soft* core structure in superfluid  $^3\text{He-A}$ . The core has the following distribution of the unit vector  $\hat{\mathbf{l}}(\mathbf{r})$ , which points in the direction of the point-like gap nodes in the smooth core

$$\hat{\mathbf{l}}(\mathbf{r}) = \hat{\mathbf{z}} \cos \eta(r) + \hat{\mathbf{r}} \sin \eta(r) , \quad (106)$$

where  $z, r, \phi$  are the cylindrical coordinates. Here  $\eta(r)$  is a function which ensures that the  $\hat{\mathbf{l}}$ -vector orientation changes within the smooth core from  $\hat{\mathbf{l}}(0) = -\hat{\mathbf{z}}$  to  $\hat{\mathbf{l}}(\infty) = \hat{\mathbf{z}}$ . The circulation of the superfluid velocity along a path far outside the soft core corresponds to  $\nu = 2$ :  $\oint d\mathbf{r} \cdot \mathbf{v}_s = 2\kappa$ . Such a continuous  $\hat{\mathbf{l}}$  texture thus represents a doubly quantized vortex without singularities. In practice the vortex measured in the NMR experiments is subject to an external magnetic field ( $\mathbf{B} \parallel \hat{\mathbf{z}}$ ) and the  $\hat{\mathbf{l}}$ -vector at infinity is fixed to the  $(x, y)$  plane (see Fig. 35 with  $\hat{\mathbf{l}}(\infty) = \hat{\mathbf{x}}$ ), but this does not change the topological structure of the vortex.

When the continuous vortex moves in  $^3\text{He-A}$  with a velocity  $\mathbf{v}_L$  it generates a time dependent  $\hat{\mathbf{l}}$  texture  $\hat{\mathbf{l}} = \hat{\mathbf{l}}(\mathbf{r} - \mathbf{v}_L t)$ . Hence both an “electric” and a “magnetic” field from Eq. (103) exist and this leads to “momentogenesis”. Integration of the anomalous momentum transfer in Eq. (105) over the cross-section of the soft core of the moving vortex gives an additional force which acts on the vortex due to spectral flow:

$$\mathbf{f}_{\text{sf}} = \partial_t \mathbf{P} = \pi \hbar \nu C_0 \hat{\mathbf{z}} \times (\mathbf{v}_L - \mathbf{v}_n) . \quad (107)$$

Here  $\hat{\mathbf{z}}$  is the direction of the vortex,  $C_0 = k_F^3/3\pi^2$ , and  $\mathbf{v}_n$  is the heat bath velocity. Thus we have obtained Eq. (37) with a temperature independent parameter  $\mathcal{C}(T) = C_0$ .

Measurements of the mutual friction coefficients in  $^3\text{He-A}$  with the continuous vortex (Bevan et al. 1997a) provide experimental verification for the spectral flow force. According to Eq. (42) it should be that  $d_{\perp} = (m_3\mathcal{C}_0 - \rho_n)/\rho_s$ . The value of  $m_3\mathcal{C}_0$  is the total mass density  $\rho$  in the normal phase. Its difference from  $\rho$  in the superfluid phase is thus determined by the effect of superfluidity on the particle density which is extremely small:  $\rho - m_3\mathcal{C}_0 \sim \rho(\Delta_0/v_F p_F)^2 = \rho(c_{\perp}/c_{\parallel})^2 \ll \rho$ . Thus one must have  $d_{\perp} \approx 1$  for all practical temperatures.  $^3\text{He-A}$  experiments at 29.3 bar and  $T > 0.82 T_c$  are consistent with this conclusion within experimental uncertainty: it was found that  $|1 - d_{\perp}| < 0.005$ , as demonstrated in Fig. 36.

### 3.3.3. Anomalous force acting on a singular vortex and baryogenesis with strings

The discussion of spectral flow in the previous sections and particularly Eqs. (100) cannot be directly applied to the singular vortex structures which are found in  $^3\text{He-B}$  and superconductors. The reason is that the deviation in the magnitude of the order parameter from its equilibrium value in the cores of such vortices create a potential well for the core quasiparticles. In this well quasiparticles have discrete energy levels with some characteristic separation  $\hbar\omega_0$  instead of continuous spectra (as a function of  $p_z$ ), as was considered above. Thus the theory of spectral flow becomes more complicated, but can still be constructed (Kopnin et al. 1995; Kopnin 2002).

The basic idea is that discrete levels have some broadening  $\hbar/\tau$ , resulting from the scattering of core excitations by the free excitations in the heat bath outside the core (or by impurities in superconductors). At low temperatures, when the width of levels is much less than their separation, i.e.  $\omega_0\tau \gg 1$ , spectral flow is essentially suppressed,  $\mathcal{C}(T) = 0$ . In the opposite case,  $\omega_0\tau \ll 1$ , the levels overlap and we have a situation similar to spectral flow in a continuous spectrum:  $\mathcal{C}(T) \approx \mathcal{C}_0$ . We may construct an interpolation formula between these two cases:

$$\mathcal{C}(T) \sim \frac{\mathcal{C}_0}{1 + \omega_0^2\tau^2}. \quad (108)$$

In fact, both the  $d_{\parallel}$  and  $d_{\perp}$  mutual friction coefficients are affected by this renormalization of the spectral flow force (Kopnin et al. 1995; Stone 1996):

$$d_{\parallel} - i(1 - d_{\perp}) = \frac{\rho}{\rho_s} \frac{\omega_0\tau}{1 + i\omega_0\tau} \tanh \frac{\Delta(T)}{2k_B T}. \quad (109)$$

Let us derive this equation using the Landau-type phenomenological description for fermions in the vortex core, as developed by Stone (1996). For simplicity we consider the axisymmetric vortex core; the general case of the asymmetric core is discussed by Kopnin and

Volovik (1998). The low-energy spectrum of Caroli-de-Gennes-Matricon quasiparticles around a vortex contains an anomalous branch of fermionic zero modes. In the case of the axisymmetric vortex, excitations on this branch are characterized by the angular momentum  $L_z$

$$E(L_z, p_z) = -\omega_0(p_z)L_z. \quad (110)$$

For superconductors with a coherence length  $\xi$  much larger than the inverse Fermi momentum,  $p_F\xi \gg 1$ , the electron wavelength is short compared with the core size, and the quasiclassical approximation is relevant. The quasiclassical angular momentum  $L_z$  is a continuous variable; thus the anomalous branch crosses zero as a function of  $L_z$  at  $L_z = 0$  and spectral flow can occur along this branch between the vacuum states with  $E < 0$  and the excited states with  $E > 0$ . Such spectral flow occurs during the motion of the vortex with respect to the normal component, where it is caused by the interaction with impurities in superconductors or with the thermal scattering states in superfluids. In the quasiclassical approximation, the Doppler shifted spectrum of the fermions in the moving vortex has the form

$$E(L_z, \mathbf{p}) = -\omega_0(p_z)L_z + (\mathbf{v}_s - \mathbf{v}_L) \cdot \mathbf{p}. \quad (111)$$

Here the momentum  $\mathbf{p}$  is assumed to be at the Fermi surface:  $\mathbf{p} = (p_F \sin \theta \sin \varphi, p_F \sin \theta \cos \varphi, p_F \cos \theta)$ . The azimuthal angle  $\varphi$  is canonically conjugated to the angular momentum  $L_z$ . This allows us to write the Boltzmann equation for the distribution function  $n(L_z, \varphi)$  at fixed  $p_z = p_F \cos \theta$ :

$$\begin{aligned} \partial_t n - \omega_0 \partial_{\varphi} n - \partial_{\varphi}((\mathbf{v}_s - \mathbf{v}_L) \cdot \mathbf{p}) \partial_{L_z} n \\ = -\frac{n(L_z, \varphi) - n_{\text{eq}}(L_z, \varphi)}{\tau}, \end{aligned} \quad (112)$$

where the collision time  $\tau$  characterizes the interaction of the bound state fermions with impurities or with the thermal fermions in the normal component outside the vortex core. The equilibrium distribution function is:

$$\begin{aligned} n_{\text{eq}}(L_z, \varphi) = \\ f(E - (\mathbf{v}_n - \mathbf{v}_L) \cdot \mathbf{p}) = f(-\omega_0 L_z + (\mathbf{v}_s - \mathbf{v}_n) \cdot \mathbf{p}), \end{aligned} \quad (113)$$

where  $f(E) = (1 + \exp(E/T))^{-1}$  is the Fermi-function.

Introducing the shifted variable

$$l = L_z - (\mathbf{v}_s - \mathbf{v}_n) \cdot \mathbf{p}/\omega_0, \quad (114)$$

one obtains the equation for  $n(l, \varphi)$

$$\begin{aligned} \partial_t n - \omega_0 \partial_{\varphi} n - \partial_{\varphi}((\mathbf{v}_n - \mathbf{v}_L) \cdot \mathbf{k}) \partial_l n \\ = -\frac{n(l, \varphi) - f(-\omega_0 l)}{\tau}, \end{aligned} \quad (115)$$

which does not contain  $\mathbf{v}_s$ . To find the force acting on the vortex from the heat bath environment, we are interested

in the evolution of the total momentum of quasiparticles in the vortex core:

$$\mathbf{P} = \sum \mathbf{p} = \int_{-p_F}^{p_F} \frac{dp_z}{2\pi} \mathbf{P}(p_z), \quad \mathbf{P}(p_z) = \frac{1}{2} \int dl \frac{d\varphi}{2\pi} n(l, \varphi) \mathbf{p}. \quad (116)$$

It appears that the equation for  $\mathbf{P}(p_z)$  can be written in closed form

$$\partial_t \mathbf{P}(p_z) - \omega_0 \hat{z} \times \mathbf{P}(p_z) + \frac{\mathbf{P}(p_z)}{\tau} = -\frac{1}{4} p_F^2 \sin^2 \theta \hat{z} \times (\mathbf{v}_n - \mathbf{v}_L) (f(\Delta(T)) - f(-\Delta(T))). \quad (117)$$

Here we take into account that  $\int dl \partial_l n$  is limited by the bound states below the gap  $\Delta(T)$  of bulk liquid: above the gap  $\Delta(T)$  the spectrum of fermions is continuous, *ie.* the inter-level distance  $\omega_0 = 0$ .

In steady state vortex motion one has  $\partial_t \mathbf{P}(p_z) = 0$ . Then, since  $f(\Delta(T)) - f(-\Delta(T)) = \tanh(\Delta(T)/2T)$ , one obtains the following contribution to the momentum from the heat bath to the core fermions due to the spectral flow of bound states below  $\Delta(T)$

$$\mathbf{F}_{\text{bsf}} = \int_{-p_F}^{p_F} \frac{dp_z}{2\pi} \frac{\mathbf{P}(p_z)}{\tau} = \frac{\kappa}{4} \tanh \frac{\Delta(T)}{2T} \times \int_{-p_F}^{p_F} \frac{dp_z}{2\pi} \frac{p_F^2 - p_z^2}{1 + \omega_0^2 \tau^2} [(\mathbf{v}_L - \mathbf{v}_n) \omega_0 \tau + \hat{z} \times (\mathbf{v}_L - \mathbf{v}_n)]. \quad (118)$$

The spectral flow of unbound states above  $\Delta(T)$  is not suppressed, the corresponding  $\omega_0 \tau = 0$ , since the distance between the levels in the continuous spectrum is  $\omega_0 = 0$ . This gives

$$\mathbf{F}_{\text{usf}} = \frac{\kappa}{4} p_F^2 \int_{-p_F}^{p_F} \frac{dp_z}{2\pi} \sin^2 \theta \left( 1 - \tanh \frac{\Delta(T)}{2T} \right) \hat{z} \times (\mathbf{v}_L - \mathbf{v}_n). \quad (119)$$

Thus the total nondissipative (transverse) and frictional (longitudinal) parts of the spectral-flow force are

$$\mathbf{F}_{\text{sf}}^\perp = \frac{\kappa}{4} \int_{-p_F}^{p_F} \frac{dp_z}{2\pi} (p_F^2 - p_z^2) \times \left[ 1 - \tanh \frac{\Delta(T)}{2T} \frac{\omega_0^2 \tau^2}{1 + \omega_0^2 \tau^2} \right] \hat{z} \times (\mathbf{v}_L - \mathbf{v}_n), \quad (120)$$

$$\mathbf{F}_{\text{sf}}^\parallel = (\mathbf{v}_L - \mathbf{v}_n) \frac{\kappa}{4} \tanh \frac{\Delta(T)}{2T} \times \int_{-p_F}^{p_F} \frac{dp_z}{2\pi} (p_F^2 - p_z^2) \frac{\omega_0 \tau}{1 + \omega_0^2 \tau^2} \quad (121)$$

In the limit  $\omega_0 \tau \ll 1$ , the friction force disappears, while the transverse spectral flow force is maximal and coincides with that obtained for the continuous vortex in Eq. (107) with the same value of  $\mathcal{C}_0 = (1/4) \int_{-p_F}^{p_F} dp_z (p_F^2 -$

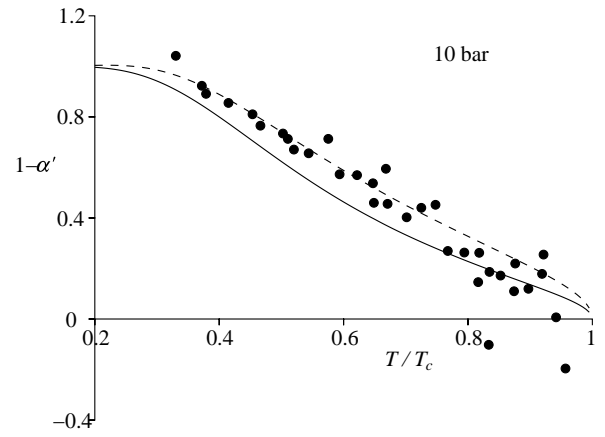


FIG. 37. Experimental values of  $1 - \alpha'$  in  ${}^3\text{He-B}$  at 10 bar compared with the theoretical result in Eq. (122). The full curve is for the theoretical value of  $\Delta(T)$  and the broken curve is the fit with reduced  $\Delta$ . (From Bevan et al. 1997a).

$p_z^2) = p_F^3/3\pi^2$ . In the general case the result in Eqs. (120) and (121) is complicated since both  $\omega_0$  and  $\tau$  depend on  $p_z$ . However, if one neglects this dependence and adds the Magnus and Iordanskii forces, one obtains Eq. (109) for all  $T$ . If the temperature is not too high, so that  $\tanh \Delta(T)/2T \approx 1$ , one obtains Eq. (108) for the renormalized spectral flow parameter.

Comparison of Eq. (109) with experiment should take into account that neither  $\omega_0$  nor  $\tau$  are known with good precision. However, the following combination of mutual friction coefficients does not depend on these parameters explicitly:

$$1 - \alpha' = \frac{1 - d_\perp}{d_\parallel^2 + (1 - d_\perp)^2} = \frac{\rho_s}{\rho} \left[ \tanh \frac{\Delta(T)}{2k_B T} \right]^{-1}. \quad (122)$$

This equation (Kopnin et al. 1995) is compared to experimental data on mutual friction in  ${}^3\text{He-B}$  (Bevan et al. 1997a) in Fig. 37. The agreement is excellent in view of the approximations in the theory.

This shows that the chiral anomaly is relevant for the interactions of condensed matter vortices (analogues of strings) with fermionic quasiparticles (analogues of quarks and leptons). For continuous vortices in  ${}^3\text{He-A}$  the spectral flow of fermions between the superfluid ground state (vacuum) and the heat bath of positive energy particles forming the normal component (matter) dominates at any relevant temperature. For singular vortices in  ${}^3\text{He-B}$  it is important at  $T \sim T_c$  and vanishes at  $T \ll T_c$ .

It is interesting to note that in a homogeneous ground state (vacuum) momentum (fermionic charge) is conserved separately in the ground state (vacuum) and in the heat bath of excitations (matter). Topological defects are thus the mediators for the transfer of momentum between these two subsystems. The motion of a vortex

across the flow changes both the topological charge of the vacuum (say, the winding number of superflow in a torus geometry) and the fermionic charge (angular momentum in the same geometry). All these processes are similar to those involved in the cosmological production of baryons and can thus be investigated in detail.

However, it is important to note that although spectral flow leads to anomalous creation of fermionic charge from vacuum, the total fermionic charge of vacuum plus matter remains conserved. There is also no intrinsic bias in this process for the direction of charge transfer: from vacuum to matter or in the opposite direction. The necessary conditions for this mechanism to start operating are that the system is in a non-equilibrium state and under the influence of symmetry breaking which biases the direction of charge transfer. How such conditions were realized in the early Universe is not clear at present – if we interpret the positive baryonic charge of matter in our Universe to arise from spectral flow. But it is commonly believed that broken P and CP invariances play crucial roles. In contrast in the  ${}^3\text{He}$  case the situation is completely under control: The relevant symmetry breaking is achieved by applying rotation or a magnetic field, while the non-equilibrium state is generated by applying external superflow.

The experimental verification of momentogenesis in superfluid  ${}^3\text{He}$  can thus be viewed to support these ideas of cosmological baryogenesis via spectral flow and points to a future where several cosmological problems are modelled and studied in light of the superfluid  ${}^3\text{He}$  example (Volovik 2003). Now let us consider the opposite effect which leads to the analogue of magnetogenesis.

### 3.4. Analog of magnetogenesis: vortex textures generated in normal-superfluid counterflow

From Eq. (100) it follows that the magnetic field configuration can absorb fermionic charge. If this magnetic field has helicity, it acquires an excess of right-moving particles over left-moving particles:

$$(n_R - n_L)_\mathbf{A} = \frac{1}{2\pi^2} \mathbf{A} \cdot (\nabla \times \mathbf{A}) . \quad (123)$$

The right-hand side is the so called Chern-Simons (or topological) charge of the magnetic field.

The transformation of particles into a magnetic field configuration opens the possibility to examine the cosmological origin of galactic magnetic fields from a system of fermions. This is the essential step in the scenario described by Joyce and Shaposhnikov (1997). In this model an initial excess of right-handed electrons,  $e_R$ , was assumed to have been generated in the early Universe. This excess would then have survived until the electroweak phase transition (at about  $10^{-10}$  s after the big bang) at which point anomalous lepton (and baryon) number

violating processes became efficient enough to erase the excess. However, it appears that well before the electroweak transition an instability developed, where the excess of the right electrons transformed into a hypermagnetic field. Then, when the electroweak transition took place, it transformed part of the hypermagnetic field into electromagnetic field, so that the universe was bestowed with a primordial (electro-) magnetic field.

We can now discuss the corresponding process in  ${}^3\text{He-A}$  – the transformation of fermionic charge to magnetic field. In our case it is the quasiparticle momentum which plays the part of the relevant fermionic charge. The net quasiparticle momentum is generated by the relative flow of the normal and superfluid components. This fermionic charge is transformed via the chiral anomaly to order parameter texture which, as we have seen, plays the part of the magnetic field. The transformation occurs in the form of an instability which transfers the excess in momentum to the formation of  $\hat{\mathbf{l}}$ -textures. The process corresponds to the counterflow instability observed in  ${}^3\text{He-A}$ , which has been discussed both experimentally and theoretically (Ruutu et al. 1997b). Thus the  ${}^3\text{He-A}$  analogy closely follows the cosmological scenario described by Joyce and Shaposhnikov (1997).

Let us discuss this instability. In the presence of counterflow,  $\mathbf{v} = \mathbf{v}_n - \mathbf{v}_s$ , of the normal component of  ${}^3\text{He-A}$  liquid with respect to the superfluid, the  $\hat{\mathbf{l}}$ -vector is oriented along the flow,  $\hat{\mathbf{l}}_0 \parallel \mathbf{v}$ . We are interested in the stability condition for such homogeneous counterflow with respect to the generation of inhomogeneous perturbations  $\delta\hat{\mathbf{l}}$ ,

$$\hat{\mathbf{l}} = \hat{\mathbf{l}}_0 + \delta\hat{\mathbf{l}}(\mathbf{r}, t) , \quad (124)$$

keeping in mind that the space and time dependences of  $\delta\hat{\mathbf{l}}$  correspond to “hyperclectric field”  $\mathbf{E} = k_F \partial_t \delta\hat{\mathbf{l}}$  and “hypermagnetic field”  $\mathbf{B} = k_F \nabla \times \delta\hat{\mathbf{l}}$ .

It is important for our consideration that the  ${}^3\text{He-A}$  liquid is anisotropic in the same manner as a nematic liquid crystal. For the relativistic fermions this means that their motion is determined by the geometry of some effective spacetime which in  ${}^3\text{He-A}$  is described by the metric tensor in Eq. (81). As we have already discussed above, in the presence of counterflow the energy of quasiparticles is Doppler shifted by the amount  $\mathbf{p} \cdot \mathbf{v}$ . Since the quasiparticles are concentrated near the gap nodes, this energy shift is constant and opposite for the two gap nodes:  $\mathbf{p} \cdot \mathbf{v} \approx \pm p_F (\hat{\mathbf{l}}_0 \cdot \mathbf{v})$ . The counterflow therefore produces what would be an effective chemical potential in particle physics, which has opposite sign for the right- and left-handed particles:

$$\mu_R = -\mu_L = p_F (\hat{\mathbf{l}}_0 \cdot \mathbf{v}) . \quad (125)$$

The kinetic energy of the counterflow is

$$E_{\text{kin}} = \frac{1}{2} \mathbf{v} \rho_{n\parallel} \mathbf{v} . \quad (126)$$



Here the density of the normal component is a tensor in the anisotropic  $^3\text{He-A}$  liquid, and only the longitudinal component  $\rho_{n\parallel}$  is involved.

Let us consider the low-temperature limit  $T \ll T_c$ , where  $T_c \sim \Delta_0$  is the superfluid transition temperature. Then using the expression for the longitudinal density of the normal component of  $^3\text{He-A}$  (Vollhardt and Wölfle 1990)

$$\rho_{n\parallel} = \pi^2 \rho \frac{m_3^*}{m_3} \left( \frac{k_B T}{\Delta_0} \right)^2 \quad (127)$$

and also the  $^3\text{He-A}$  equivalent of the chemical potential (125) one obtains

$$E_{\text{kin}} \approx \frac{1}{6} m_3^* k_F^3 \frac{T^2}{\Delta_0^2} (\hat{\mathbf{l}}_0 \cdot \mathbf{v})^2 \equiv \frac{1}{6} \sqrt{-g} T^2 \mu_R^2. \quad (128)$$

In the last equality an over-all constant appears to be the square root of the determinant of an effective metric in  $^3\text{He-A}$ :  $\sqrt{-g} = 1/c_{\parallel} c_{\perp}^2 = m_3^* k_F / \Delta_0^2$ . In relativistic theories the rhs of Eq. (128) is exactly the energy density of the massless right-handed electrons in the presence of the chemical potential  $\mu_R$ . Thus the kinetic energy, stored in the counterflow, is exactly analogous to the energy stored in the right-handed electrons. The same analogy occurs between the net quasiparticle linear momentum,  $\mathbf{P} = \rho_n \mathbf{v}$ , along  $\hat{\mathbf{l}}_0$  and the chiral charge of the right electrons,

$$n_R \equiv \frac{1}{p_F} \mathbf{P} \cdot \hat{\mathbf{l}}_0. \quad (129)$$

The inhomogeneity which absorbs the fermionic charge, is represented by a magnetic field configuration in real physical vacuum and by a  $\delta\hat{\mathbf{l}}$ -texture in  $^3\text{He-A}$ . However, Eq. (123) applies in both cases, if in  $^3\text{He-A}$  we use the standard identification  $\mathbf{A} = k_F \delta\hat{\mathbf{l}}$ .

Just as in the particle physics case, we now consider the instability towards the production of the “magnetic” texture due to the excess of chiral particles. This instability can be seen by considering the gradient energy of the inhomogeneous texture on the background of the superflow. In the geometry of the superflow, the textural contribution to the free energy of the  $\delta\hat{\mathbf{l}}$ -vector is completely equivalent to the conventional energy of the hypermagnetic field (Volovik 1992)

$$\begin{aligned} F_{\text{grad}} &= \ln \left( \frac{\Delta_0^2}{T^2} \right) \frac{p_F^2 v_F}{24\pi^2 \hbar} (\hat{\mathbf{l}}_0 \times (\nabla \times \delta\hat{\mathbf{l}}))^2 \\ &\equiv \frac{\sqrt{-g}}{4\pi e_{\text{eff}}^2} g^{ij} g^{kl} F_{ik} F_{jl} = F_{\text{mag}}. \end{aligned} \quad (130)$$

Here  $F_{ik} = \nabla_i A_k - \nabla_k A_i$  and we again have included the effective anisotropic metric in Eq. (81) appropriate for  $^3\text{He-A}$ .

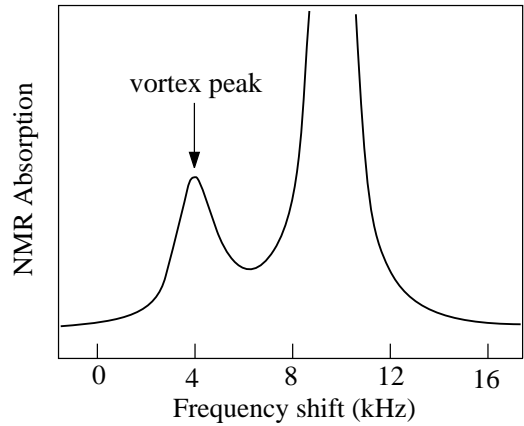


FIG. 38. NMR signal from an array of continuous ATC vortices, with the frequency shift from the Larmor value plotted on the horizontal axis. The large truncated peak on the right is generated by the bulk order-parameter texture, while the small satellite peak on the left is produced by the continuous soft-core vortex textures. The frequency shift of the satellite peak from the Larmor frequency indicates the type of vortex, while the intensity of the peak is proportional to the number of vortices of this particular type.

It is interesting that the logarithmic factor in the gradient energy plays the part of the running coupling  $e_{\text{eff}}^{-2} = (1/3\pi\hbar c) \ln(\Delta_0/T)$  in particle physics, where  $e_{\text{eff}}$  is the effective hyperelectric charge; while the gap amplitude  $\Delta_0$ , the ultraviolet cutoff, plays the part of the Planck energy scale. Now if one has the counterflow in  $^3\text{He-A}$ , or its equivalent – an excess of chiral charge produced by the chemical potential  $\mu_R$  – the anomaly gives rise to an additional effective term in the magnetic energy, corresponding to the interaction of the charge absorbed by the magnetic field with the chemical potential. This effective energy term is:

$$\begin{aligned} F_{CS} &= (n_R - n_L) \mu_R = \frac{1}{2\pi^2} \mu_R \mathbf{A} \cdot (\nabla \times \mathbf{A}) \\ &= \frac{3\hbar}{2m} \rho (\hat{\mathbf{l}}_0 \cdot \mathbf{v}) (\delta\hat{\mathbf{l}} \cdot \nabla \times \delta\hat{\mathbf{l}}). \end{aligned} \quad (131)$$

The rhs corresponds to the well known anomalous interaction of the counterflow with the  $\hat{\mathbf{l}}$ -texture in  $^3\text{He-A}$ , where  $\rho$  is the mass density of  $^3\text{He}$  (Volovik 1992) (the additional factor of  $3/2$  enters due to nonlinear effects).

For us the most important property of this term is that it is linear in the derivatives of  $\delta\hat{\mathbf{l}}$ . Its sign thus can be negative, while its magnitude can exceed the positive quadratic term in Eq. (130). This leads to the helical instability where the inhomogeneous  $\delta\hat{\mathbf{l}}$ -field is formed. During this instability the kinetic energy of the quasiparticles in the counterflow (analog of the energy stored in the fermionic degrees of freedom) is converted into the energy of inhomogeneity  $\nabla \times \delta\hat{\mathbf{l}}$ , which is the analog of the magnetic energy of the hypercharge field.

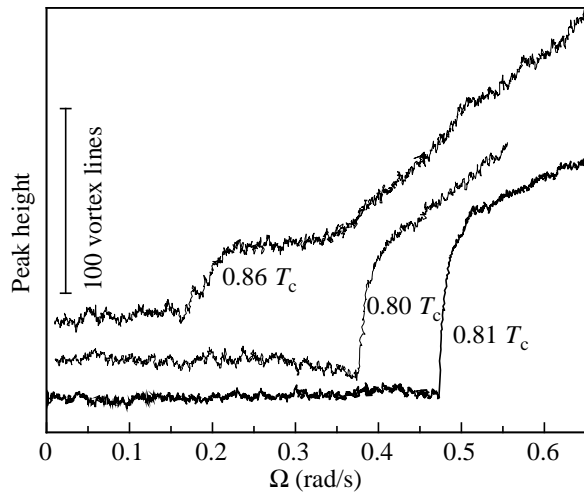


FIG. 39. The height of the satellite peak, which is generated by continuous vortex lines, is here monitored during a slow increase of  $\Omega$ . Initially there are no vortex lines in the sample and the peak height is zero. When the velocity of the counterflow  $\mathbf{v}$  in the  $\hat{\mathbf{l}}_0$  direction (corresponding to the chemical potential  $\mu_R$  of the chiral electrons) exceeds some critical value, a textural instability occurs and the texture transforms into a configuration with a lower critical velocity. Simultaneously a larger number of vortex lines is formed. This means that the center of the sample cylinder becomes suddenly filled with the  $\hat{\mathbf{l}}$ -texture (or hypermagnetic field) which forms a central cluster of continuous vortex lines. (From Ruutu et al. (1996c)).

When the helical instability develops in  $^3\text{He-A}$ , the final result is the formation of a  $\hat{\mathbf{l}}$ -texture, which represents a large jump from the vortex-free counterflow texture towards the global free energy minimum, the equilibrium vortex texture. The new texture contains a central part with a periodic  $\hat{\mathbf{l}}$ -texture, where the elementary lattice cell represents a so-called Anderson-Toulouse-Chechetkin (ATC) continuous vortex (Fig. 35). ATC vortices give rise to a characteristic satellite peak in the NMR absorption spectrum where their number is directly proportional to the height of the satellite peak, Fig. 38 (Blaauwgeers et al. 2000).

Experimentally this is observed when the rotation velocity is slowly increased, starting from a state with vortex-free counterflow (*ie.* with fermionic charge, but no hypermagnetic field). The helical instability is then observed as a discontinuity, when the vortex satellite is suddenly formed (Fig. 39). Its peak height jumps from zero to a magnitude which approaches that in the equilibrium vortex state, which means that the counterflow is essentially reduced and the number of vortex lines is close to that in equilibrium. Most of the counterflow (fermionic charge) thus becomes converted into the vortex texture (magnetic field).

Together with the results of Bevan et al. (1997b), the textural superflow instability shows that the chiral

anomaly is an important mechanism in the interaction of vortex textures (the analogue of the hypercharge magnetic fields and cosmic strings) with fermionic excitations (analogue of quarks and leptons). These two experiments verified both processes which are induced by the anomaly: the nucleation of fermionic charge from vacuum, observed by Bevan et al. (1997b), and the inverse process of the nucleation of an effective magnetic field from the fermion current as observed by Ruutu et al. (1997b).

### 3.5. Vortex mass: chiral fermions in strong magnetic field

Until now we have assumed that the mass  $M_V$  of a vortex can be neglected in experimental vortex dynamics. How well justified is this approach? The term  $M_V \partial_t \mathbf{v}_L$  in the force balance equation for the vortex contains the time derivative and thus at very low frequencies of vortex motion it can be neglected compared to other forces, which are directly proportional to  $\mathbf{v}_L$ . To be more quantitative, we estimate the vortex mass in the BCS superfluids and superconductors. There are several contributions to the vortex mass. It will also become clear that these are related to some most peculiar phenomena in quantum field theory. We start from the contribution, which is relevant for the Bose superfluid  $^4\text{He}$ .

#### 3.5.1. “Relativistic” mass of the vortex

In the hydrodynamic theory the mass of the vortex is nonzero owing to the compressibility of the liquid. Since sound propagation in fluids is similar to light propagation in vacuum, the hydrodynamic energy of the vortex, soliton or other extended object moving in the liquid is connected with its hydrodynamic mass per unit length by the “relativistic” equation  $E = ms^2$ , where the speed of sound  $s$  substitutes the speed of light (Davis 1992; Duan 1995; Kao and Lee 1995; Iengo and Jug 1995; Wexler and Thouless 1996). Thus the hydrodynamic mass of a vortex loop of length  $L$  at  $T = 0$  is according to Eq. (18):

$$M_{\text{compr}} = \frac{E_{\text{kin}}}{s^2} = \frac{\rho \kappa^2 L}{4\pi s^2} \ln \frac{L}{\xi}. \quad (132)$$

For Fermi superfluids  $s$  is on the order of the Fermi velocity  $v_F \sim p_F/m$  ( $m$  is the mass of the electron in metals or of the  $^3\text{He}$  atom), and the estimate for the hydrodynamic mass of a small vortex loop of length  $L$  is  $M_{\text{compr}} \sim \rho a^2 L \ln L/\xi$ , where  $a$  is the interatomic distance. For superfluid  $^4\text{He}$ , where the core size  $\xi \sim a$ , we can roughly speaking associate the hydrodynamic vortex mass  $\sim \rho a^2 L$  with the “mass of the liquid in the vortex core volume”. However for  $^3\text{He}$  superfluids and for superconductors, where  $\xi \gg a$ , the hydrodynamic vortex mass

is much less than  $\rho\xi^2L$  and other contributions become more important.

### 3.5.2. Contribution from bound states to the mass of a singular vortex

It appears that the most important contribution to vortex mass originates from the quasiparticles occupying the bound states in the vortex core and thus forming the normal component concentrated in the core. For the vortices in conventional superconductors and in  $^3\text{He-B}$  this contribution to the vortex mass depends on  $\omega_0\tau$  and in the clean-limit case it is proportional to the mass of the liquid in the vortex core, as was first found by Kopnin (1978) for superconductors and by Kopnin and Salomaa (1991) for superfluid  $^3\text{He-B}$ :  $M_{\text{Kopnin}} \sim \rho\xi^2L$ . This core mass is essentially larger than the logarithmically divergent contribution, which comes from the compressibility. In spite of the logarithmic divergence, the latter contains the speed of sound in the denominator and thus is smaller by the factor  $(a/\xi)^2 \ll 1$ , where  $a$  is the interatomic distance. The compressibility mass of the vortex dominates in Bose superfluids, where the core size is small,  $\xi \sim a$ .

According to Kopnin's theory the core mass comes from the fermions trapped in the vortex core (Kopnin 1978; Kopnin and Salomaa 1991; van Otterlo et al. 1995; Volovik 1997; Kopnin and Vinokur 1998). This Kopnin mass of the vortex can be derived using a phenomenological approach. Let us consider the limit of low  $T$  in the superclean regime  $\omega_0\tau \gg 1$  (Volovik 1997). If the vortex moves with velocity  $\mathbf{v}_L$  with respect to the superfluid component, the fermionic energy spectrum in the vortex frame is Doppler shifted and has in Eq. (111) the form:  $E = E_0(q) - \mathbf{p} \cdot \mathbf{v}_L$ , where  $q$  represents the fermionic degrees of freedom in the stationary vortex. The summation over the fermionic degrees of freedom leads to the extra linear momentum of the vortex  $\propto \mathbf{v}_L$ :

$$\begin{aligned} \mathbf{P} &= \sum_q \mathbf{p} \theta(-E) = \sum_q \mathbf{p}(\mathbf{k} \cdot \mathbf{v}_L) \delta(E_0) = M_{\text{Kopnin}} \mathbf{v}_L, \\ M_{\text{Kopnin}} &= \frac{1}{2} \sum_q \mathbf{p}_\perp^2 \delta(E_0). \end{aligned} \quad (133)$$

For the axisymmetric vortex, where  $E_0 = -L_z\omega_0(p_z)$  and  $\sum_q = \int dL_z dp_z dz / 2\pi$ , one has

$$M_{\text{Kopnin}} = L \int_{-p_F}^{p_F} \frac{dp_z}{4\pi} \frac{p_F^2 - p_z^2}{\omega_0(p_z)}. \quad (134)$$

Eq. (134) can also be obtained from the time dependent kinetic equation (112). It is the coefficient in the contribution to the longitudinal force, which is linear in external frequency  $\omega$ :  $\mathbf{F}_{\text{sf}}^\parallel = -i\omega M_{\text{Kopnin}} \mathbf{v}_L$ .

Note that this vortex mass is determined in essentially the same way as the normal component density in the

bulk system. The Kopnin vortex mass is nonzero if the density of fermionic states is finite in the vortex core, which is determined by the inter-level spacing  $\omega_0$  in the core:  $N(0) \propto 1/\omega_0$ . That gives for the Kopnin vortex mass per unit length an estimation:  $M_{\text{Kopnin}} \sim p_F^3/\omega_0 \sim \rho\xi^2$ . A method to measure this contribution for the  $^3\text{He-B}$  vortex with spontaneously broken axisymmetry of the vortex core, by driving the core into rapid rotation with an NMR excitation field, has been suggested by Kopnin and Volovik (1998). The much stronger connection to the normal component fraction in the core of a vortex with continuous structure, like the dominant vortex line in  $^3\text{He-A}$ , will be examined in the next subsection.

### 3.5.3. Kopnin vortex mass in the continuous-core model: connection to chiral fermions in magnetic field

The continuous-core vortex in  $^3\text{He-A}$  is the best example – a model case – which helps to understand the vortex core mass. The continuous-core model can also be applied to other Fermi superfluids and superconductors: the singular core can thereby be smoothed, so that the  $1/r$ -singularity of the superfluid velocity is removed, by introducing point nodes in the superfluid energy gap in the core region (Fig. 40). As a result the superfluid/superconducting state in the vortex core acquires the properties of  $^3\text{He-A}$  with its continuous vorticity and point gap nodes (Volovik and Mineev 1982; Salomaa and Volovik 1987). After that one can easily separate different contributions to the vortex mass. Actually this is not only a model: Spontaneous smoothing of the velocity singularity occurs in the cores of both types of  $^3\text{He-B}$  vortices (Salomaa and Volovik 1987), while in heavy fermion and high- $T_c$  superconductors such smoothing can occur due to the admixture of different pairing states in the vortex core.

For the smoothed singly quantized vortices of  $^3\text{He-B}$  and superconductors one has two  $\hat{\mathbf{I}}$ -vectors:  $\hat{\mathbf{I}}_1$  and  $\hat{\mathbf{I}}_2$ , each for one of the two spin projections. The simplest distribution of both fields is given by Eq. (106) with such  $\eta(r)$  that  $\hat{\mathbf{I}}_1(0) = \hat{\mathbf{I}}_2(0) = -\hat{\mathbf{z}}$  and  $\hat{\mathbf{I}}_1(\infty) = -\hat{\mathbf{I}}_2(\infty) = \hat{\mathbf{r}}$  (Salomaa and Volovik 1987). The region of radius  $R_{\text{sc}}$ , where the texture of  $\hat{\mathbf{I}}$ -vectors is concentrated, represents the smoothed *nonsingular core* of the vortex.

In the continuous vortex, the normal component in the core can be considered to be a local quantity, determined at each point in the vortex core. This consideration is valid for a smooth core with radius  $R_{\text{sc}} \gg \xi$ , where the local classical description of the fermionic spectrum can be applied. The main contribution comes from the point-like gap nodes, where the classical spectrum has the form  $E_0 = \sqrt{v_F^2(p - p_F)^2 + \Delta_0^2(\hat{\mathbf{p}} \times \hat{\mathbf{I}})^2}$  and  $\Delta_0$  is the gap amplitude. In the presence of a gradient in the  $\hat{\mathbf{I}}$ -field, which acts on the quasiparticles as an effective magnetic field,

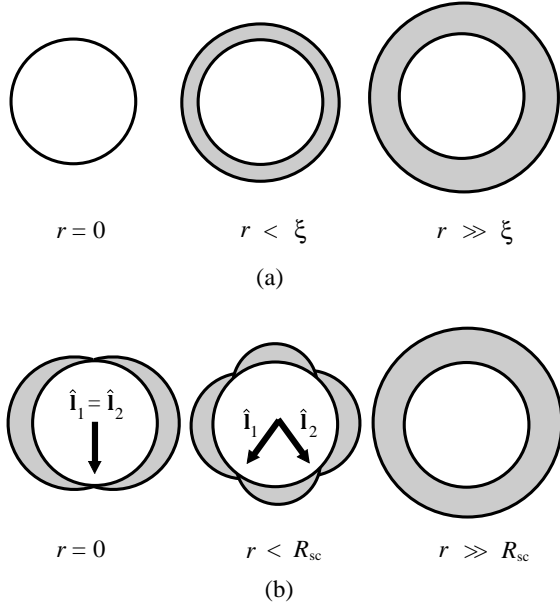


FIG. 40. Smoothing operation of the singular vortex core. (a) In the singular vortex the gap is continuously reduced and becomes zero exactly on the vortex axis (at  $r = 0$ ). (b) For some vortices it is energetically favorable to avoid the vanishing order parameter at  $r = 0$ . Instead, within the smooth core,  $r < R_{sc}$ , point-like gap nodes appear in the spectrum of fermions (Volovik and Mineev 1982). The unit vectors  $\hat{\mathbf{i}}_1$  and  $\hat{\mathbf{i}}_2$  show the directions to the nodes at different  $r$ . Close to the gap nodes the spectrum of the fermions is similar to that in  ${}^3\text{He-A}$  (example at  $r = 0$ ).

this gapless spectrum leads to the nonzero local DOS, discussed in Sec. 3.3.1 for the relativistic chiral fermions. To apply the DOS in Eq. (99) to the case of anisotropic  ${}^3\text{He-A}$ , one must make the covariant generalization of the DOS, by introducing the general metric tensor and then substituting it by the effective  ${}^3\text{He-A}$  metrics which describes the anisotropy of  ${}^3\text{He-A}$ . The general form of the DOS of the chiral fermions in the curved space is

$$N(0) = \frac{|e|}{2\pi^2} \sqrt{-g} \sqrt{\frac{1}{2} g^{ij} g^{kl} F_{ik} F_{jl}}, \quad (135)$$

where  $F_{ik}$  is defined on p. 57. One now can apply this to  ${}^3\text{He-A}$  where  $|e| = 1$ , and the metric tensor is given by Eq. (81). Neglecting the dependence of the small velocity field  $v_s$  in the smooth core, one obtains the following local DOS for the fermions in the  $\hat{\mathbf{I}}$ -texture at  $T = 0$ :

$$N(0, \mathbf{r}) = \frac{p_F^2}{2\pi^2 \Delta_A} |(\hat{\mathbf{I}} \times (\nabla \times \hat{\mathbf{I}}))|. \quad (136)$$

This DOS can be inserted in the expression for the local density of the normal component at  $T = 0$  (see Eq. (5.24) in the review by Volovik (1990)):

$$(\rho_n)_{ij}(\mathbf{r}) = \hat{l}_i \hat{l}_j p_F^2 N(0, \mathbf{r}). \quad (137)$$

For the axisymmetric continuous vortex (Eq. (106)) one has

$$N(0, \mathbf{r}) = \frac{p_F^2}{2\pi^2 \Delta_A} \sin \eta |\partial_r \eta|. \quad (138)$$

The integral of this normal density tensor over the cross section of the soft core gives the Kopnin mass of the vortex in the local density representation

$$\begin{aligned} M_{\text{Kopnin}} &= \int d^2 r (\hat{\mathbf{v}}_L \cdot \hat{\mathbf{I}})^2 p_F^2 N(0, \mathbf{r}) \\ &= \frac{p_F^2}{4\pi^2 \Delta_A} \int d^2 r \sin^3 \eta(r) |\partial_r \eta|, \end{aligned} \quad (139)$$

where  $\hat{\mathbf{v}}_L$  is the unit vector in the direction of the vortex velocity  $\mathbf{v}_L$ . The same equation for the mass can be obtained from Eq. (134), using the exact expression for the inter-level distance  $\omega_0(p_z)$  (Volovik 1997).

Since  $v_F/\Delta_0 \sim \xi$  one obtains that the Kopnin mass of the continuous vortex  $\sim \rho \xi R_{sc}$ , i.e. it is linear in the dimension  $R_{sc}$  of the core (Kopnin 1995). Thus it follows that the area law for the vortex mass is valid only for vortices with a core size of order  $\xi$  (i.e.  $R_{sc} \sim \xi$ ).

Note that the vortex mass discussed above comes from the normal component trapped in the vortex and which thus moves with the vortex velocity,  $\mathbf{v}_n = \mathbf{v}_L$ . In this consideration it is assumed that  $\omega_0 \tau \gg 1$ . In this limit the normal component in the core and the normal component in the heat bath do not interact with each other and thus can move with different velocities. The local hydrodynamic energy of the normal component trapped by the vortex is

$$F = \frac{1}{2} (\rho_n)_{ij}(\mathbf{r}) (\mathbf{v}_L - \mathbf{v}_s)_i (\mathbf{v}_L - \mathbf{v}_s)_j. \quad (140)$$

This can be rewritten in a form, which is valid also for chiral fermions:

$$F = \frac{\mu_R^2 + \mu_L^2}{8\pi^2} \sqrt{-g} \sqrt{\frac{1}{2} g^{ij} g^{kl} F_{ik} F_{jl}}, \quad (141)$$

where, as before in Eq. (125), the chemical potential of the left and right fermions in  ${}^3\text{He-A}$  are expressed in terms of the counterflow:  $\mu_R = -\mu_L = p_F (\hat{\mathbf{I}} \cdot \mathbf{v})$ . Eq. (141) represents the magnetic energy of the chiral particles with finite chemical potential in a strong magnetic field  $B \gg \mu^2$ .

### 3.5.4. Associated hydrodynamic mass

Recently the problem of another vortex mass of hydrodynamic origin was raised by Sonin et al. (1998). It is the so-called backflow mass discussed by Baym and Chandler (1983), which also can be proportional to the core area. Here we compare these two contributions in

the superclean regime and at low  $T \ll T_c$  using the model of a continuous core. The associated (or induced) mass appears when, say, an external body moves in the superfluid. This mass depends on the geometry of the body. For the moving cylinder of radius  $R$  it is the mass of the liquid displaced by the cylinder,

$$M_{\text{associated}} = \pi R^2 \rho \quad , \quad (142)$$

which is to be added to the actual mass of the cylinder to obtain the total inertial mass of the body. In superfluids this part of the superfluid component moves with the external body and thus can be associated with the normal component. A similar mass is responsible for the normal component in porous materials, in aerogel for instance, where some part of the superfluid is hydrodynamically trapped by the pores. It is removed from the overall superfluid motion and thus becomes part of the normal component.

In the case when a vortex is trapped on a wire of radius  $R_{\text{wc}} \gg \xi$ , such that the wire replaces the vortex core, Eq. (142) gives the vortex mass due to the backflow around the moving core. This is the simplest realization of the backflow mass of the vortex discussed by Baym and Chandler (1983). For this vortex with a wire-core the Baym-Chandler mass is the dominant mass of the vortex. The Kopnin mass, which can result from normal excitations trapped near the surface of the wire, is essentially less.

Let us now consider the Baym-Chandler mass for the free vortex at  $T = 0$ , using again the continuous-core model. In the wire-core vortex this mass arises from the backflow caused by the inhomogeneity in  $\rho_s$ :  $\rho_s(r > R_{\text{wc}}) = \rho$  and  $\rho_s(r < R_{\text{wc}}) = 0$ . Similar but less severe inhomogeneity of  $\rho_s = \rho - \rho_n$  occurs in the continuous-core vortex due to the nonzero local normal density in Eq. (137). Owing to the profile of the local superfluid density, the external flow is disturbed near the core according to the continuity equation

$$\nabla \cdot (\rho_s \mathbf{v}_s) = 0 \quad . \quad (143)$$

If the smooth core is large,  $R_{\text{sc}} \gg \xi$ , the deviation of the superfluid component inside the smooth core is small from its asymptotic value outside the core:  $\delta\rho_s = \rho - \rho_s \sim (\xi/R_{\text{sc}})\rho \ll \rho$  and can be considered as a perturbation. Thus if the asymptotic value of the velocity of the superfluid component with respect of the core is  $\mathbf{v}_{s0} = -\mathbf{v}_L$ , the disturbance  $\delta\mathbf{v}_s = \nabla\Phi$  of the superflow in the smooth core is given by:

$$\rho \nabla^2 \Phi = v_{s0}^i \nabla^j (\rho_n)_{ij} \quad . \quad (144)$$

The kinetic energy of the backflow gives the Baym-Chandler mass of the vortex

$$M_{\text{BC}} = \frac{\rho}{v_{s0}^2} \int d^2r (\nabla\Phi)^2 \quad . \quad (145)$$

In the simple approximation that the normal component in Eq. (137) is considered isotropic, one obtains

$$M_{\text{BC}} = \frac{1}{2\rho} \int d^2r \rho_n^2(r) \sim \rho \xi^2 \quad . \quad (146)$$

The Baym-Chandler mass does not depend on the core radius  $R_{\text{sc}}$ , since the large area  $R_{\text{sc}}^2$  of integration in Eq. (146) is compensated by the small value of the normal component in the rarefied core,  $\rho_n \sim \rho(\xi/R_{\text{sc}})$ . That is why this mass is parametrically smaller than the Kopnin mass in Eq. (139), if the smooth core is large:  $R_{\text{sc}} \gg \xi$ .

In conclusion, both contributions to the mass of the vortex result from the mass of the normal component trapped by the vortex. The difference between Kopnin mass and Baym-Chandler backflow mass is only in the origin of the normal component trapped by the vortex. The relative importance of the two masses depends on the vortex core structure: (1) For the free continuous vortex with a large core size  $R_{\text{sc}} \gg \xi$ , the Kopnin mass dominates:  $M_{\text{Kopnin}} \sim \rho R_{\text{sc}} \xi \gg M_{\text{BC}} \sim \rho \xi^2$ . (2) For the circulation trapped around a wire of radius  $R_{\text{wc}} \gg \xi$ , the Baym-Chandler mass is proportional to the core area,  $M_{\text{BC}} \sim \rho R_{\text{wc}}^2$ , and is parametrically larger than the Kopnin mass. (3) For the free vortex core with a core radius  $R \sim \xi$  the situation is not clear since the continuous core approximation does not work any more. But extrapolation of the result in Eq. (146) to  $R \sim \xi$  suggests that the Baym-Chandler mass can be comparable with the Kopnin mass.

### 3.5.5. Topology of the energy spectrum: gap nodes and their ramifications

Zeroes in the fermionic spectrum, such as Fermi surfaces (surfaces of zeroes) and Fermi points (point zeroes) play an extremely important role in condensed matter and in analogue models of the low-energy physics of the quantum vacuum (Volovik 2003). In condensed matter, the gapless fermions interacting with the Bose fields of the order parameter lead to the anomalous behavior of superfluids and superconductors at low temperatures,  $T \ll T_c$ , such as spectral flow in vortex dynamics, non-analytic behavior of the current and gradient energy, nonlinear and nonlocal Meissner effect, etc. The counterpart of this behavior in high energy physics manifests itself in the axial anomaly, baryogenesis, zero charge effect, running coupling constants, photon mass, etc. It is the zeroes in the fermionic spectrum, through which the conversion of the vacuum degrees of freedom into that of matter takes place.

Similar zeroes, but in real space, exist in the cores of topological defects, especially in quantized vortices (or cosmic strings in high energy physics). Actually the

real-space zeroes and the momentum-space zeroes are described by the same topology extended to the  $8=4+4$  dimensional space. For example from the topological point of view, the Fermi-surface represents the vortex singularity of the Green's function in the  $\omega, \mathbf{p}$  space, where  $\omega$  is the Matsubara frequency. The Green's function  $G(\omega, p) = 1/(i\omega + v_F(p - p_F))$  displays a vortex in the  $\omega, p$  plane with the winding number  $\nu = 1$ . This makes the Fermi surface topologically stable and robust under perturbations of the Fermi system. Even though the pole in the Green's function can disappear under some perturbations, the Fermi surface will survive in the marginal and Luttinger superfluids. The latter thus belong to the same class of Fermi systems as the Landau Fermi-liquid.

In the same manner, superfluids and superconductors with a non-vanishing gap behave in the vicinity of the vortex core like superfluid  $^3\text{He-A}$  in bulk – point-like gap nodes appear to be the common feature. Owing to the common topological origin of the point nodes, the fermions near the gap nodes in gapless Fermi superfluids and superconductors and the low energy fermions localized in the cores of vortices in conventional gapped superconductors produce similar anomalous effects.

#### 4. FINAL REMARKS

We have examined here a few cases in which superfluid  $^3\text{He}$  has been used as an analogue system, to model new concepts in quantum field theory. The focus in Chap. 2 is on the question whether the observed vortex formation in a rapid 2nd order phase transition is described correctly by the Kibble-Zurek scaling theory in  $^3\text{He-B}$ . In  $^3\text{He-A}$  vortex formation (Ruutu et al. 1997b) and vortex dynamics (Eltsov et al. 2002) are very different. And so are the measuring techniques which are required to study these features. In fact, the rotating measurements on the KZ mechanism in Chap. 2 cannot be repeated in  $^3\text{He-A}$ , because vortex-free flow can be reached only up to  $\lesssim 1$  mm/s while, as seen in Fig. 13, the required threshold velocity  $v_{\text{cn}}$  is at least twice higher. No such fundamental limitations restrict calorimetric measurements on neutron absorption events in  $^3\text{He-A}$ , but present measuring techniques are not sufficiently developed to tackle this question. The consequences from spectral flow and chiral anomaly in the vortex dynamics of especially  $^3\text{He-A}$  have been described in Chap. 3. A number of other analogue models involving both  $^3\text{He-A}$  and B are described in the monograph by Volovik (2003).

What is the role of analogue studies in examining the validity of a new concept in physics? If such a test gives a positive result, then good grounds may exist to claim that the concept has fundamental value as a physical model. However, even if a particular model has been shown to work in superfluid  $^3\text{He}$  this does not imply uni-

versal applicability. Analogue studies are not a replacement for cosmological observations or a means to spare investments in high-energy accelerators! For instance, from a condensed matter experiment no direct conclusions can be drawn on the presence or absence of the KZ mechanism and its consequences in the Early Universe. Although superfluid  $^3\text{He}$  experiments in Chap. 2 support the validity of the KZ mechanism, at present this scenario is not a popular explanation for the anisotropy of the cosmic background radiation, which was precipitated by the inhomogeneity of the Early Universe when it had cooled to the point where it became transparent to radiation. Theories based on the presence of an epoch with exponentially accelerated inflationary expansion appear to provide better fits. Nevertheless, defects are formed in abundance in non-equilibrium phase transitions in condensed matter physics and one is left wondering why cosmological transitions should be any different. In this sense it remains an open mystery why defects would not have formed, or if indeed they were formed, what was their role in shaping the Early Universe.

Irrespective of its cosmological origin, in condensed matter physics the KZ mechanism has today become an important new concept in rapid non-equilibrium phase transitions. It is one of the few intrinsic processes of the bulk material which accounts for defect formation in a wide spectrum of different systems in the absence of boundaries, impurities, or other non-ideal constraints. The strongest experimental support to date for the KZ mechanism comes from the neutron absorption measurements in  $^3\text{He-B}$  where different types of defects are observed to form (usual mass-flow vortices, spin-mass vortices, AB interfaces). In these measurements it is also directly seen that later phase transition fronts, which sweep through the system, interact with the existing defects and that the final outcome depends on the relative velocity of the phase front with respect to the defects. The amount of work performed on the KZ mechanism in the form of simulations, measurements, and analysis by far exceeds other examples of analogue studies. It serves as a good example of what can be achieved with analogue studies in the unification of physical principles.

#### ACKNOWLEDGEMENTS

We would like to dedicate this work to Tom Kibble and Wojciech Zurek. We are indebted to Yu. Bunkov, A.P. Finne, A. Gill, H. Godfrin, H.E. Hall, J.R. Hook, T. Jacobson, N. Kopnin, A. Leggett, Yu. Makhlin, P. Mazur, B. Plaças, J. Ruohio, V. Ruutu, E. Thuneberg, T. Vachaspati, G. Williams, Wen Xu, and X. Zhang. Much of the cowork with these and many other colleagues was made possible by the ULTI visitor programs under the EU Human Capital and Mobility program (contract

no. CHGECT94-0069) and its continuation in the EU program Improving the Human Research Potential (no. HPRI-CT-1999-00050). This collaborative work has been inspired by the European Science Foundation programs Cosmology in the Laboratory (COSLAB) and Vortex Matter in Superconductors at Extreme Scales and Conditions (VORTEX).

## REFERENCES

- Aarts, R.G.K.M and A.T.A.M de Waele, 1994, Phys. Rev. B **50**, 10069.
- Adams, J.S., S.R. Bandler, S.M. Brouer, R.E. Lanou, H.J. Maris, T. More and G.M. Seidel, 1995, Phys. Lett. B **341**, 431.
- Adler, S., 1969, Phys. Rev. **177**, 2426.
- Aharonov, Y. and D. Bohm, 1959, Phys. Rev. **115**, 485.
- Albert, D.Z., 1982, Phys. Rev. B **25**, 4810.
- Amelino-Camelia, G., J.D. Bjorken and S.E. Larsson, 1997, Phys. Rev. D **56**, 6942.
- Andreev, A.F. and L.A. Melnikovskiy, 2003, Pis'ma Zh. Exp. Teor. Fiz. **78**, 1063; [JETP Lett. **78**, 574 (2003)].
- Antunes, N.D., L.M.A. Bettencourt and M. Hindmarsh, 1998, Phys. Rev. Lett. **80**, 908.
- Antunes, N.D., L.M.A. Bettencourt and W.H. Zurek, 1999, Phys. Rev. Lett. **82**, 2824.
- Antunes, N.D. and L.M.A. Bettencourt, 1998, Phys. Rev. Lett. **81**, 3083.
- Aranson, I.S., N.B. Kopnin and V.M. Vinokur, 1999, Phys. Rev. Lett. **83**, 2600.
- Aranson, I.S., N.B. Kopnin and V.M. Vinokur, 2001, Phys. Rev. B **63**, 184501.
- Awschalom, D.D. and K.W. Schwarz, 1984, Phys. Rev. Lett. **52**, 49.
- Barenghi, C.F., D.C. Samuels, G.H. Bauer and R.J. Donnelly, 1997, Phys. Fluids **9**, 2631.
- Barenghi, C.F. and D.C. Samuels, 2002, Phys. Rev. Lett. **89**, 155302.
- Barriola, M., 1995, Phys. Rev. D **51**, 300.
- Bäuerle, C., Yu.M. Bunkov, S.N. Fisher, H. Godfrin and G.R. Pickett, 1996, Nature **382**, 332.
- Bäuerle, C., Yu.M. Bunkov, S.N. Fisher, H. Godfrin and G.R. Pickett, 1998a, J. Low Temp. Phys. **110**, 13.
- Bäuerle, C., Yu.M. Bunkov, S.N. Fisher and H. Godfrin, 1998b, Phys. Rev. B **57**, 14381.
- Baym, G. and E. Chandler, 1983, J. Low Temp. Phys. **50**, 57.
- Beckurts, K.H. and K. Wirtz, 1964, Neutron Physics (Springer Verlag, Berlin, Germany).
- Bell, J.S. and R. Jackiw, 1969, Nuovo Cim. A **60**, 47.
- Bennett, C.L. et al., 2003, Astrophys. J. Suppl. **148**, 1.
- Bettencourt, L.M.A., N.D. Antunes and W.H. Zurek, 2000, Phys. Rev. D **62**, 065005.
- Bevan, T.D.C., A.J. Manninen, J.B. Cook, A.J. Armstrong, J.R. Hook and H.E. Hall, 1995, Phys. Rev. Lett. **74**, 750.
- Bevan, T.D.C., A.J. Manninen, J.B. Cook, H. Alles, J.R. Hook and H.E. Hall, 1997a, J. Low Temp. Phys. **109**, 423.
- Bevan, T.D.C., A.J. Manninen, J.B. Cook, J.R. Hook, H.E. Hall, T. Vachaspati and G.E. Volovik, 1997b, Nature **386**, 689.
- Bjorken, J.D., 1997, Acta Phys. Polon. B **28**, 2773.
- Blaauwgeers, R., V.B. Eltsov, M. Krusius, J.J. Ruohio, R. Schanen and G.E. Volovik, 2000, Nature **404**, 471.
- Blaauwgeers, R., V.B. Eltsov, G. Eska, A.P. Finne, R.P. Haley, M. Krusius, J.J. Ruohio, L. Skrbek and G.E. Volovik, 2002, Phys. Rev. Lett. **89**, 155301.
- Bowick, M.J., L. Chandar, E.A. Schiff and A.M. Srivastava, 1994, Science **263**, 943.
- Bradley, D.I., S.N. Fisher and W.M. Hayes, 1998, J. Low Temp. Phys. **113**, 687.
- Bradley, D.I., S.N. Fisher, M.R. Lowe A.M. Guénault, G.R. Pickett, A. Rahm and R.C.V. Whitehead, 2004, Phys. Rev. Lett.; in print.
- Bray, A., 1994, Adv. Phys. **43**, 357.
- Bunkov, Yu.M. and O.D. Timofeevskaya, 1998a, Phys. Rev. Lett. **80**, 4927.
- Bunkov, Yu.M. and O.D. Timofeevskaya, 1998b, J. Low Temp. Phys. **110**, 45.
- Camprostrini, M., M. Hasenbusch, A. Pelissetto, P. Rossi and E. Vicari, 2001, Phys. Rev. B **63**, 214503.
- Caroli, C., P.G. de Gennes and J. Matricon, 1964, Phys. Lett. **9**, 307.
- Chattopadhyay, B., M.C. Mahato and S.R. Shenoy, 1993, Phys. Rev. B **47**, 15159.
- Chuang, I., R. Durrer, N. Turok and B. Yurke, 1991, Science **251**, 1336.
- Cleary, R.M., 1968, Phys. Rev. **175**, 587.
- Collin, E., E. Moulin, F. Mayet, C. Winkelmann, Yu.M. Bunkov, H. Godfrin, M. Krusius and D. Santos, 2004, in print .
- Davis, R.L., 1992, Physica B **178**, 76.
- Davis, R.L. and E.P.S. Shellard, 1989, Phys. Rev. Lett. **63**, 2021.
- Demircan, E., P. Ao and Q. Niu, 1995, Phys. Rev. B **52**, 476.
- Deser, S., R. Jackiw and G. 't Hooft, 1984, Ann. Phys. **152**, 220.
- Dodd, M.E., P.C. Hendry, N.S. Lawson, P.V.E. McClintock and C.D.H. Williams, 1998, Phys. Rev. Lett. **81**, 3703.
- Donnelly, R.J., 1991, Quantized Vortices in Helium II (Cambridge University Press, Cambridge, UK).
- Duan, J.M., 1995, Phys. Rev. Lett. **75**, 974.
- Dziarmaga, J., 1998, Phys. Rev. Lett. **81**, 1551.
- Dziarmaga, J., 1999, Phys. Rev. Lett. **82**, 4749.
- Eltsov, V.B., T.W.B. Kibble, M. Krusius, V.M. Ruutu and G.E. Volovik, 2000, Phys. Rev. Lett. **85**, 4739.
- Eltsov, V.B., R. Blaauwgeers, N.B. Kopnin, M. Krusius, J.J. Ruohio, R. Schanen, E.V. Thuneberg and Wen Xu, 2002, Phys. Rev. Lett. **88**, 065301.
- Fetter, A.L., 1964, Phys. Rev. **136A**, 1488.
- Finne, A.P., T. Araki, R. Blaauwgeers, V.B. Eltsov, N.B. Kopnin, M. Krusius, L. Skrbek, M. Tsubota and G.E. Volovik, 2003, Nature **424**, 1022.
- Finne, A.P., S. Boldarev, V.B. Eltsov and M. Krusius, 2004a, J. Low Temp. Phys. **135**, 479.
- Finne, A.P., V.B. Eltsov, R. Blaauwgeers, Z. Janu, M. Krusius and L. Skrbek, 2004b, J. Low Temp. Phys. **134**, 375.
- Fisher, S.N., A.J. Hale, A.M. Guénault and G.R. Pickett, 2001, Phys. Rev. Lett. **86**, 244.

- Gal'tsov, D.V. and P.S. Letelier, 1993, *Phys. Rev. D* **47**, 4273.
- Garriga, J. and T. Vachaspati, 1995, *Nucl. Phys. B* **438**, 161.
- Geller, M.J. and J.P. Huchra, 1989, *Science* **246**, 897.
- Gill, A.J. and T.W. Kibble, 1996, *J. Phys. A: Math. Gen.* **29**, 4289.
- Giovannini, M. and E.M. Shaposhnikov, 1997, *Phys. Rev. Lett* **80**, 22.
- Goldner, L.S. and G. Ahlers, 1992, *Phys. Rev. B* **45**, 13129.
- Greywall, D.S., 1986, *Phys. Rev. B* **33**, 7520.
- Guillou, J.C. Le and J. Zinn-Justin, 1980, *Phys. Rev. B* **21**, 3976.
- Hakonen, P.J., M. Krusius, M.M. Salomaa and J.T. Simola, 1985, *Phys. Rev. Lett.* **54**, 245.
- Harari, D. and A.P. Polychronakos, 1988, *Phys. Rev. D* **38**, 3320.
- Hendry, P.C., N.S. Lawson, R.A.M. Lee, P.V.E. McClintock and C.D.H. Williams, 1994, *Nature* **368**, 315.
- Hendry, P.C., N.S. Lawson and P.V.E. McClintock, 2000, *J. Low Temp. Phys.* **119**, 249.
- Hindmarsh, M. and T. Kibble, 1995, *Rep. Progr. Phys.* **58**, 477.
- Ibaceta, D. and E. Calzetta, 1999, *Phys. Rev. E* **60**, 2999.
- Iengo, R. and G. Jug, 1995, *Phys. Rev. B* **52**, 7537.
- Iordanskii, S.V., 1964, *Ann. Phys.* **29**, 335.
- Iordanskii, S.V., 1965, *Zh. Exp. Teor. Fiz.* **49**, 225; [*Sov. Phys. JETP*, **22**, 160 (1966)].
- Jensen, B. and J. Kuvcera, 1993, *J. Math. Phys.* **34**, 4975.
- Joyce, M. and M. Shaposhnikov, 1997, *Phys. Rev. Lett.* **79**, 1193.
- Kafanov, S.G., A.Ya. Parshin and I.A. Todoshchenko, 2000, *Zh. Exper. Teor. Fiz.* **118**, 1143; [*JETP*, **91**, 991 (2000)].
- Kagan, Yu. and B.V. Svistunov, 1994, *Zh. Exper. Teor. Fiz.* **105**, 353; [*Sov. Phys. JETP* **78**, 187 (1994)].
- Kajantie, K., M. Karjalainen, M. Laine, J. Peisa and A. Rajantie, 1998, *Phys. Lett. B* **428**, 334.
- Kao, H.-C. and K. Lee, 1995, *Phys. Rev. D* **52**, 6050.
- Karra, G. and R.J. Rivers, 1998, *Phys. Rev. Lett.* **81**, 3707.
- Keto, J.W., F.J. Soley, M. Stockton and W.A. Fitzsimmons, 1974, *Phys. Rev. A* **10**, 872.
- Kibble, T.W., 1976, *J. Phys. A* **9**, 1387.
- Kibble, T.W.B. and A. Rajantie, 2003, *Phys. Rev. B* **68**, 174512.
- Kibble, T.W. and G.E. Volovik, 1997, *Pis'ma Zh. Exp. Teor. Fiz.* **65**, 96; [*JETP Lett.* **65**, 102 (1997)].
- Kirtley, J.R., C.C. Tsui and F. Tafuri, 2003, *Phys. Rev. Lett.* **90**, 257001.
- Kleinert, H., 1980, *J. Low Temp. Phys.* **39**, 451.
- Kleinert, H., 1989, *Gauge Fields in Condensed Matter* (World Scientific, Singapore).
- Kleinert, H. and B. Van den Bossche, 2001, *Phys. Rev. E* **63**, 056113.
- Kondo, Y., J.S. Korhonen, M. Krusius, V.V. Dmitriev, E.V. Thuneberg and G.E. Volovik, 1992, *Phys. Rev. Lett.* **68**, 3331.
- Koplik, J. and H. Levine, 1993, *Phys. Rev. Lett.* **71**, 1375.
- Kopnin, N.B., 1978, *Pis'ma Zh. Exp. Teor. Fiz.* **27**, 417; [*JETP Lett.* **27**, 390 (1978)].
- Kopnin, N.B., 1993, *Phys. Rev. B* **47**, 14354.
- Kopnin, N.B., 1995, *Physica B* **210**, 267.
- Kopnin, N.B., 2002, *Rep. Progr. Phys.* **65**, 1633.
- Kopnin, N.B., G.E. Volovik and Ü. Parts, 1995, *Europhys. Lett.* **32**, 651.
- Kopnin, N.B. and M.M. Salomaa, 1991, *Phys. Rev. B* **44**, 9667.
- Kopnin, N.B. and E.V. Thuneberg, 1999, *Phys. Rev. Lett.* **83**, 116.
- Kopnin, N.B. and V.M. Vinokur, 1998, *Phys. Rev. Lett.* **81**, 3952.
- Kopnin, N.B. and G.E. Volovik, 1998, *Phys. Rev. B* **57**, 8526.
- Kopu, J., R. Schanen, R. Blaauwgeers, V.B. Eltsov, M. Krusius, J.J. Ruohio and E.V. Thuneberg, 2000.
- Kopu, J. and M. Krusius, 2001, *Phys. Rev. B* **64**, 094504.
- Korhonen, J.S., A.D. Gongadze, Z. Janu, Y. Kondo, M. Krusius, Yu.M. Mukharsky and E.V. Thuneberg, 1990, *Phys. Rev. Lett.* **65**, 1211.
- Korhonen, J.S., Y. Kondo, M. Krusius, E.V. Thuneberg and G.E. Volovik, 1993, *Phys. Rev. B* **47**, 8868.
- Krusius, M., E.V. Thuneberg and Ü. Parts, 1994, *Physica B* **197**, 376.
- Krusius, M., T. Vachaspati and G.E. Volovik, 1998, preprint cond-mat/9802005.
- Laguna, P. and W.H. Zurek, 1997, *Phys. Rev. Lett.* **78**, 2519.
- Lee, K.-M., 1994, *Phys. Rev. D* **49**, 4265.
- Leggett, A.J., 1984, *Phys. Rev. Lett.* **53**, 1096.
- Leggett, A.J., 1992, *J. Low Temp. Phys.* **87**, 571.
- Leggett, A.J., 2002, *J. Low Temp. Phys.* **126**, 775.
- Linde, A., 1990, *Particle physics and inflationary cosmology* (Harwood Acad. Publ., Switzerland).
- Lipa, J.A., D.R. Swanson, J.A. Nissen, T.C.P. Chui and U.E. Israelsson, 1996, *Phys. Rev. Lett.* **76**, 944.
- Lipa, J.A., J.A. Nissen, D.A. Stricker, D.R. Swanson and T.C.P. Chui, 2003, *Phys. Rev. B* **68**, 174518.
- Maniv, A., E. Polturak and G. Koren, 2003, *Phys. Rev. Lett.* **91**, 197001.
- Mazur, P.O., 1986, *Phys. Rev. Lett.* **57**, 929.
- Mazur, P.O., 1987, *Phys. Rev. Lett.* **59**, 2380.
- Mazur, P.O., 1996, preprint hep-th/9611206.
- Meyer, J.S. and T. Sloan, 1997, *J. Low Temp. Phys.* **108**, 345.
- Mino, Y., M. Sasaki and T. Tanaka, 1997, preprint gr-qc/9705073.
- Nelson, D.R. and J.M. Kosterlitz, 1977, *Phys. Rev. Lett.* **39**, 1201.
- Nemirovskii, S.K. and W.M. Fiszdon, 1994, *Physica B* **197**, 290.
- Onsager, L., 1949, *Nuovo Cimento* **6**, Suppl. 2, 249.
- Packard, R.E., 1998, *Rev. Mod. Phys.* **70**, 641; and references therein.
- Parts, Ü., Y. Kondo, J.S. Korhonen, M. Krusius and E.V. Thuneberg, 1993, *Phys. Rev. Lett.* **71**, 2951.
- Parts, Ü., V.M. Ruutu, J.H. Koivuniemi, Yu.M. Bunkov, V.V. Dmitriev, M. Fogelström, M. Huebner, Y. Kondo, N.B. Kopnin, J.S. Korhonen, M. Krusius, O.V. Lounasmaa, P.I. Soininen and G.E. Volovik, 1995, *Europhys. Lett.* **31**, 449.
- Peacock, J.A. et al., 2001, *Nature* **410**, 169.
- Rajantie, A., 1998, *Physica B* **255**, 108.
- Rajantie, A., 2001, *J. Low Temp. Phys.* **124**, 5.
- Rajantie, A., K. Kajantie, M. Karjalainen, M. Laine and J. Peisa, 1998, preprint hep-lat/9807042.
- Rivers, R.J., 2000, *Phys. Rev. Lett.* **84**, 1248.
- Roberge, A., 1989, *Finite Density Effects in Gauge Theories*,



- Ph. D. thesis, University of British Columbia.
- Ruutu, V.M., V.B. Eltsov, A.J. Gill, T.W. Kibble, M. Krusius, Yu.G. Makhlin, B. Plaças, G.E. Volovik and Wen Xu, 1996a, *Nature* **382**, 334.
- Ruutu, V.M., Ü. Parts, B. Plaças, Wen Xu, G.E. Volovik and M. Krusius, 1996b, *Czechoslovak J. Phys.* **46**, Suppl. S1, 15.
- Ruutu, V.M.H., J. Kopu, M. Krusius, Ü. Parts, B. Plaças, E.V. Thuneberg and Wen Xu, 1996c, *Czechoslovak J. Phys.* **46**, Suppl. S1, p. 7.
- Ruutu, V.M., Ü. Parts, J.H. Koivuniemi, N.B. Kopnin and M. Krusius, 1997a, *J. Low Temp. Phys.* **107**, 93.
- Ruutu, V.M.H., J. Kopu, M. Krusius, Ü. Parts, B. Plaças, E.V. Thuneberg and Wen Xu, 1997b, *Phys. Rev. Lett.* **79**, 5058.
- Ruutu, V.M., V.B. Eltsov, M. Krusius, Yu.G. Makhlin, B. Plaças and G.E. Volovik, 1998a, *Phys. Rev. Lett.* **80**, 1465.
- Ruutu, V.M., J.J. Ruohio, M. Krusius, B. Plaças and E.B. Sonin, 1998b, *Physica B* **255**, 27.
- Salomaa, M.M. and G.E. Volovik, 1987, *Rev. Mod. Phys.* **59**, 533.
- Samuels, D.C., 1992, *Phys. Rev. B* **46**, 11714.
- Schiffer, P., M.T. O'Keefe, M.D. Hildreth, H. Fukuyama and D.D. Osheroff, 1992, *Phys. Rev. Lett.* **69**, 120.
- Schiffer, P.E., D.D. Osheroff and A.J. Leggett, 1995, in: *Prog. Low Temp. Phys.*, Vol. XIV, ed W. Halperin (Elsevier Science B. V., Amsterdam) p. 159; and references therein.
- Schiffer, P. and D.D. Osheroff, 1995, *Rev. Mod. Phys.* **67**, 491.
- Schwarz, K.W., 1978, *Phys. Rev. B* **18**, 245.
- Schwarz, K.W., 1985, *Phys. Rev. B* **31**, 5782.
- Schwarz, K.W., 1988, *Phys. Rev. B* **38**, 2398.
- Shelankov, A., 1998a, preprint cond-mat/9802158.
- Shelankov, A., 1998b, *Europhys. Lett.* **43**, 623.
- Sonin, E.B., 1975, *Zh. Exp. Teor. Fiz.* **69**, 921; [*Sov. Phys. JETP* **42**, 469 (1976)].
- Sonin, E.B., 1997, *Phys. Rev. B* **55**, 485.
- Sonin, E.B., V.H. Geshkenbein, A. van Otterlo and G. Blatter, 1998, *Phys. Rev. B* **57**, 575.
- Spergel, D.N. et al., 2003, *Astrophys. J. Suppl.* **148**, 175.
- Starkman, G.D., 1996, *Phys. Rev. D* **53**, 6711.
- Staruszkiewicz, A., 1963, *Acta Phys. Polon.* **24**, 734.
- Stockton, M., J.W. Keto and W.A. Fitzsimmons, 1971, *Phys. Rev. A* **5**, 372.
- Stone, M., 1996, *Phys. Rev. B* **54**, 13222.
- Strösser, M. and V. Dohm, 2003, *Phys. Rev. E* **67**, 056115.
- Tang, Y.H., I. Hahn, H.M. Bozler and C.M. Gould, 1991, *Phys. Rev. Lett.* **67**, 1775.
- Thorne, K.S. and J.B. Hartle, 1985, *Phys. Rev. D* **31**, 1815.
- Tough, J.T., 1982, in: *Prog. Low Temp. Phys.*, Vol. XIII, ed W. Halperin (Elsevier Science B. V., Amsterdam) p. 133; and references therein.
- Toyoki, H., 1994, *J. Phys. Soc. Japan* **63**, 446.
- Tsubota, M. and H. Yoneda, 1995, *J. Low Temp. Phys.* **101**, 815.
- Unruh, W.G., 1976, *Phys. Rev. D* **14**, 870.
- Vachaspati, T., 1994, in: *Proc. NATO Workshop "Electroweak Physics and the Early Universe"*, Sintra, Portugal, Vol. 338 of Series B: Physics (Plenum Press, New York).
- Vachaspati, T. and G.B. Field, 1994, *Phys. Rev. Lett.* **73**, 373.
- Vachaspati, T. and G.B. Field, 1995, *Phys. Rev. Lett.* **74**, 1258.
- Vachaspati, T. and A. Vilenkin, 1984, *Phys. Rev. D* **30**, 2036.
- van Otterlo, A., M.V. Feigel'man, V.B. Geshkenbein and G. Blatter, 1995, *Phys. Rev. Lett.* **75**, 3736.
- Varoquaux, E., O. Avenel, P. Hakonen and Yu. Mukharsky, 1998, *Physica B* **255**, 55; and references therein.
- Vollhardt, D., K. Maki and N. Schopohl, 1980, *J. Low Temp. Phys.* **39**, 79.
- Vollhardt, D. and P. Wölfle, 1990, *The Superfluid Phases of Helium 3* (Taylor & Francis).
- Volovik, G.E., 1990, in: *Helium Three*, eds W. Halperin and L. Pitaevskii (Elsevier Science B. V., Amsterdam) p. 27.
- Volovik, G.E., 1992, *Exotic Properties of Superfluid <sup>3</sup>He* (World Scientific, Singapore).
- Volovik, G.E., 1996, *Czechoslovak J. Phys.* **46**, Suppl. S6, 3048.
- Volovik, G.E., 1997, *Pis'ma Zh. Exp. Teor. Fiz.* **65**, 201; [*JETP Lett.* **65**, 217 (1997)].
- Volovik, G.E., 1998, *Physica B* **255**, 86.
- Volovik, G.E., 2003, *The Universe in a Helium Droplet* (Oxford Science Publications, Oxford).
- Volovik, G.E. and V.P. Mineev, 1982, *Zh. Exp. Teor. Fiz.* **83**, 1025; [*Sov. Phys. JETP* **56**, 579 (1982)].
- Volovik, G.E. and T. Vachaspati, 1996, *Int. J. Mod. Phys. B* **10**, 471.
- Wexler, C., 1997, *Phys. Rev. Lett.* **79**, 1321.
- Wexler, C. and D.J. Thouless, 1996, preprint cond-mat/9612059.
- Wheatley, J.C., 1975, *Rev. Mod. Phys.* **47**, 415.
- Wilczek, F., 1998, *Physics Today* **51**, N1 (January), 11.
- Williams, G.A., 1993a, *Phys. Rev. Lett.* **71**, 392.
- Williams, G.A., 1993b, *J. Low Temp. Phys.* **93**, 1079.
- Williams, G.A., 1999, *Phys. Rev. Lett.* **82**, 1201.
- Witten, E., 1985, *Nucl. Phys. B* **249**, 557.
- Xu, Wen, B. Plaças, V.M. Ruutu and M. Krusius, 1996, *Czechoslovak J. Phys.* **46**, Suppl. S1, 11.
- Yates, A. and W.H. Zurek, 1998, *Phys. Rev. Lett.* **80**, 5477.
- Zapotocky, M., P.M. Goldbart and N. Goldenfeld, 1995, *Phys. Rev. E* **51**, 1216.
- Zurek, W.H., 1985, *Nature* **317**, 505.
- Zurek, W.H., 1996, *Phys. Rep.* **276**, 177.